Predictive Control Strategies of Modular Multilevel Matrix Converter

by **Rodrigo H. Cuzmar**

Thesis submitted in fulfilment of the requirements for the degree of
Doctor of Philosophy
under the supervision of
Supervisor: Ricardo P. Aguilera
Co-supervisor: Dylan Lu

School of Electrical and Data Engineering
Faculty of Engineering and IT
University of Technology Sydney
November 27, 2024

Certificate of Authorship / Originality

I, Rodrigo H. Cuzmar, declare that this thesis is submitted in fulfilment of the requirements for the award of Doctor of Philosophy, in the School of Electrical and Data Engineering at the University of Technology Sydney.

This thesis is wholly my own work unless otherwise referenced or acknowledged. In addition, I certify that all information sources and literature used are indicated in the thesis.

I certify that the work in this thesis has not previously been submitted for a degree nor has it been submitted as part of the requirements for a degree at any other academic institution except as fully acknowledged within the text. This thesis is the result of a Collaborative Doctoral Research Degree program with Pontifical Catholic University of Chile.

This research is supported by the Australian Government Research Training Program.

Signature: Production Note: Signature removed prior to publication.

Date: November 27, 2024

ABSTRACT

Currently, the world is transitioning to a new energy paradigm, shifting from systems with low penetration of renewable energy, unidirectional power flows, and minimal power converter use, to systems featuring high renewable energy integration, bidirectional power flows, and extensive use of power converters. AC-to-AC converters will play a key role in future applications, such as power system interconnection, low-frequency AC (LFAC) transmission, wind energy conversion systems (WECS), and medium/high voltage motor drives for industries like mining, marine propulsion, and more. Countries like Chile and Australia predict WECSs will become a primary energy source by 2050. Additionally, both countries present an active mining activity which includes several motor drives applications. However, the future AC-to-AC converters for the aforementioned applications, such as modular multilevel matrix converter (M3C), present technical challenges for their implementation, for instance, highly coupled internal states, complex control and balance of several floating capacitors, a large number of control signals, and capacitor voltage oscillations at critical frequencies, which complicates its implementation in high voltage applications that require a large number of sub-modules.

This research aims to develop a predictive control strategy for the M3C. The proposed solution includes an inner controller responsible for current control and local-cluster balancing, and an outer controller to manage inter-cluster balancing and mitigate low-frequency oscillations in sub-module capacitor voltages. On one hand, two strategies are proposed for the inner controller: sequential phase-shifted model-predictive-control (sPS-MPC) and finite-control-set MPC (FCS-MPC). On the other hand, two reference generator are proposed as outer controller, one generates circulating currents as a function of the cluster energies in a transformed space, and the other considers circulating currents and common-model voltage to balance the M3C energy.

Experimental results demonstrate the effectiveness of these strategies in controlling the M3C, achieving accurate current and energy tracking. In steady-state, the average tracking error for currents and voltages is 1.96% and 1.82%, respectively, with a reduction in capacitor voltage ripple of 31% for low frequency and 36% for equal frequency. During transients, power and frequency step changes are met instantaneously, while step changes in local- and inter-cluster balancing control are achieved in 80 and 200 ms, respectively. The computational burden increases linearly with the number of sub-modules, except in the FCS-MPC strategy.

Keywords: Circulating currents, common-mode voltage, direct ac-to-ac conversion, energy balance, model predictive control, modular multilevel matrix converter (M3C), phase-shifted pulse width modulation (PS-PWM), triple-star bridge cells (TSBC).

Labor omnia vincit improbus
et duris urgens in rebus egestas

Virgil

ACKNOWLEDGEMENTS

I wish to express my sincere thanks to all the people who supported me during this long process.

Firstly, I would like to thank my family who has always been and will be there to support me unconditionally. This fact has been proved several times during my life, so I consider them a fundamental pillar in all my projects. Therefore, thank to my parents, Cecilia and Sergio, for their unconditional support in my personal development. Additionally, thanks to my sister and brother, Maca and Javier, for their advice and support in the most complicated situations.

Secondly, I want to thank to my supervisors who advice me during all this research. Their comments, suggestions and support were fundamental to accomplish all the objectives during my Ph.D. project. Hence, thank to Javier, Ricardo and Andrés for all the time and guidance provided that have built my second fundamental pillar which is related to my professional development.

Thirdly, I thank to my laboratory partners who have been there for the challenges that implementation presents. Thank to Pablo, Gabriel, Andrés and José for their suggestions and help during unexpected behavior in the prototype.

Fourthly but not least, I would like to thank all my friends for the moments of distraction and leisure which are indispensable to properly address a project like this. So, thank to my friends from school, Nicolás, Óscar, Matías, Fernando and Mario; thank to my friends from Australia, Ignacio, Pablo again, Majid, Hamid, Pato; and thank to my friends from handball, Samuel, Gonzalo, Sebastián and Miguel; which are the third and last fundamental pillar that allows me to keep good results in my projects.

Finally, I want to thank to all the funds that made this possible. Thank to ANID for Beca Doctorado Nacional and UTS for UTS President's Scholarship. Additionally, this work was supported in part by: ANID through Fondecyt project 1220928 and 1231030; FONDAP/1523A0006 SERC Chile; and FB0008 Advanced Center for Electrical and Electronics Engineering; and by the Australian Government through the Australian Research Council (Discovery Project No. DP240102646).

Rodrigo H. Cuzmar
November 27, 2024
Sydney, Australia

Contents

List of Figures

List of Tables

Chapter 1

INTRODUCTION

The productive, social and scientific development are directly related with the energy, which is the capability to do work. Along human history the use of energy has been a keystone for its development, from human labor at the beginning into electrical machines today. Since 18th century, with the invention of steam engine and the industrial revolution, the energy has allowed to simplify processes and achieve new efficiencies in a wide range of applications, not only in the industry but in the everyday life as well. Nowadays, the energy is used in almost every activity, specifically electric energy [1].

The world has met multiple times into the Conference of Parties (CoP) to face climate change. During the last years, one of the common agreements has been to reduce the emission of greenhouse gases [2], [3], where the energy industry produces 34% of the total emission in the world [4]. Greenhouse gases are mainly produced by fuel combustion and emissions derived from fuel. In the energy sector, they correspond to fossil fuel generators, so the world is changing into renewable energies. With this thought in mind, the energy matrix of the countries is in a transformation process, from an electric system with unidirectional power flow, low participation of power converters and low penetration of renewable energies, to an electric system with bidirectional power flow, high penetration of renewable energies and high participation of power converters. Specific examples are Australia and Chile, which have been carrying out an energy transition process and decarbonization of the energy matrix of the countries [5], [6], replacing oil, black coal and natural gas fuels with renewable energies (specially, wind and solar power) for a net zero emission by 2050 as presented in Fig. 1.1 and 1.2.

1.1 AC-AC applications

Most of the applications required by future systems will rely on power converters to facilitate the conversion of electrical energy. These converters can be categorized into different types, including dc-dc converters, inverters (dc-ac converters), ac-ac converters, and rectifiers (ac-dc converters).

Several noteworthy ac-ac applications are anticipated for future electric systems, such as power systems interconnection, low-frequency ac (LFAC) transmission systems, wind energy conversion systems (WECS), and motor drives for transportation or industrial activities, among others. Power systems interconnection enables the exchange of energy between electrical systems, even when they operate at varying voltage levels or frequencies. This enhances network

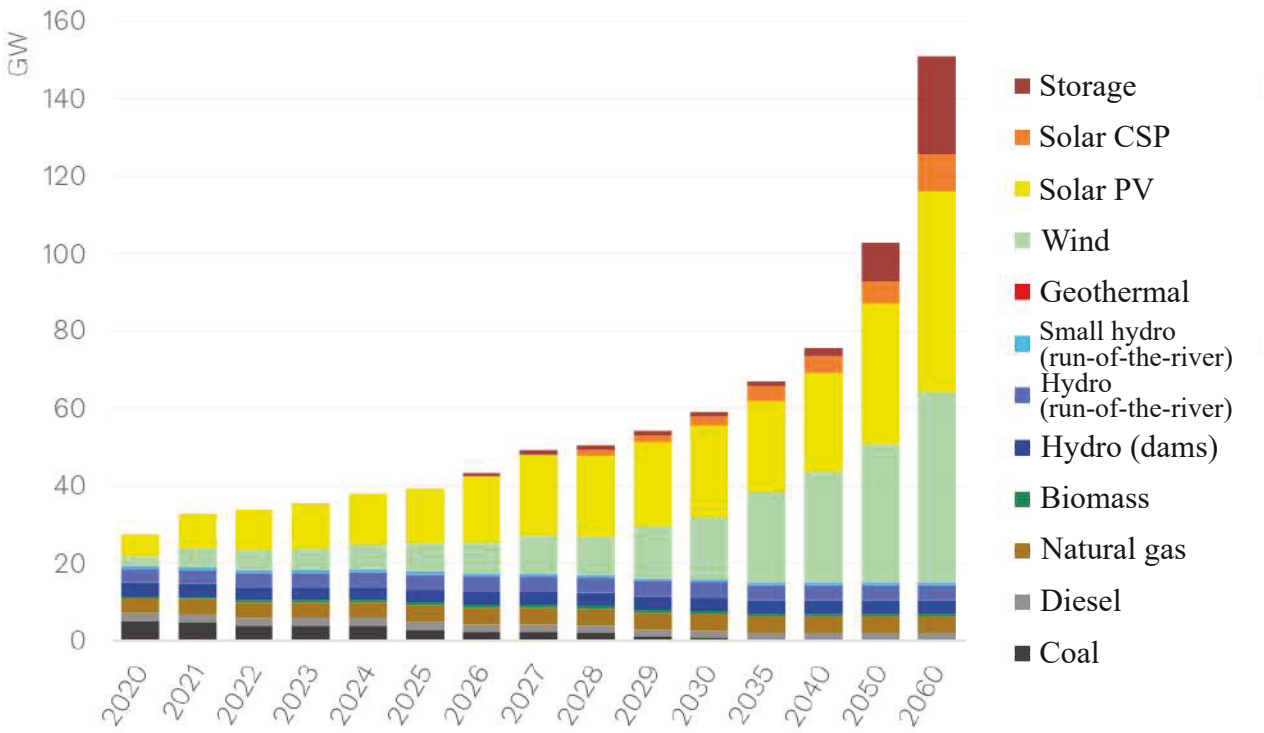

Figure 1.1: Forecasted Capacity Chile 2022-2060 [7]

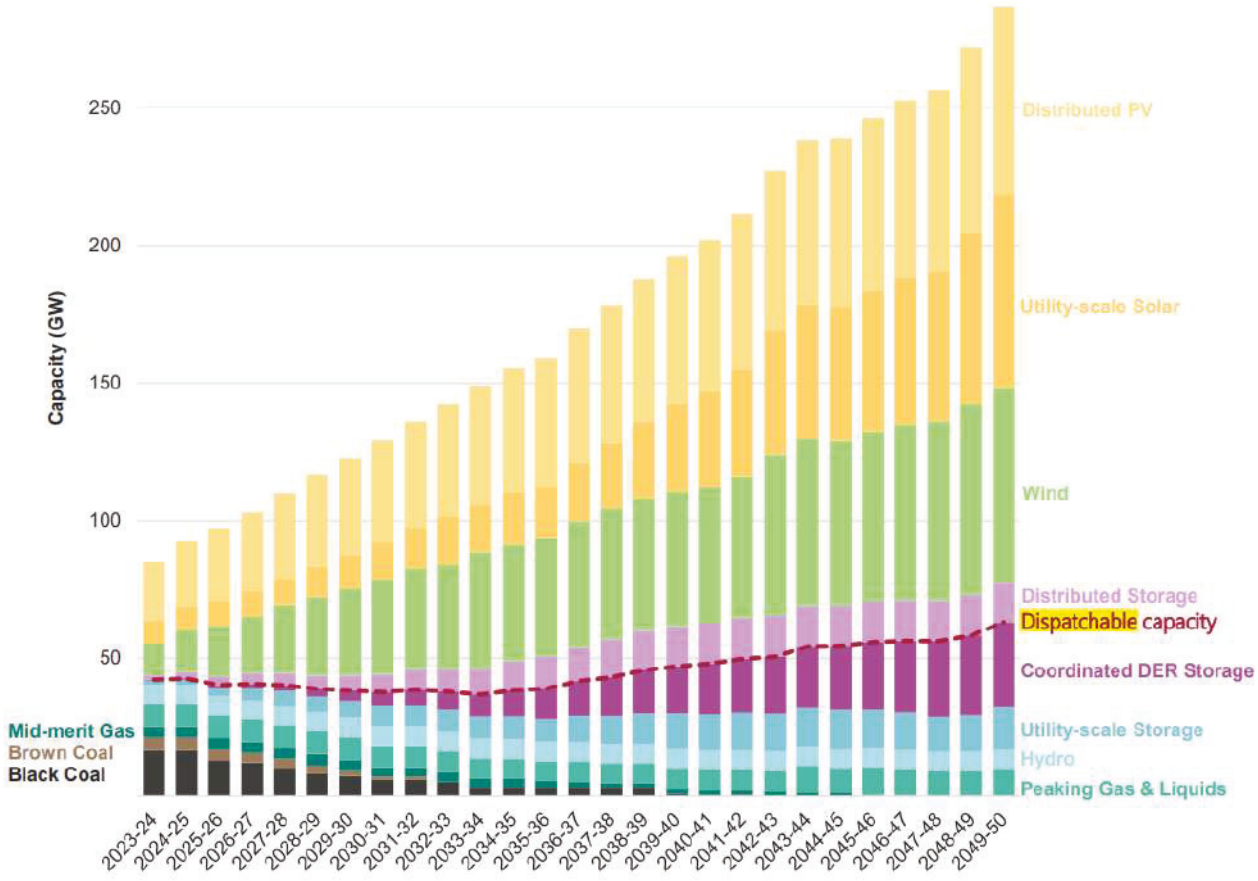

Figure 1.2: Forecasted Capacity Australia 2023-2050 [8]

reliability by compensating for weaknesses and capitalizing on strengths.

The transmission systems are undergoing significant advances to address the parasitic effects associated with the length of transmission lines. One popular approach is to reduce the operating frequency of the transmission line since the parasitic effects are directly related to the frequency. High Voltage DC (HVDC) and Low Frequency AC (LFAC) transmission systems offer solutions to extend the transmission line distance by lowering the operating frequency. However, LFAC systems can utilize the existing transmission line infrastructure (three-phase system) unlike HVDC systems (DC system) which require separate infrastructure for optimal operation at nominal power.

In Chile and Australia (refer to Fig. 1.1 and 1.2), solar and wind power are anticipated to become the primary sources of energy for industries and general population. Wind power harnesses the kinetic energy of moving air masses through the blades, converting it into three-phase electric energy that needs to be injected into a three-phase network. Moreover, studies have been done to check the feasibility to connect the Chilean (50 Hz) and Peruvian (60 Hz) power systems, which consider to use power converters to achieve this interconnection [9].

Furthermore, one longstanding and widely used application of ac-ac converters is in motor drives. Industries that rely on high voltage or high power motors often connect them directly to the three-phase grid. Examples include marine propulsion, mills, pumps, conveyors, and various other applications.

The future systems and applications already mentioned require the proper hardware to make them possible. The power converters are key for all these high voltage and high power applications, and within them, the modular multilevel cascaded converters are considered one of the most attractive technologies for the next generation of control and conversion of electrical power, mainly due to their modularity, lower voltage requirements for semiconductors, voltage and power scalability, reduced dv/dt, and fault tolerance.

1.2 Challenges

The future grids present several technical challenges for their performance along the world, which affect the efficiency, reliability, flexibility and performance of power converters in these applications and with it, the robustness of the power system.

Variable Frequency Applications

AC-to-AC applications usually require operation at different frequencies, so the power converters must dynamically change their frequency operating points. In terms of renewable energies, WECSs generate energy as a function of the mass of air passing through the blades, mass of air depends on the weather and varies every day and every hour, making this power source a variable frequency application. Therefore, WECSs are an intermittent energy source that requires a power converter along with a control strategy capable to handle variable frequencies. As a common industry application, motor drive systems govern high-power and low-frequency motors that must be directly connected to the three-phase system such as medium/high voltage motor drives for marine propulsion, mills, pumps, conveyors and crushing process in mining activity. These applications require to operate at very low and variable frequencies.

Bidirectional Power Flow

Future grids will present a high participation of power converters, bidirectional power flows and high participation of renewable energies. Generation at distribution level and the use of battery energy storage systems (BESS) are changing how the energy has been transmitted, transforming what was considered a load only into something that can act as either a load or a generator, depending on the time and application. Microgrids are good examples of bidirectional power flow. During day, photovoltaic systems and WECSs can generate more power than is needed in the microgrid, so the excess is injected to the main grid. However, during night, photovoltaic systems cannot generate power, so the missing energy that WECSs are not able to provide must be supplied by the main grid. Therefore, the future grid requires power converters with bidirectional capabilities. Additionally, the reduction of conventional energy sources introduces a new challenge to the system stability. The reduction of conventional energies has decreased the inertia of the power system, reducing its reliability under fault conditions. Hence, the power converters must have capabilities to act fast in order to provide ancillary services in emergency situations.

Parasitic Effects in Transmission Lines

Current High Voltage AC (HVAC) transmission lines are typically limited due to the parasitic effects that occur as a function of the frequency which is 50 or 60 Hz. These effects generate a parasitic capacitance that requires reactive power. Therefore, by increasing the length of the line, the parasitic capacitance increases, requiring more reactive power and limiting the maximum active power the line can transmit. Additionally, the skin effect increases the resistance of the line as a function of the frequency as well. So, new methods power transmission are required for futures grid.

For long transmission lines, the preferred method is to use an HVDC transmission system. As the name mentions, the frequency is zero, therefore, the parasitic effects are eliminated. Nevertheless, due to the absence of the zero-crossing points in HVDC systems, the breakers for these systems are more challenging in comparison with an AC system. This fact make DC breakers more expensive and exclusive than AC breakers because of the specific application in high-power, and the technology that they need to interrupt a high DC current.

To overcome HVAC and HVDC systems, the LFAC transmission systems have been proposed. These systems propose reducing the line frequency by including AC-to-AC power converters at the end of the line. Therefore, the parasitic effects are reduced and the zero-crossing points to disconnect the line is presented for emergency situations.

Complex Control for Future Power Converters

The required power converters for the future power system need to accomplish all the previous mentioned features. For instance, AC-to-AC transformation, bidirectional power flow, high voltage, high power and low-frequency operation. However, these power converters present several challenges such as complex control due to non-linear dynamic and several coupled internal states. Additionally, these converters have multiple control objectives, more control objectives than degrees of freedom, floating capacitors that must be regulated and a large number of control signals, requiring multivariable control schemes which are normally accomplished by using various control loops, some coupled to each other and others uncoupled, making them a challenge to design and implement.

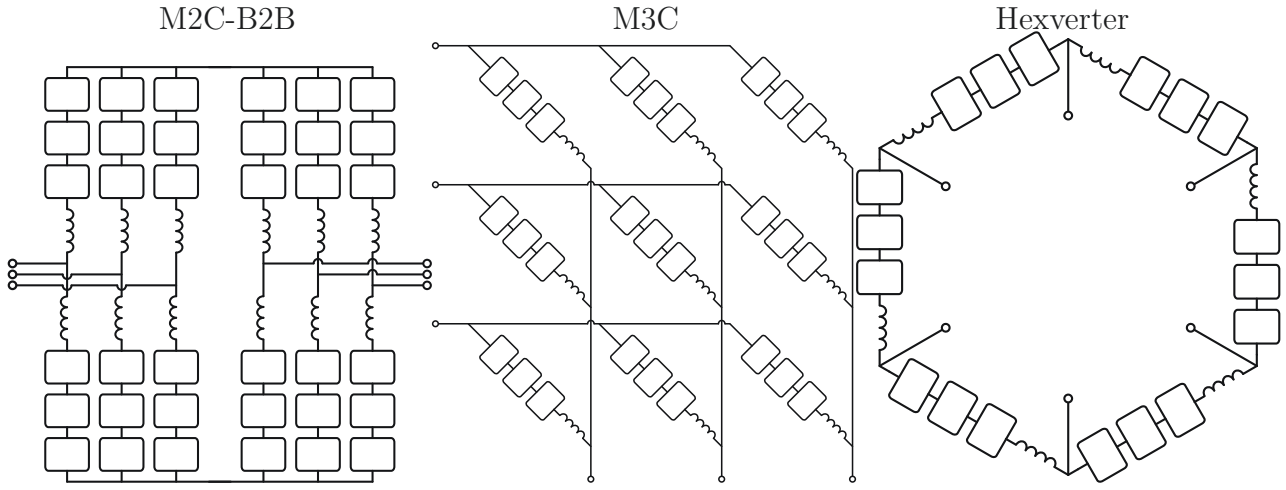

Figure 1.3: Modular multilevel cascaded converters for ac-ac conversion

1.3 State of the Art

This section presents the main publications in the literature regarding modular multilevel converters for ac-ac applications, controllers used for the different control objectives required by the modular multilevel matrix converter, and optimal control strategies for modular multilevel converters.

1.3.1 Modular Multilevel Cascaded Converters

Modular multilevel cascaded converters (MMCCs) are considered one of the most attractive technologies for the next generation of control and conversion of electrical power, mainly due to their modularity, lower voltage requirements for semiconductors, voltage and power scalability, reduced dv/dt, and fault tolerance. In terms of ac-ac conversion, the main examples of MMCCs are the Modular Multilevel Matrix Converter (M3C), the Modular Multilevel Back-to-Back Converter (M2C-B2B), and the Hexverter (see Fig. 1.3) for applications such as power system interconnections (50-60 Hz), low frequency ac transmission systems (LFAC), wind energy conversion systems (WECS) and medium/high voltage motor drives for marine propulsion, mills, pumps, conveyors, among other applications [10].

Among them, the M3Cs, also known as triple-star bridge cells (TSBC), are promising for direct ac-ac power conversion because they do not require a high voltage dc-link [11], [12], and need less sub-modules in comparison with the B2B-M2C [13]. Additionally, the M3C reactive power between input and output three-phase systems is decoupled, unlike the Hexverter [14]. For these reasons, M3C is considered as an alternative to meet all the requirements of the aforementioned applications. Hence, the M3C excels over the B2B-M2C in LFAC transmission systems, WECS and low-speed motor drives, showing a better performance at low-frequency operation [15]. A brief comparison of these three converters have been included in the Table 1.1.

Therefore, because of its advantages in comparison with M3C and Hexverter as an ac-ac power converter, the modular multilevel matrix converter or M3C is the converter chosen to be used in this research.

However, the M3C presents several challenges such as highly coupled internal states, complex control and balance of several floating capacitors, a big number of control signals, and capacitor

Table 1.1: Comparison summary of modular multilevel cascaded converters for ac-ac applications.

	M2C-B2B	M3C	Hexverter
Sub-module	Half bridge	Full bridge	Full bridge
Clusters	12	9	6
Reactive power Input-Output	Decoupled	Decoupled	Coupled
Direct Current Stage	Required	No required	No required

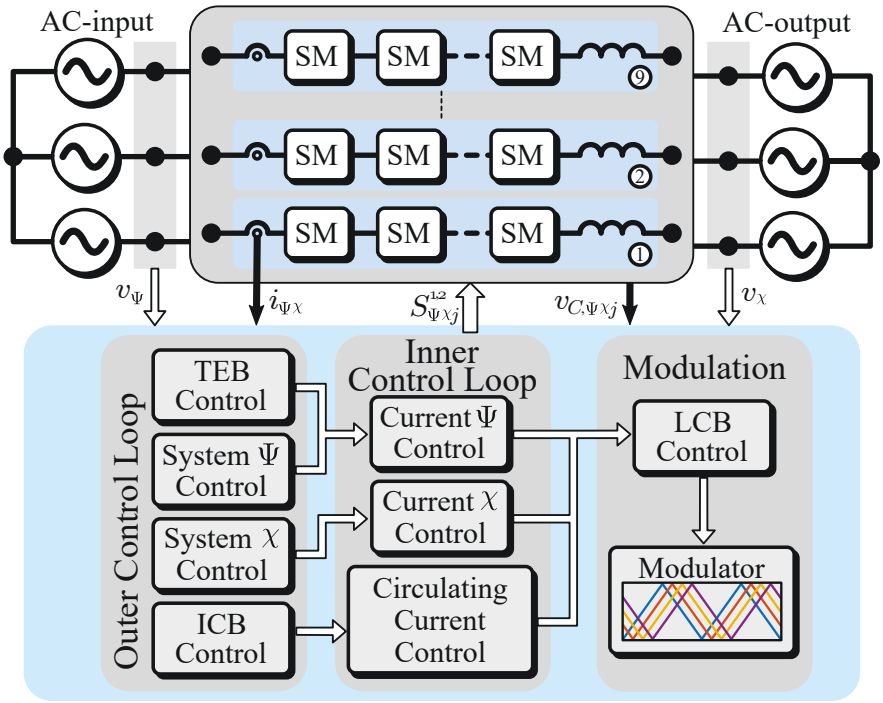

Figure 1.4: General control scheme for the modular multilevel matrix converter

voltage oscillations at low and similar frequencies, which complicates its implementation in high voltage applications that require a large number of sub-modules. [16], [17].

1.3.2 M3C Control Objectives

The M3C has multiple coupled control objectives, which make it a complex system from a control point of view. The general control scheme of an M3C is presented in Fig. 1.4, which is divided into three stages: outer controllers, inner controllers, and modulation. The outer controllers generate current references for the inner controllers. Then, the inner controllers generate duty cycles, which are adjusted to balance the energy among sub-modules (SMs) before being synthesized by the modulator and applied to the M3C.

In order to govern the M3C and tackle the previously mentioned problems, several control

strategies have been proposed. A standard control strategy for M3Cs consists of using a multiple loop of proportional-integral (PI) controllers working in multiple transformed references to achieve decoupling [11], [12], [16], [18]. However, the use of multiple single-input-single-output (SISO) controllers for a highly coupled system, which has more variables than degrees of freedom, reduces the robustness of the control in comparison with a multiple-inputs-multiple-outputs (MIMO) controller [19]. Additionally, linear controllers are tuned only for one operation point, present slower dynamic response and overshoot due to the integration action of PI controllers.

The finite-control-set model-predictive-control (FCS-MPC) has been proposed in the literature to solve the aforementioned SISO control limitations [20], [21]. However, the FCS-MPC introduces other disadvantages such as a spread frequency spectrum, mainly concentrated at low frequencies, due to the lack of a modulation stage, and requires a high computational effort which increases exponentially with the number of sub-modules, limiting the implementation of FCS-MPC to M3Cs with a reduced number of sub-modules. To account for these drawbacks, a sequential phase-shifted model-predictive-control (PS-MPC) has been proposed for multilevel converters to improve the frequency spectrum and reduce the computational burden of the MPC. The PS-MPC exploits the sequential working principle of a phase-shifted pulse-width-modulation (PS-PWM), which allows the MPC to only optimize the duty-cycle of the switch that is going to be updated next. The PS-MPC was initially implemented in a single-phase flying capacitor converter [22], and then proposed to govern a CHB converter with independent power sub-modules [23], and an M2C in order to include multiple control objectives (ac current, circulating currents and capacitor voltages balance) [24]. Nevertheless, in [22]–[24], the optimal unconstrained solution of the control inputs are saturated and might not be the optimal during transients.

Finally, it is important to highlight that the PS-MPC has not been proposed for the M3C before. This thesis presents the first PS-MPC implemented for an M3C, which is not a trivial implementation due to the model of an M3C has to be derived as a function of the PS-PWM.

M3C current control

The M3C presents multiple currents to be considered and from the application point of view, only the input and output currents are relevant. However, the circulating currents have a key role in the capacitor voltage balance among clusters. Hence, from the control point of view, the input, output and circulating currents must be governed [25].

Input and Output Current Control

The input and output current control is part of the inner control loop of the M3C, so the settling time must be at least ten times faster than the outer control loop.

Regarding the controllers for the input and output currents of the three-phase systems, any standard controller used to govern the three-phase currents can be implemented for this block. For instance, the most used controllers for input and out currents for the M3C are Proportional Integral (PI) [12] and Proportional Resonant (PR) [26].

Circulating Current Control

The circulating currents are used to balance the energy among clusters. These currents present several frequency components. The most common controllers utilized are Proportional (P) [16],

PI [27] and PR [28]. Nonetheless, the circulating current reference present several frequencies and every frequency requires a P/PI/PR controller. Moreover, multiple transformation stages must be applied in order to separate each frequency component [25]. In the last years, an MPC strategy has been proposed for circulating currents to overcome this disadvantage [29].

Cluster Capacitor Voltage Control

The energy among sub-modules must be balanced to properly operate the M3C. This balancing control is divided in three, the total energy balancing (TEB) control, the inter-cluster balancing (ICB) control and the local-cluster balancing (LCB) control of the M3C [25]. Additionally, it is usually included a low-frequency oscillation (LFO) mitigation to operate the converter at low and similar frequencies.

Total Energy Balancing Control

The total energy balancing or TEB control regulates the total stored energy in the M3C. The energy of the M3C is directly related to the capacitor voltage of each sub-module. TEB control generates an active power reference of input or output power. In the literature, the PI is the controller used for TEB control [25], [29]–[31].

Inter-Cluster Balancing Control

The energy among clusters must be regulated to avoid imbalances in the three-phase system currents. Therefore, the inter-cluster balancing or ICB control distributes the power of the M3C among all its clusters, determining the imposition of internal command signals for the circulating currents and/or common-mode voltage (CMV), without affecting the AC ports. However, the ICB should generate minimal circulating currents and CMV to increase the efficiency and power density of the converter. Additionally, both CMV and circulating currents demand additional voltage from the cluster, which must be into account so as not saturate it.

In the literature, the controllers that have been used to generate circulating current references are linear controllers such as PI [16], optimal strategies for re-allocations [32] and even fixed waveforms have utilized [12].

Low-Frequency Oscillation Mitigation

The low-frequency oscillation or LFO mitigation compensates large oscillations in sub-module capacitor voltages by injecting CMV and circulating currents with high harmonic components. It is required only at the critical points of operation, when the M3C operates at a very low frequency, but most acute when these frequencies approach or equal [16].

Local-Cluster Balancing Control

The local-cluster balancing or LCB control locally regulates the capacitor voltage of each SM in their respective cluster. It is usually implemented at the modulation stage with P controllers [17], where a P controller is needed per SM, or sorting strategies to extract more energy from the SMs which have more stored energy [18].

1.3.3 Optimal Control Strategies

In the literature, the optimal controllers applied to power converter are linear-quadratic-regulator (LQR) and model-predictive-control (MPC) [33], [34]. Both consider a system model and a cost function. Nonetheless, the main difference is that the MPC strategies are able to include restrictions in the optimal problem. Additionally, the MPC control can be used for nonlinear systems, unlike LQR control, which can only be applied to linear systems.

Regarding M3Cs, the optimal control strategies applied to M3C are finite-control-set MPC (FCS-MPC) [20] and continuous-control-set MPC (CCS-MPC) [29]. On one hand, the FCS-MPC has only been applied in a simulation environment in order to govern input, output and circulating currents, and balance the floating capacitor voltages, so the effectiveness of this strategy has not been proved in a real-time application. On the other hand, the CCS-MPC proposed in [29] has been implemented to govern circulating currents only.

In the last years, a new predictive strategy has been proposed for multilevel converters, the sequential phase-shifted MPC (sPS-MPC) [22]–[24]. The sPS-MPC belongs to the CCS-MPC and has demonstrated to be an alternative for multilevel converters due to its reduced computational burden, scalability and good performance in comparison with other predictive strategies. Nevertheless, the sPS-MPC has never been proposed for M3Cs before.

1.4 Proposal

The contribution of this research is focused on the formulation of a predictive control strategy for the modular multilevel matrix converter, composed by a inner control strategy and a outer control strategy which are independent.

1.4.1 Hypotheses

H1: A control strategy based on predictive control allows to govern currents and balance capacitor voltages of an M3C over a wide frequency range, a fixed spectra and a high scalability.

H2: An optimal reference generator for circulating currents and/or common-mode voltage improves the steady-state performance of the M3C, specifically the capacitor voltage oscillations and/or maximum cluster currents, and operates over a wide frequency range.

Both hypothesis are going to be compared with a control strategy and a reference generator based on linear controllers utilized in the state of the art.

1.4.2 Objectives

In order to prove or refute the proposed hypothesis, the general objective is the development of an optimal control strategy for M3C, which includes an optimal internal control based on predictive control and an optimal reference generator, for operating M3C over a wide frequency range for input and output three-phase systems.

The specific objective can be expressed as:

1. To analyze the dynamic model of currents and voltages of the M3C.
2. To design an internal control strategy based on predictive control strategy.
3. To evaluate the performance through simulations of the proposed inner control strategy.
4. To design an optimal reference generator for inner control.
5. To evaluate the performance through simulations of the proposed control strategy, including the optimal reference generator and the inner control based on optimal control strategy.
6. To evaluate the performance in a prototype of the proposed control strategies.

1.4.3 Methodology

In order to prove or refute the hypothesis, the following steps are followed to successfully accomplish the different objectives:

1. Theoretical analysis and control strategy design:

   First, the necessary conditions for the M3C operation are theoretically analyzed. Based on the theoretical analysis, suitable control strategies are proposed for the proper operation of the converter.

2. Control strategy evaluation through simulation:

After designing possible control strategies based on the analyzed models, they are tested in simulation using specific software such as PLECS or Matlab/Simulink. In this way, the proposed control strategies can be validated under different operating conditions such as steady-state and dynamic response under sudden changes.

3. Design and implementation of the strategy in laboratory prototypes:

   Next, based on the results and tests from the simulations, an experimental prototype is designed and constructed to validate the proposed control strategy in real-time. This involves component sizing, electronic board design, and programming of the control platform.

4. Analysis of obtained experimental results:

   This stage involves conducting tests under different operating conditions in real-time using the laboratory prototype. The objective is to validate and compare the previously performed simulation tests.

5. Dissemination and publication of results and conclusions:

   Finally, the development of this project includes the periodic publication of the obtained results to contribute to the state-of-the-art in the field of ac-ac converters, specifically control strategies for the M3C.

The mentioned steps of the methodology are applied to the optimal inner control and the optimal reference generator. Finally, the effectiveness of the proposals are analyzed by considering the following points:

- Steady-state performance.
- Steady-state error.
- Voltage and current ripple.
- Compliance of constraints.
- Dynamic performance.
- Output frequency performance.
- Three-phase system currents.
- Three-phase system powers.
- Total harmonic distortion of converter output current.
- Weighted total harmonic distortion of converter output current.
- Total harmonic distortion of converter output voltage.
- Weighted total harmonic distortion of converter output voltage.
- Floating point per second required by the strategy.

1.5 Summary of Contributions

1.5.1 Novel Contribution

In this section, a list of the main contributions to the literature of this research are presented.

1. An inner controller that controls the currents and regulates the capacitor voltages of an M3C based on FCS-MPC (see Chapter 2). This proposal unifies the control structure of cluster currents and local cell balancing controls; reduces the average cell switching frequency; tracks any current waveform; considers the coupling among cluster current and capacitor voltages; and is feasible for an experimental implementation. Moreover, this proposal has been tested up to prediction horizon four, comparing its performance as a function of the different horizons. Experimental results have been performed in a 36-sub-module M3C prototype to prove the previously mentioned benefits.

2. An inner controller that controls the currents and regulates the capacitor voltages of an M3C based on PS-MPC (see Chapter 3). This proposal unifies the control structure of input, output and circulating currents and local cell balancing controls; reduces the computational burden; increases the scalability; and presents a fast closed-loop dynamic response with low distortion. The proposed predictive strategy is validated in a prototype with 36 sub-modules proving the previously mentioned advantages.

3. An outer controller that generates circulating current references to balance the energy among cluster of an M3C (see Chapter 4). This proposal obtains the optimal circulating current component per cluster considering the feasible current limits of each cluster as constraints in the optimal problem, so the safe operation of the M3C does not depend on the inner controller tuning since the bound constraints are already included in the optimal problem. Experimental results are provided to verify its performance and effectiveness of the proposed constrained ICB control for the M3C.

4. An outer controller that generates not only circulating current references but CMV reference to balance the energy among cluster of an M3C (see Chapter 5). This proposal achieves the inter-cluster balancing control by optimizing the circulating current component per cluster and then the common-mode voltage of the converter iteratively. The inclusion of common-mode voltage allows to mitigate capacitor voltage oscillations in critical points, such as low frequency operation and equal frequencies. Additionally, the cluster energies are derived in the original framework, which highly simplifies the tuning of the weighting factors in comparison with literature. Moreover, constraints are considered in the optimal control problem to ensure that the generated circulating currents do not impact input and output currents. Experimental results are presented to validate the the contributions of the ICB control based on circulating current and CMV for an M3C.

1.5.2 Publications

Publications: Journal Articles Accepted

1. **R. H. Cuzmar**, A. Mora, J. Pereda, and R. P. Aguilera, "An Improved Reference Generator Based on MPC of Circulating Currents and Common-Mode Voltage for Modular Multilevel Matrix Converters," in *IEEE Transactions on Industrial Electronics*. **Q1 Journal**. Impact Factor of 8.41.

2. **R. H. Cuzmar**, A. Mora, J. Pereda, R. P. Aguilera, P. Poblete and S. Neira, "Computationally Efficient MPC for Modular Multilevel Matrix Converters Operating With Fixed Switching Frequency," in *IEEE Open Journal of the Industrial Electronics Society*, vol. 4, pp. 748-761, 2023, doi: 10.1109/OJIES.2023.3347101. **Q1 Journal**. Impact Factor of 6.75.

3. **R. Cuzmar**, A. Montenegro, A. Mora, J. Pereda and R. P. Aguilera, "Constrained MPC for Intercluster Energy Control of Modular Multilevel Matrix Converters," in *IEEE Transactions on Industrial Electronics*, vol. 71, no. 7, pp. 7766-7776, July 2024, doi: 10.1109/TIE.2023.3303641. **Q1 Journal**. Impact Factor of 8.41.

4. **R. H. Cuzmar**, A. Mora, J. Pereda, P. Poblete and R. P. Aguilera, "Long-Horizon Sequential FCS-MPC Approaches for Modular Multilevel Matrix Converters," in *IEEE Transactions on Industrial Electronics*, vol. 71, no. 5, pp. 5137-5147, May 2024, doi: 10.1109/TIE.2023.3286013. **Q1 Journal**. Impact Factor of 8.41.

5. **R. H. Cuzmar**, J. Pereda and R. P. Aguilera, "Phase-Shifted Model Predictive Control to Achieve Power Balance of CHB Converters for Large-Scale Photovoltaic Integration," in *IEEE Transactions on Industrial Electronics*, vol. 68, no. 10, pp. 9619-9629, Oct. 2021, doi: 10.1109/TIE.2020.3026299. **Q1 Journal**. Impact Factor of 8.41.

Publications: Conference Articles Accepted

- **R. H. Cuzmar**, P. Poblete, R. P. Aguilera, J. Pereda and D. D. -C. Lu, "Power Balance of a Delta-Connected CHB Converter with MPC for Photovoltaic Systems," *2023 IEEE International Future Energy Electronics Conference (IFEEC)*, Sydney, Australia, 2023, pp. 305-310, doi: 10.1109/IFEEC58486.2023.10458456.

Publications: Collaborations

- P. Poblete, J. Gajardo, **R. H. Cuzmar**, R. P. Aguilera, J. Pereda, D. Lu and A. M. Marquez "Predictive Optimal Variable-Angle PS-PWM Strategy for Cascaded H-Bridge Converters," in *IEEE Transactions on Industrial Electronics*,
doi: 10.1109/TIE.2024.3370998. **Q1 Journal**. Impact Factor of 8.41.

- P. Poblete, S. Neira, **R. Cuzmar**, R. P. Aguilera, A. Mora and J. Pereda, "Closed-Loop Performance Improvement for MMCs Based on Optimal Reference Governor," *2021 IEEE 12th Energy Conversion Congress & Exposition - Asia (ECCE-Asia)*, Singapore, Singapore, 2021, pp. 2292-2297,
doi: 10.1109/ECCE-Asia49820.2021.9479378.

- S. Neira, P. Poblete, **R. Cuzmar**, J. Pereda and R. P. Aguilera, "Sequential Phase-Shifted Model Predictive Control for a Multilevel Converter with Integrated Battery Energy Storage," *2020 IEEE 11th International Symposium on Power Electronics for*

Table 1.2: Structure and relation of this thesis.

Chapter	Journal	Description	Hypothesis		Contribution			
			1	2	1	2	3	4
2	TIE 2024	Long horizon FCS-MPC	✓		✓			
3	OJIES 2023	Sequential PS-MPC	✓			✓		
4	TIE 2024	Constrained CC generator		✓			✓	
5	TIE	CC and CMV generator		✓				✓

Distributed Generation Systems (PEDG), Dubrovnik, Croatia, 2020, pp. 29-34, doi: 10.1109/PEDG48541.2020.9244410.

1.6 Thesis structure

The body of this thesis is comprised by 6 chapters. Chapter 1, the present chapter, presents the the contributions, main and specific objectives of this research. Additionally, includes the state of the art in terms of modular multilevel cascaded converters for AC-to-AC conversion and the advantages of the modular multilevel matrix converter in comparison with the others. Moreover, in this chapter, the controllers require to govern the M3C and used in the literature are mentioned. The following chapters and the relation with the journal articles are summarized in Table 1.2.

Chapter 2 presents an inner controller for the M3C, the proposed inner controller is based on a long-horizon finite-control-set model-predictive-control and compares it with two predictive strategies from the literature. The proposal is validated by using a prototype with 36 submodules.

This chapter resulted in the following publication:

- **R. H. Cuzmar**, A. Mora, J. Pereda, P. Poblete and R. P. Aguilera, "Long-Horizon Sequential FCS-MPC Approaches for Modular Multilevel Matrix Converters," in *IEEE Transactions on Industrial Electronics*, vol. 71, no. 5, pp. 5137-5147, May 2024, doi: 10.1109/TIE.2023.3286013.

Chapter 3 describes an inner controller for the M3C, the proposed strategy is based on phase shifted model predictive control strategy and two existing control strategies, presented in previous works to be used as benchmark. This predictive strategy considers the coupling among states and decouples the cluster currents in input, output and circulating currents in the $\alpha\beta 0-$framework. In addition, the references for the proposal are derived. Finally, experimental results are presented to show the effectiveness of the proposed strategy.

This chapter resulted in the following publication:

- **R. H. Cuzmar**, A. Mora, J. Pereda, R. P. Aguilera, P. Poblete and S. Neira, "Computationally Efficient MPC for Modular Multilevel Matrix Converters Operating With Fixed Switching Frequency," in *IEEE Open Journal of the Industrial Electronics Society*, vol.

4, pp. 748-761, 2023, doi: 10.1109/OJIES.2023.3347101.

Chapter 4 shows the proposed outer control strategy for the M3C, a constrained circulating current generator to balanced the energy among clusters of the M3C. Experimental results have been performed to prove the effectiveness of the proposal.

This chapter resulted in the following publication:

- **R. Cuzmar**, A. Montenegro, A. Mora, J. Pereda and R. P. Aguilera, "Constrained MPC for Intercluster Energy Control of Modular Multilevel Matrix Converters," in *IEEE Transactions on Industrial Electronics*, vol. 71, no. 7, pp. 7766-7776, July 2024, doi: 10.1109/TIE.2023.3303641.

Chapter 5 presents an improved version of the previous generator. In this case, the inter-cluster balancing control considers not only circulating currents but common-mode voltage as well. The common-mode voltage generator allows to operate the M3C at low and equal frequencies, which are critical points for this converter. This reference generator has been tested in an M3C prototype with 36 SMs to prove its features.

This chapter resulted in the following publication:

- **R. Cuzmar**, A. Mora, J. Pereda and R. P. Aguilera, "An Improved Reference Generator Based on MPC of Circulating Currents and Common-Mode Voltage for Modular Multilevel Matrix Converters," in *IEEE Transactions on Industrial Electronics*.

Chapter 6 presents the conclusions of this research and future work.

Chapter 2

LONG-HORIZON SEQUENTIAL FCS-MPC APPROACHES FOR MODULAR MULTILEVEL MATRIX CONVERTERS

2.1 Introduction

Modular multilevel cascaded converters (MMCCs) are an attractive technology for medium voltage and high power applications due to its high modularity, performance and capability to work directly at medium and high voltages [11], [12], [35]–[37]. The main exponents of MMCCs are the cascaded H-bridge (CHB), the modular multilevel converter (M2C), and the modular multilevel matrix converter (M3C).

The back-to-back M2C (B2B-MMC) and the M3C are the MMCC choices for ac-ac applications such as power system interconnections (50-60 Hz), low frequency ac transmission systems (LFAC), wind energy conversion systems (WECS) and medium/high voltage motor drives for marine propulsion, mills, pumps, conveyors, among other applications.

The M3Cs, also known as triple-star bridge cells (TSBC), are promising for direct ac-ac power conversion because they do not require a high voltage dc-link [11], [12], and needs less cells in comparison with the M2C-B2B. Additionally, the M3Cs excels over B2B-M2Cs in LFAC transmission systems, WECS and low speed motor drives, showing a better performance at low frequency operation [15] due to capacitor oscillations are lower at low frequencies [10]. However, the M3C presents several challenges such as highly coupled internal states, complex control and balance of several floating capacitors, a big number of control signals, and capacitor voltage oscillations at specific frequencies. Therefore, its implementation can be challenging in high voltage application that requires a large number of cells. [16], [17], [38].

Several control strategies have been proposed to tackle these problems and govern the M3C. A standard way to control an M3C is by designing and implementing multiple control loops based on proportional-integral (PI) controllers working in multiple transformed reference frames to decouple each state [11], [12], [16], [18]. However, the use of multiple single-input-single-output (SISO) controllers for a highly coupled system, which has more variables than degrees of freedom, reduces the robustness of the control in comparison with a multiple-inputs-multiple-

outputs (MIMO) controller [19]. Additionally, linear controllers are tuned for a specific operating condition, degrading the closed-loop performance when the converter operates far from the desired point.

Alternatively, finite-control-set model-predictive-control (FCS-MPC) has been proposed in the literature to solve the aforementioned SISO control limitations [20], [21]. However, since the FCS-MPC does not consider a modulation stage, it forces the converter to operate with a spread voltage frequency spectra, which is mainly concentrated at low frequencies with a high average cell switching frequency. In term of implementation, the main limitation of this control strategy is its computational effort requirement, which increases exponentially with the number of cells. Consequently, the implementation of standard FCS-MPC strategies is limited to converters with a reduced number of cells. That is why FCS-MPC has only been tested in simulation for the M3C.

This work proposes a long-horizon sequential FCS-MPC to govern the M3C without decoupling the dynamics of its internal states. The proposed controller provides a simplified control structure and provides a fast transient response at multiple frequencies, unlike standard SISO strategies that require a controller per frequency. Moreover, by considering the common-mode voltage as a known disturbance, the proposed strategy governs independently each cluster, reducing the total possible combinations and significantly reducing the required computational effort. The main contributions of this work are the following: i) fast closed-loop transient response comparable with standard FCS-MPC strategies; ii) reduced average cell switching frequency; iii) tracking of any current waveform; iv) consideration of the coupling among current and capacitor voltages; v) unified control structure; and vi) scalability and feasibility of experimental implementation.

Experimental results are provided to verify the performance and the effectiveness of the proposal, showing a fast dynamic response, a low harmonic distortion, and a suitable computational burden. The functionality of the proposed control was verified in steady state, under a sudden power step and under different operating frequencies, obtaining adequate results that make it attractive for applications such as low frequency ac transmission systems (LFAC), wind energy conversion systems (WECS), and variable speed drives.

2.2 Modular Multilevel Matrix Converter Model

The M3C topology is composed by nine stacks or clusters to interconnect the $uvw-$ and the $abc-$ three-phase ac-ports (Fig. 2.1). Each cluster is formed by connecting several H-bridges cells or sub-modules (SMs) in cascade manner along with a series cluster inductor. Additionally, each cell has a floating capacitor in its dc-link.

To properly operate an M3C, it is required to control: the currents of both ac-ports; the four circulating currents; and the capacitor voltages of each cell. The regulation of the capacitor voltages considers three energy balancing strategies: i) the inner energy of the M3C; ii) the energy balance among clusters; and iii) the intra-cluster energy balance.

The latter is called local cell balancing (LCB) control and the other two are part of the cluster capacitor voltage (CCV) control [16], [25].

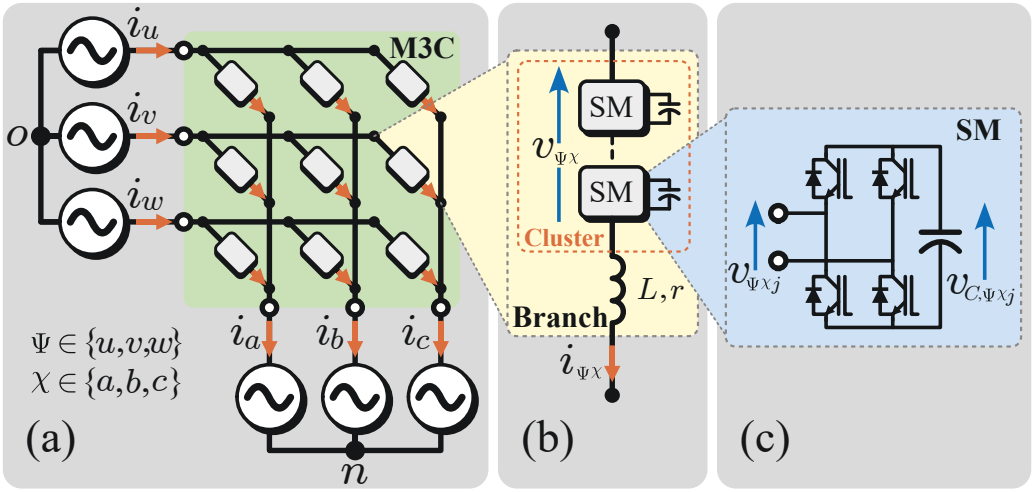

Figure 2.1: The M3C topology: (a) circuit diagram; (b) N-cell cluster; and (c) full-bridge-based sub-module.

2.2.1 Continuous-Time Model

Considering an M3C connected between two three-phase ports as represented in Fig. 2.1, the continuous-time dynamic model of each converter cluster current, $i_{\Psi\chi}(t)$, can be expressed via:

$$L\frac{\mathrm{d}}{\mathrm{d}t}i_{\Psi\chi}(t) = v_{\Psi}(t) - v_{\Psi\chi}(t) - ri_{\Psi\chi}(t) - v_{\chi}(t) - v_{n0}(t) \tag{2.1}$$

where $\Psi \in \{u, v, w\}$ and $\chi \in \{a, b, c\}$. Here, L and r are the inductance and the resistance of the cluster filter, respectively. Additionally, the terms $v_{\Psi}(t)$ and $v_{\chi}(t)$ stand for the $uvw-$ and the output-port voltage in each phase, respectively; $v_{\Psi\chi}(t)$ represents the output voltage per cluster; and $v_{n0}(t)$ denotes the common-mode voltage. The cluster output voltage in a given arm is formed by the sum of the individual cell voltages over the set $\mathcal{N} = \{1, \ldots, N\}$, i.e.:

$$v_{\Psi\chi}(t) = \sum_{j\in\mathcal{N}} v_{\Psi\chi j}(t) \tag{2.2}$$

where each cell output voltage is given by:

$$v_{\Psi\chi j}(t) = v_{C,\Psi\chi j}(t)\, u_{\Psi\chi j}(t) \tag{2.3}$$

where $u_{\Psi\chi j}(t) \in \{-1, 0, 1\}$ is the switching state of the j-th cell in the $\Psi\chi-$cluster . Moreover, the dynamic model of each capacitor voltage, $v_{C,\Psi\chi j}(t)$, is given by:

$$\frac{\mathrm{d}}{\mathrm{d}t}v_{C,\Psi\chi j}(t) = \frac{1}{C}i_{\Psi\chi}(t)\, u_{\Psi\chi j}(t) \tag{2.4}$$

For the sake of simplicity, we define $\kappa \in \{\Psi, \chi\}$ to refer the κ-cluster hereinafter. Thus, by introducing the switching state vector as the system input:

$$\boldsymbol{u}_{\kappa} = \begin{bmatrix} u_{\kappa 1} & \cdots & u_{\kappa N} \end{bmatrix}^{\mathrm{T}} \in \{-1, 0, 1\}^{N}, \tag{2.5}$$

the continuous-time dynamic model of the κ-cluster shown in Fig. 2.1(b) is given by:

$$\frac{\mathrm{d}}{\mathrm{d}t}i_{\kappa} = -\frac{r}{L}i_{\kappa} - \frac{1}{L}\mathbf{v}_{C\kappa}^{\mathrm{T}}\boldsymbol{u}_{\kappa} + \frac{1}{L}v_{g\kappa} \tag{2.6a}$$

$$\frac{\mathrm{d}}{\mathrm{d}t}\mathbf{v}_{C\kappa} = \frac{1}{C}i_{\kappa}\boldsymbol{u}_{\kappa} \tag{2.6b}$$

where $\mathbf{v}_{C\kappa} = \begin{bmatrix} v_{C\kappa 1} & \dots & v_{C\kappa N} \end{bmatrix}^{\mathrm{T}}$, and $v_{g\kappa} = v_{\Psi} - v_{\chi} - v_{no}$.

It is important to highlight that in (2.6), the switching state vector $\boldsymbol{u}_{\kappa}$ is multiplying both the branch current i_{κ} and the floating capacitor voltages $\mathbf{v}_{C\kappa}$, establishing a bilineal model for every cluster. Moreover, usually for M3Cs, a higher level control determines the common-mode voltage (CMV) to be injected to balance the cluster capacitor voltages and mitigate low-frequency oscillations [25]. Therefore, the CMV v_{no} can be modelled as a known variable in (2.6a).

2.2.2 Discrete-Time Cluster Model

This work formulates a FCS-MPC strategy to control the current and the capacitor voltages of each cluster independently. Therefore, the system state, at each sampling instant k, is chosen as:

$$\boldsymbol{x}_{\kappa}(k) = \begin{bmatrix} i_{\kappa}(k) & \mathbf{v}_{C\kappa}^{\mathrm{T}}(k) \end{bmatrix}^{\mathrm{T}} \in \mathbb{R}^{1+N} \tag{2.7}$$

Discretization methods for bilinear systems, as per (2.6), are imperfect and usually require a higher computational burden than those for linear systems. However, when the sampling frequency is high enough, different discretization methods do not highly differ in their performance [39]. Therefore, this work applies the Forward Euler discretization method with a sampling period T_s to (2.6), obtaining the following discrete-time model:

$$\boldsymbol{x}_{\kappa}(k+1) = \boldsymbol{A}\boldsymbol{x}_{\kappa}(k) + \boldsymbol{B}_{\kappa}(k)\boldsymbol{u}_{\kappa}(k) + \boldsymbol{g}_{\kappa}(k) \tag{2.8}$$

where

$$\begin{aligned} \boldsymbol{A} &= \begin{bmatrix} 1 - T_s\frac{r}{L} & \mathbf{0}_{1\times N} \\ \mathbf{0}_{N\times 1} & \mathbf{1}_{N\times N} \end{bmatrix} \\ \boldsymbol{B}_{\kappa}(k) &= \begin{bmatrix} -\frac{T_s}{L}\mathbf{v}_{C\kappa}^{\mathrm{T}}(k) \\ \frac{T_s}{C} i_{\kappa}(k)\boldsymbol{I}_{N\times N} \end{bmatrix} \;;\; \boldsymbol{g}_{\kappa}(k) = \begin{bmatrix} \frac{T_s}{L} v_{g\kappa}(k) \\ \mathbf{0}_{N\times 1} \end{bmatrix}. \end{aligned} \tag{2.9}$$

2.3 FCS-MPC of M3Cs

This section formulates the proposed long-horizon sFCS-MPC to govern each cluster independently. The formulation allows the controller to regulate the cell capacitor voltages and the cluster current in a unified and straightforward manner. Thus, the control targets per cluster are given by the cluster current and cell capacitor voltages, so the state references are given by

$$\boldsymbol{x}_{\kappa}^{\star}(k) = \begin{bmatrix} i_{\kappa}^{\star}(k) & \mathbf{v}_{C\kappa}^{\star\,\mathrm{T}}(k) \end{bmatrix}^{\mathrm{T}}. \tag{2.10}$$

2.3.1 Standard FCS-MPC

In order to track this multi-variable objective the standard quadratic cost function is considered

$$J_{\kappa}(k) = \left\| \boldsymbol{e}_{\kappa x}(k+1) \right\|_{\boldsymbol{Q}}^{2} + \lambda\, e_{\kappa u}^{2}(k) \tag{2.11}$$

where

$$\begin{aligned} \boldsymbol{e}_{\kappa x}(k+1) &= \boldsymbol{x}_{\kappa}(k+1) - \boldsymbol{x}_{\kappa}^{\star}(k+1) \in \mathbb{R}^{1+N} \\ e_{\kappa u}(k) &= \mathbf{1}^{\mathrm{T}}\boldsymbol{u}_{\kappa}(k) - u_{\kappa}^{\star}(k) \in \mathbb{R}. \end{aligned} \tag{2.12}$$

In (2.11), $\|\boldsymbol{e}_{\kappa x}\|^2_{\boldsymbol{Q}} = \boldsymbol{e}^{\mathrm{T}}_{\kappa x}\boldsymbol{Q}\boldsymbol{e}_{\kappa x}$ denotes the weighted quadratic norm of states tracking error $\boldsymbol{e}_{\kappa x}$, and matrix $\boldsymbol{Q} = \mathrm{diag}\left([\sigma_1 \quad \sigma_2\mathbf{1}_{1\times N}]\right)$ is used to trade-off the tracking error between the current and capacitor voltages in every cluster. Additionally, the non-negative parameter λ regulates the states tracking error $\boldsymbol{e}_{\kappa x}$ and the input effort $e_{\kappa u}$. Since $u^{\star}_{\kappa}(k) \in \mathbb{R}$ is the required cluster steady-state duty-cycle to maintain the SMs capacitor voltage and the cluster current in the desired steady-state $\boldsymbol{x}^{\star}_{\kappa}(k+1)$ presented in (2.10), the parameter λ allows modifying the response of the closed-loop system [40]. Further details regarding the desired steady-state duty-cycle is given in Section 2.4.3.

By considering the cluster model (2.8) and the cost function (2.11) it is possible to formulate a standard single-step horizon FCS-MPC of an M3C, considering a finite set of 9×3^N possible control actions.

2.3.2 Proposed Long-Horizon Sequential FCS-MPC

This chapter proposes a long-horizon sequential FCS-MPC for an M3C. The control targets per cluster for a long-horizon are given by the cluster current and cell capacitor voltages, so the state references for a long-horizon model are the same as the one presented for single-horizon model (2.10).

In [20], the cluster model considers the update of only one cell, reducing the possible combinations because the combinations increase exponentially with the number of cells in the standard FCS-MPC. Although the cluster is composed of several cells, considering a sequential update of the switching states makes it possible to reduce the total available combinations because only one cell is optimized in every sampling period.

Following the sequential updating principle introduced in [20], to formulate the long-horizon predictive control strategy, we present the control input to be optimized in every sampling time k as follows

$$\boldsymbol{U}_{\kappa}(k) = \begin{bmatrix} u_{\kappa,j}(0) & \dots & u_{\kappa,j+H-1}(H-1) \end{bmatrix}^{\mathrm{T}}, \tag{2.13}$$

which represents the controller switching sequence to decide over horizon $\mathcal{H}{=}\{0,\dots,H-1\}$, with $H{\leq}N$, as illustrated in Fig. 2.2(a) for a horizon length $H = 3$. In (2.13), the sampling time k was omitted for simplicity, and the switching states are evaluated from SM j to $j{+}H{-}1$.

Thus, by taking into account that only the ℓth SM's switching state is updated at horizon $h \in \mathcal{H}$, the predictive tracking error can be explicitly rewritten in terms of switching state to be updated as:

$$\boldsymbol{e}_{\kappa x}(h{+}1) = \mathbf{A}\boldsymbol{x}_{\kappa}(h) + \mathbf{b}_{\ell}(h)u_{\kappa\ell}(h) + \boldsymbol{\eta}_{\ell}(h) - \boldsymbol{x}^{*}_{\kappa}(h+1) \tag{2.14}$$

where $\mathbf{b}_i(h)$ is the ith column vector in matrix $\boldsymbol{B}_{\kappa}(h)$, and $\boldsymbol{\eta}_{\ell}(h)$ is a known disturbance given by:

$$\boldsymbol{\eta}_{\ell}(h) = \sum_{\forall i \neq \ell} \mathbf{b}_i(h)u_{\kappa i}(h-1) + \boldsymbol{g}_{\kappa}(h) \tag{2.15}$$

Therefore, the optimization problem underlying the proposed long-horizon sequential FCS-

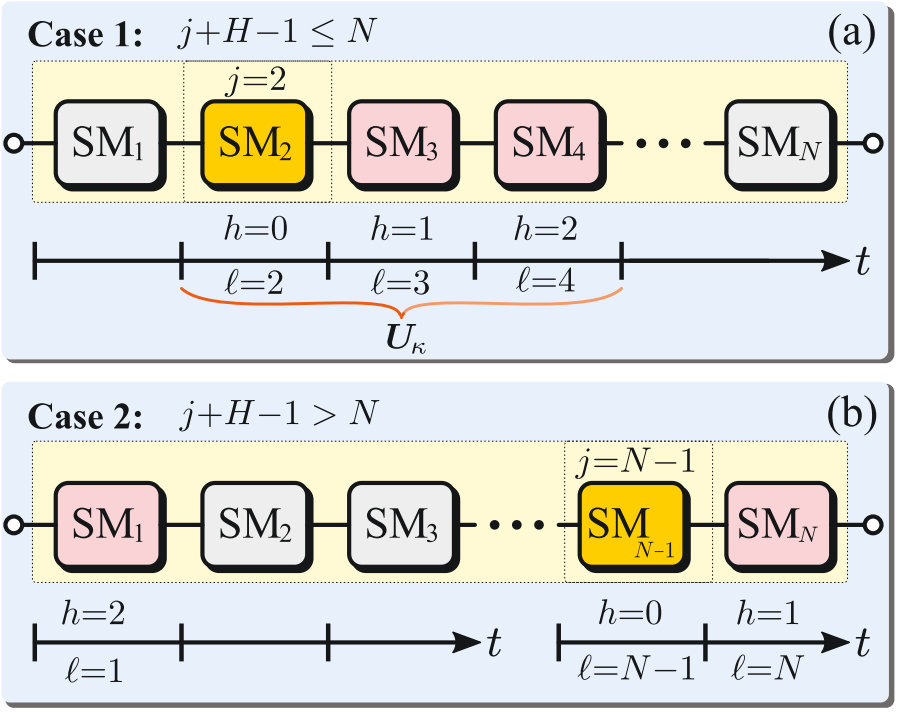

Figure 2.2: Optimization process over horizon length $H = 3$: (a) sub-modules to evaluate when $j + H - 1 \leq N$; and (b) sub-modules to evaluate and reset when $j + H - 1 > N$.

MPC can be stated as:

$$\min_{\boldsymbol{U}_\kappa} \sum_{h\in\mathcal{H}} \left(\|\boldsymbol{e}_{\kappa x}(h+1)\|^2_{\boldsymbol{Q}_h} + \lambda_h e^2_{\kappa u}(h) \right) \tag{2.16a}$$

$$\text{s. t. } (2.14) \tag{2.16b}$$

$$\boldsymbol{U}_\kappa \in \{-1, 0, +1\}^H \tag{2.16c}$$

$$|u_{\kappa,j}(h) - u_{\kappa,j}(h-1)| \leq 1, \tag{2.16d}$$

As shown in the cost function in (2.16a), the weight λ_h regulates the states tracking error $\boldsymbol{e}_{\kappa x}$ and the input effort $e_{\kappa u}$ over the prediction horizon $h\in\mathcal{H}$. Analogously, matrix $\boldsymbol{Q}_h = \text{diag}\left([\sigma_{1h} \quad \sigma_{2h}\mathbf{1}_{1\times N}]\right)$ regulates the tracking error between the current and capacitor voltages.

In the stated optimal control problem (2.16), condition (2.16d) is included to only allow switching transitions between consecutive levels, producing a variable feasible control set $\mathbb{U}$ per sampling time, whose cardinality $M = |\mathbb{U}|$ can be bounded between 2^H and 3^H for every cluster. As shown in the control diagram presented in Fig. 2.3, the proposed control method performs an enumeration search algorithm in which the predictions of the system state over the feasible control set are evaluated into the cost function. Specifically, the algorithm first step updates the feasible control set $\mathbb{U} = \{\boldsymbol{U}^{(1)}_\kappa, \ldots, \boldsymbol{U}^{(M)}_\kappa\}$ by taking into account the previous switching state $\boldsymbol{u}_\kappa(k-1)$ and constraints (2.16c) and (2.16d). Then, the controller predicts the tracking errors over the prediction horizon and computes the cost function value for every candidate control input, i.e., $J^{(m)}_\kappa$ with $m \in \{1, \ldots, M\}$. Finally, the optimal control sequence $\boldsymbol{U}^\star_k(k)$ is the one that produces the minimal cost function value.

It is worth highlighting that, although the switching states are evaluated from the SM j to the one $j + H - 1$, only the first element in $\boldsymbol{U}^\star_k(k)$ [see (2.13)] is updated in every sampling instant,

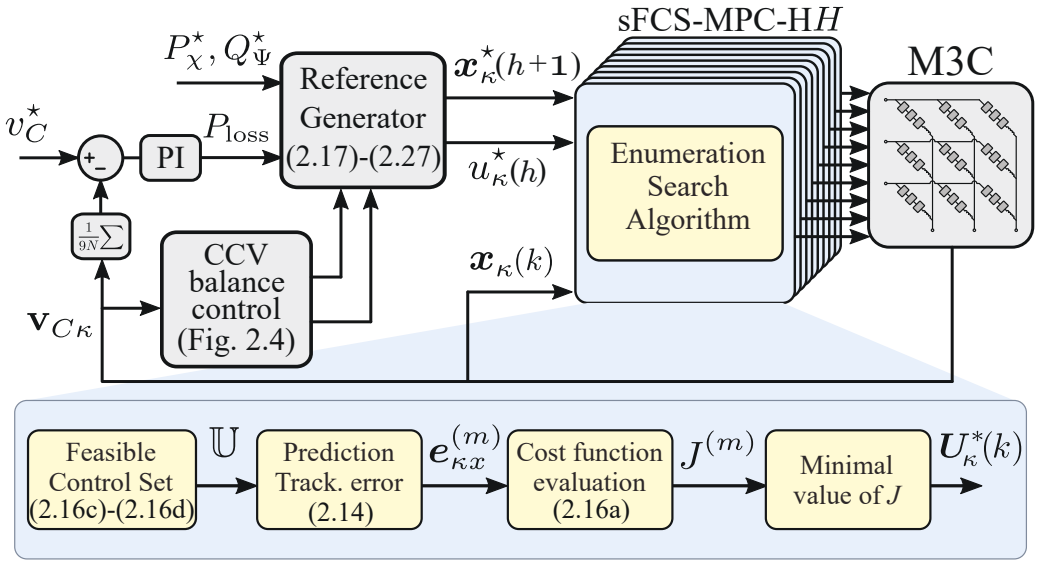

Figure 2.3: Proposed control scheme.

as illustrated in Fig. 2.2. This control action update follows the receding-horizon MPC working principle [41], [42]. Moreover, since subindex ℓ denotes the SM to be optimized at the horizon $h \in \mathcal{H}$, it is defined as $\ell = j + h$ and its value is reset when $\ell > N$, as illustrated in Fig. 2.2(b).

The sequential FCS-MPC Horizon H of an M3C is referred to as sFCS-MPC-HH.

2.4 References Design

The overall control strategy is shown in Fig. 2.3. This section aims to obtain the state references, $\boldsymbol{x}^\star_\kappa(h{+}1)$, considering current of both ports, capacitor voltages and the CCV balancing controller requirements as:

$$\boldsymbol{x}^\star_\kappa(h+1) = \begin{bmatrix} i^\star_\kappa(h+1) & \mathbf{v}^{\star\,\mathrm{T}}_{C\kappa}(h+1) \end{bmatrix}^{\mathrm{T}} \in \mathbb{R}^{1+N} \tag{2.17}$$

where each element in $\mathbf{v}^\star_{C\kappa}(h+1)$ is considered constant and equal to $v^\star_C$. Additionally, the required steady-state control input $u^\star_\kappa(h)$ is also determined in this section.

The current references are designed in the double-$\alpha\beta$0-framework (D-$\alpha\beta$0). In order to transform the D-$\alpha\beta$0 currents into arm currents, the power-invariant Clark Transformation, $\left[\boldsymbol{C}^{\alpha\beta0}\right]$, is utilized:

$$\begin{bmatrix} i^\star_{ua} & i^\star_{va} & i^\star_{wa} \\ i^\star_{ub} & i^\star_{vb} & i^\star_{wb} \\ i^\star_{uc} & i^\star_{vc} & i^\star_{wc} \end{bmatrix} = \left[\boldsymbol{C}^{\alpha\beta0}\right]^T \begin{bmatrix} i^\star_{\alpha\alpha} & i^\star_{\beta\alpha} & i^\star_{0\alpha} \\ i^\star_{\alpha\beta} & i^\star_{\beta\beta} & i^\star_{0\beta} \\ i^\star_{\alpha0} & i^\star_{\beta0} & 0 \end{bmatrix} \left[\boldsymbol{C}^{\alpha\beta0}\right]. \tag{2.18}$$

2.4.1 Input and Output Current Reference

The reference for the input and output currents are designed in the $\alpha\beta$0-framework. By considering an active power references for the output system, a symmetric current reference is obtained:

$$\boldsymbol{i}^\chi_{\alpha\beta0} = \frac{\sqrt{2}P^\star_\chi}{\sqrt{3}r_L} \begin{bmatrix} \sin(\omega_\chi t) \\ -\cos(\omega_\chi t) \end{bmatrix} \tag{2.19}$$

where $P^\star_\chi$ is the active power reference for a passive load with inductance L_L and resistance r_L. Then, in order to regulate the average energy of the converter, the required input active power

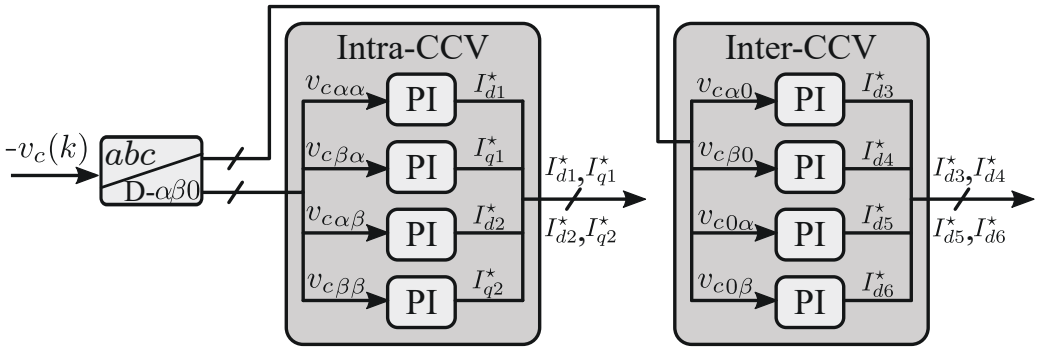

Figure 2.4: Intra-CCV and inter-CCV balancing control [11].

$P^\star_\Psi$ must be the sum of the desired output active power $P^\star_\chi$ and the power consumed by the M3C, P_{loss}. This leads to the following expression for the input current reference:

$$\boldsymbol{i}^\Psi_{\alpha\beta0} = \frac{1}{{v^\Psi_\alpha}^2 + {v^\Psi_\beta}^2} \begin{bmatrix} v^\Psi_\alpha & v^\Psi_\beta \\ v^\Psi_\beta & -v^\Psi_\alpha \end{bmatrix} \begin{bmatrix} P^\star_\chi + P_{\text{loss}} \\ Q^\star_\Psi \end{bmatrix} \tag{2.20}$$

The power losses P_{loss} are obtained by a PI controller as shown in Fig. 2.3, which allows to regulate the internal energy of the converter, being part of the CCV control.

Finally, the current references in the D-$\alpha\beta$0 framework for both ports are given by:

$$\begin{bmatrix} i^\star_{\alpha0} & i^\star_{\beta0} & i^\star_{0\alpha} & i^\star_{0\beta} \end{bmatrix}^{\text{T}} = \frac{1}{\sqrt{3}} \begin{bmatrix} \boldsymbol{i}^\Psi_{\alpha\beta0} \\ \boldsymbol{i}^\chi_{\alpha\beta0} \end{bmatrix}. \tag{2.21}$$

2.4.2 Circulating Current Reference

The CCV control considers the energy balance among clusters, designing a proper circulating current. By analyzing the cluster powers and cluster voltages in the D-$\alpha\beta$0-framework the waveform for the circulating current can be deduced as is presented in [11], [12], [25]. In this work, the CCV balancing control introduced in [11] is implemented, where every circulating current possess two components as follow:

$$\begin{bmatrix} i^\star_{\alpha\alpha} \\ i^\star_{\alpha\beta} \\ i^\star_{\beta\alpha} \\ i^\star_{\beta\beta} \end{bmatrix} = \begin{bmatrix} i^\star_{\alpha\alpha1} + i^\star_{\alpha\alpha2} \\ i^\star_{\alpha\beta_1} + i^\star_{\alpha\beta_2} \\ i^\star_{\beta\alpha_1} + i^\star_{\beta\alpha_2} \\ i^\star_{\beta\beta_1} + i^\star_{\beta\beta_2} \end{bmatrix} \tag{2.22}$$

where the first component is given by the intra-CCV balancing control (Fig. 2.4):

$$\begin{bmatrix} i^\star_{\alpha\alpha1} \\ i^\star_{\alpha\beta_1} \\ i^\star_{\beta\alpha_1} \\ i^\star_{\beta\beta_1} \end{bmatrix} = \begin{bmatrix} I^\star_{d1}\cos(\omega_\Psi t) + I^\star_{q1}\sin(\omega_\Psi t) \\ I^\star_{d2}\cos(\omega_\Psi t) + I^\star_{q2}\sin(\omega_\Psi t) \\ -I^\star_{d1}\sin(\omega_\Psi t) + I^\star_{q1}\cos(\omega_\Psi t) \\ -I^\star_{d2}\sin(\omega_\Psi t) + I^\star_{q2}\cos(\omega_\Psi t) \end{bmatrix} \tag{2.23}$$

and the second term is given by the inter-CCV balancing control (Fig. 2.4):

$$\begin{bmatrix} i^\star_{\alpha\alpha2} \\ i^\star_{\alpha\beta_2} \\ i^\star_{\beta\alpha_2} \\ i^\star_{\beta\beta_2} \end{bmatrix} = \begin{bmatrix} I^\star_{d3}\cos(\omega_\chi t) + I^\star_{d5}\cos(\omega_\Psi t) \\ I^\star_{d3}\sin(\omega_\chi t) + I^\star_{d6}\cos(\omega_\Psi t) \\ I^\star_{d4}\cos(\omega_\chi t) + I^\star_{d5}\sin(\omega_\Psi t) \\ I^\star_{d4}\sin(\omega_\chi t) + I^\star_{d6}\sin(\omega_\Psi t) \end{bmatrix} \tag{2.24}$$

with ω_Ψ and ω_χ the frequency of the input- and output-ports, respectively. The amplitudes $I^\star_{d1}$, $I^\star_{d2}$, $I^\star_{d3}$, $I^\star_{d4}$, $I^\star_{d5}$, $I^\star_{d6}$, $I^\star_{q1}$ and $I^\star_{q2}$ are obtained by PI controllers in order to regulate the cluster imbalance in the D-$\alpha\beta$0-framework as shows Fig. 2.4.

2.4.3 Modulation Index Reference

The modulation index references for each arm are generated by considering the system in steady-state. This means that the currents of the converter are the desired ones, i.e., $\boldsymbol{i}_{\alpha\beta0}(k) = \boldsymbol{i}^\star_{\alpha\beta0}(k)$. Thus, by substituting the current references (2.21) and (2.22) into the dynamic model (2.1) in the D-$\alpha\beta$0-framework, it is possible to calculate the desired voltages in the D-$\alpha\beta$0-framework as:

$$\begin{aligned}\begin{bmatrix} v^\star_{\alpha\alpha} & v^\star_{\beta\alpha} & v^\star_{0\alpha} \\ v^\star_{\alpha\beta} & v^\star_{\beta\beta} & v^\star_{0\beta} \\ v^\star_{\alpha0} & v^\star_{\beta0} & v^\star_{00} \end{bmatrix} &= \sqrt{3}\begin{bmatrix} 0 & 0 & 0 \\ 0 & 0 & 0 \\ v^\Psi_\alpha & v^\Psi_\beta & 0 \end{bmatrix} - L\frac{d}{dt}\begin{bmatrix} i^\star_{\alpha\alpha} & i^\star_{\beta\alpha} & i^\star_{0\alpha} \\ i^\star_{\alpha\beta} & i^\star_{\beta\beta} & i^\star_{0\beta} \\ i^\star_{\alpha0} & i^\star_{\beta0} & 0 \end{bmatrix} \\ &\quad -r\begin{bmatrix} i^\star_{\alpha\alpha} & i^\star_{\beta\alpha} & i^\star_{0\alpha} \\ i^\star_{\alpha\beta} & i^\star_{\beta\beta} & i^\star_{0\beta} \\ i^\star_{\alpha0} & i^\star_{\beta0} & 0 \end{bmatrix} - \sqrt{3}\begin{bmatrix} 0 & 0 & v^\chi_\alpha \\ 0 & 0 & v^\chi_\beta \\ 0 & 0 & 0 \end{bmatrix} - \begin{bmatrix} 0 & 0 & 0 \\ 0 & 0 & 0 \\ 0 & 0 & 3v_{n0} \end{bmatrix}\end{aligned} \tag{2.25}$$

Then, by premultiplying by $\left[\boldsymbol{C}^{\alpha\beta0}\right]^{\mathrm{T}}$ and postmultiplying by $\left[\boldsymbol{C}^{\alpha\beta0}\right]$, the voltages obtained in (2.25) are represented in the *abc*-framework:

$$\begin{bmatrix} v^\star_{ua} & v^\star_{va} & v^\star_{wa} \\ v^\star_{ub} & v^\star_{vb} & v^\star_{wb} \\ v^\star_{uc} & v^\star_{vc} & v^\star_{wc} \end{bmatrix} = \left[\boldsymbol{C}^{\alpha\beta0}\right]^T \begin{bmatrix} v^\star_{\alpha\alpha} & v^\star_{\beta\alpha} & v^\star_{0\alpha} \\ v^\star_{\alpha\beta} & v^\star_{\beta\beta} & v^\star_{0\beta} \\ v^\star_{\alpha0} & v^\star_{\beta0} & v^\star_{00} \end{bmatrix} \left[\boldsymbol{C}^{\alpha\beta0}\right] \tag{2.26}$$

Thus, the steady-state duty-cycle required by the proposed controller in (2.12) are obtained by dividing the desired ac cluster voltage $v^\star_\kappa$ by the available cluster capacitor voltage:

$$u^\star_\kappa = N\frac{v^\star_\kappa}{\sum_{j=1}^{N} v_{C,\kappa j}} \tag{2.27}$$

Finally, the future references values are obtained by evaluating them at a discrete-time instant $t(k+1) = t(k) + kT_s$.

2.5 Experimental Results

Experimental results were performed to analyze the proposed long-horizon sequential FCS-MPC strategy performance when governing an M3C connected to a three-phase system and a passive load. The grid-voltage was generated by a regenerative grid-simulator (NHR9410) and the passive load was implemented by a regenerative ac load (NHR9430). Fig. 2.5 presents the prototype, where the proposed predictive control scheme was implemented on an OPAL-RT OP4510 controller. The main setup parameters are shown in Table 2.1. The sFCS-MPC-HH was tuned with σ_{1h}=σ_1=1, σ_{2h}=σ_2=0.2 and λ_h=λ=0.4.

2.5.1 Predictive Control Strategies Comparison

The proposed strategy was evaluated in four versions, from horizon one to four (sFCS-MPC-HH, $H \in \{1,2,3,4\}$), and compared with two Finite-Control-Set strategies, referred in this chapter as sFCS-MPC-27 [20] and FCS-MPC-729 [34].

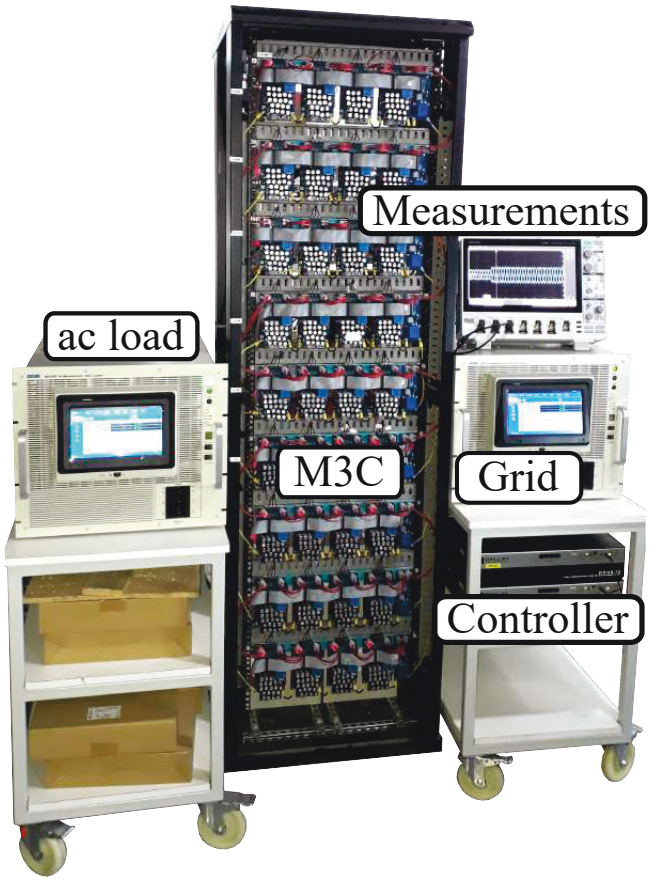

Figure 2.5: 3 kVA experimental prototype.

Table 2.1: System parameters

Variable	Description	Sim/Exp
P	Rated power	3 kW
v_Ψ	Input grid voltage (line-to-line rms)	190 V
f_Ψ	Input grid frequency	60 Hz
r_L	Output resistance	14 Ω
L_L	Output inductance	1 mH
f_χ	Output frequency	5 - 50 Hz
N	SMs per clusters	4
C	SM capacitance	987 μF
$v_{dc}^\star$	dc cap. voltage per SM	120 V
L	Cluster filter inductance	5 mH
r	Cluster filter resistance	0.1 Ω
T_s	Sample time	60 μs

- sFCS-MPC-27 [20]: This predictive control strategy considers the update of one cell each sampling time per arm, which means a total possible combinations of $9 \times 3 = 27$. In addition, the strategy considers a tracking error of arm current and capacitors only.
- FCS-MPC-729 [34]: This predictive control strategy considers the feasible cell output voltage, so for a four-cell M3C converter the total states are $3^{9N} = 3^{36} \approx 1.5 \times 10^{17}$ which cannot be implemented in a simulation environment, even less in a real application. Therefore, the total combinations are reduced by considering the common-mode voltage as a known

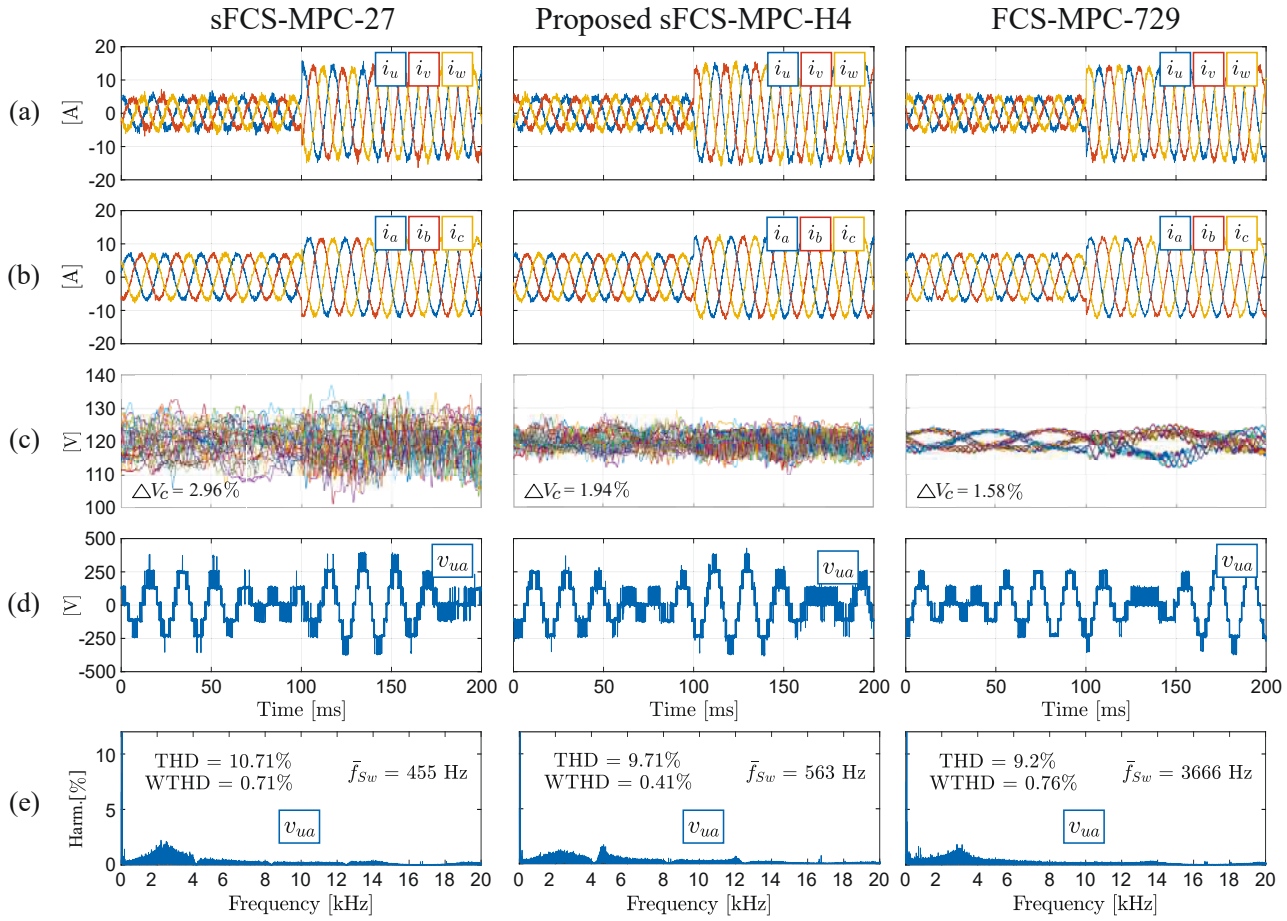

Figure 2.6: Experimental closed-loop comparison, sequential FCS-MPC-H1 strategy proposed in [20] (left), proposed sequential FCS-MPC-H4 strategy (middle) and FCS-MPC-729 strategy (right). (a) input currents, (b) output currents, (c) capacitor voltages, (d) *ua*-cluster output voltage and (e) *ua*-cluster output voltage spectra.

disturbance, decreasing the total combinations to $9 \times 3^N = 9 \times 3^4 = 729$. Additionally, by including constraint (2.16d), the total combinations are bounded by 144 and 729, making its implementation feasible. Nonetheless, the computational burden of this predictive strategy increases exponentially with the number of cells of the converter.

- sFCS-MPC-H4: This proposed predictive control strategy with four-horizon sequential FCS-MPC has a maximum of $9 \times 3^H = 9 \times 3^4 = 729$ possible combinations.

The comparison of the three strategies is shown in Fig. 2.6. Here, it is possible to observe that all the analyzed predictive control strategies achieve a fast dynamic response under a power step. In steady-state, all the strategies achieve the desired system references, obtaining balanced input and output currents, and balanced clusters and cells with a mean capacitor voltage equal to 120 V. However, the proposed sFCS-MPC-H4 provides several advantages when compared to the other two strategies, such as, low average cell switching frequency, a reduced harmonic distortion and a low capacitor ripple.

In order to compare these three strategies, the following five key performance indexes (KPIs) were defined:

(i) KPI_I: average arm current tracking error.

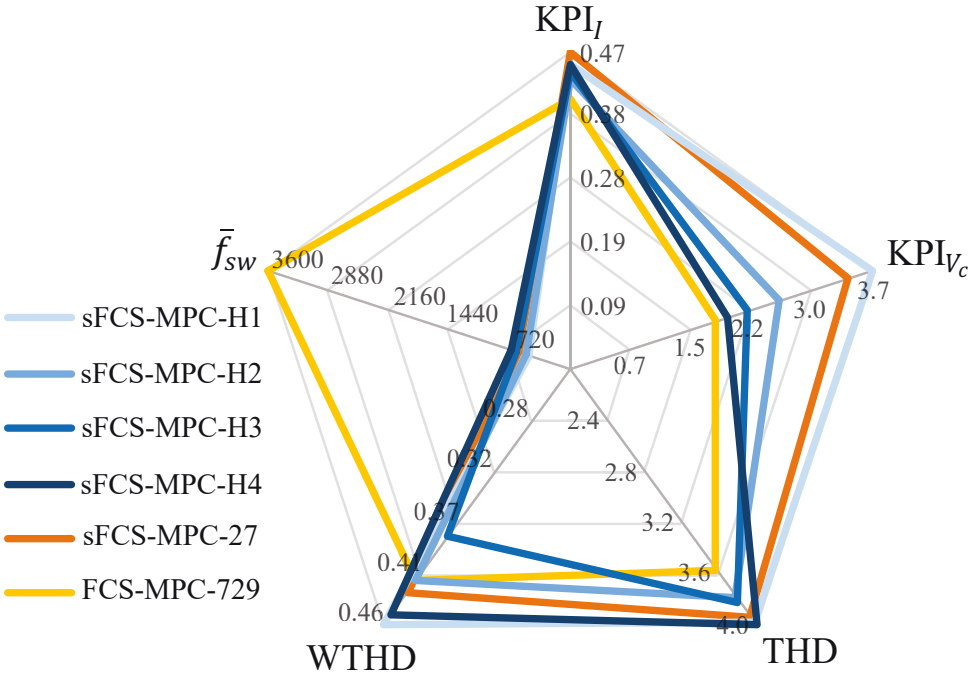

Figure 2.7: Experimental key performance indexes radial graph.

(ii) KPI$_{V_c}$: average capacitor voltage tracking error.

(iii) THD: total harmonic distortion of the phase-a voltage.

(iv) WTHD: weighted THD of the phase-a voltage.

(v) $\bar{f}_{Sw}$: average cell switching frequency.

Fig. 2.7 presents the summary of the five experimental KPIs. Notice that the lower the KPI, the better performance. Therefore, if we weight all the KPIs equally, normalizing each KPI with respect the maximum value, the strategy with the best performance will be the one with the lowest sum. The proposed sFCS-MPC-H3 has the lowest value of 3.48, achieving the best performance, followed by the proposal with horizon 2 (with 3.62) and 4 (with 3.66). In contrast, the FCS-MPC-729 has the worst performance (with 4.14).

The proposed sFCS-MPC-H3 improves the KPI$_I$ and KPI$_{V_c}$ performance indexes with 0.44 A and 2.19 V, highly reducing the capacitor voltage ripple, in comparison with [20] whose KPIs are 0.47 A and 3.42 V, respectively. Additionally, the voltage harmonic distortion is reduced, decreasing the THD from 3.95% to 3.82% and the WTHD from 0.43% to 0.38%. However, the average switching frequency rises from 589 Hz to 618 Hz and the total number of input combination to be evaluated in the cost function increases from 27 to 243.

The proposed sFCS-MPC-H4, in comparison with the FCS-MPC-729, highly reduces the average cell switching frequency by 80.66%, from 3563 Hz to 689 Hz, significantly reducing the switching power losses. Nevertheless, the cluster current and capacitor voltage tracking error are slightly higher, increasing these indexes by 12.5% and 8.33%, respectively. In addition, the distortion rises, increasing the voltage THD and WTHD by 12.01% and 7.14%, respectively.

An increase in the prediction horizon has a direct impact in the capacitor voltage tracking error, improving it by up to 47.3%, from 3.7 V to 1.95 V. However, it does not highly impact the KPI$_I$. In terms of distortion, the best performance occurs for the sFCS-MPC-H3, where

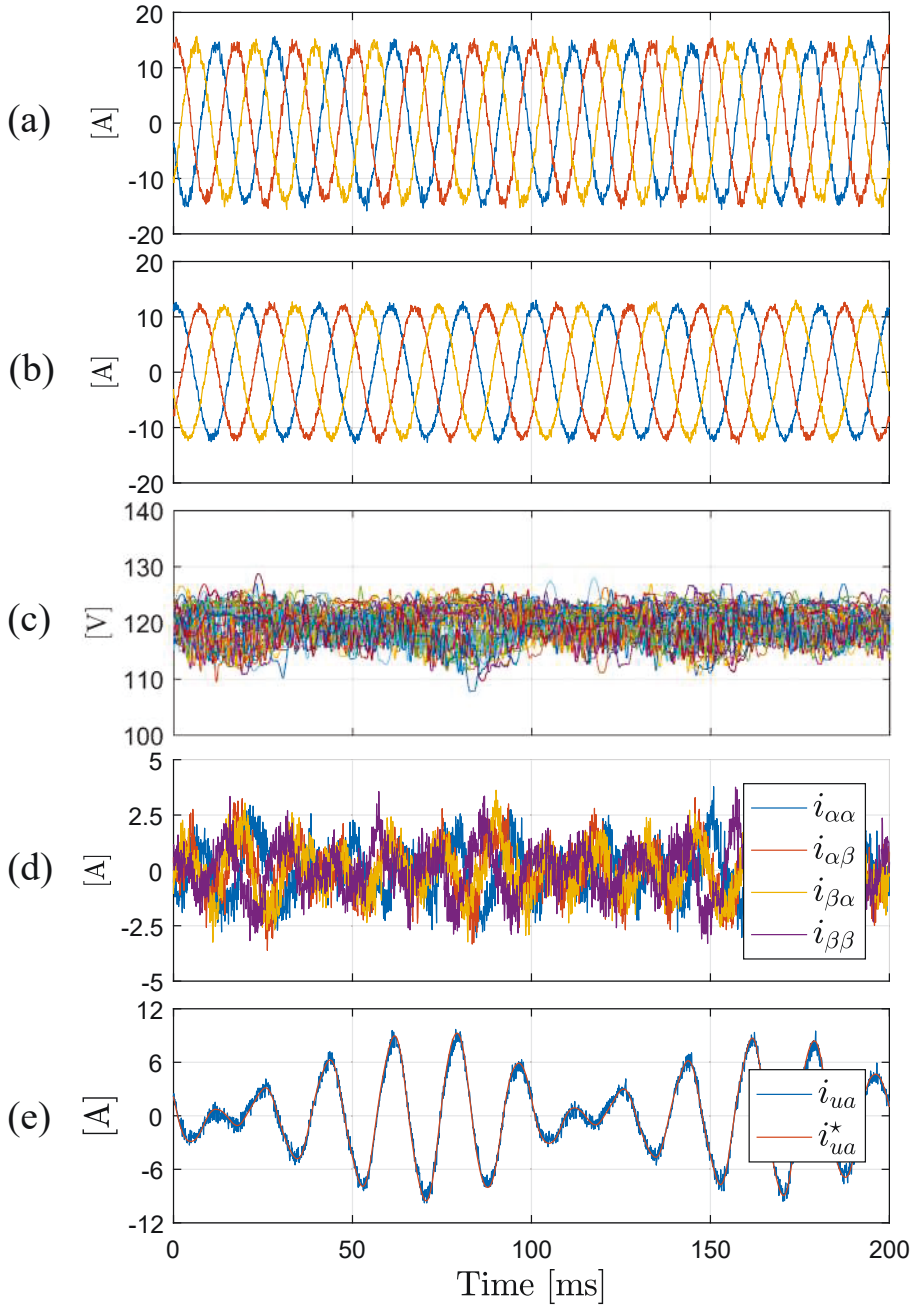

Figure 2.8: Experimental steady-state performance. (a) input currents, (b) output currents, (c) capacitor voltages, (d) circulating currents and (e) *ua*-cluster current.

the voltage THD and WTHD decrease by 4.02% and 17.39%, regarding the sFCS-MPC-H1. Finally, the average cell switching frequency augments with as the prediction horizon, going from 476 Hz to 517 Hz, 618 Hz and 689 Hz. Therefore, by increasing the horizon there is a trade-off between the tracking error and the average cell switching frequency performance.

Experimental mismatches up to 50% has been considered for three parameters: the filter resistance (r), the filter inductance (L) and the sub-module capacitance (C). Parameter mismatches are generated in the model while maintaining the experimental setting, and its effects in the cluster current and capacitor voltage deviations (KPI_I and KPI_{V_c}) were evaluated. The changes in the KPIs (the absolute value of the KPI with the mismatch minus the KPI with no mismatch) have been plotted in Fig. 2.9. The mismatch in the filter resistor generates marginal

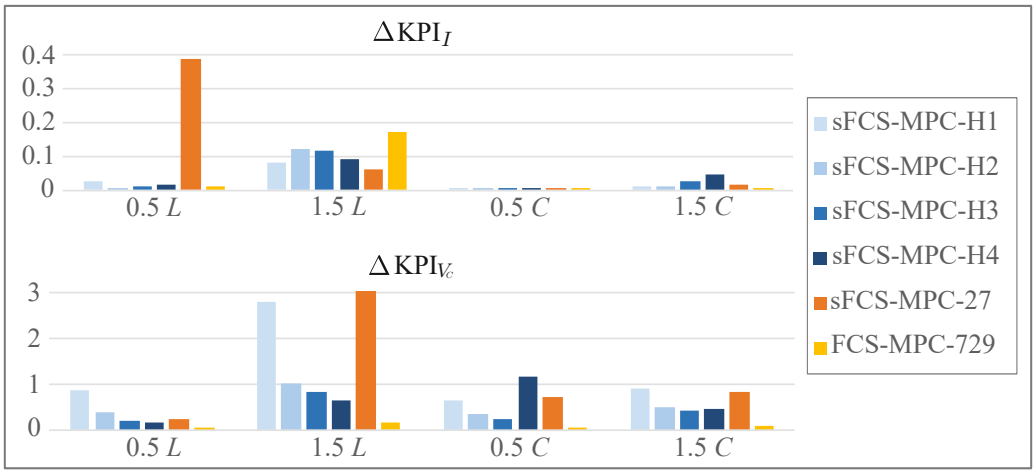

Figure 2.9: Experimental mismatches between control parameters and real hardware values.

deviations that can be neglected, which is due to its small value. The mismatch in the sub-modules capacitance does not generate a considerable deviation in the cluster current, but it does in the voltage of the capacitors for all the methods, where horizon 3 is the most tolerant of all. Finally, the inductor mismatch generates the largest deviations of cluster current and capacitor voltage, especially when the inductor increases in the model, being the [20] method the most affected. However, all the methods present tolerance to these mismatches.

2.5.2 Closed-Loop Steady-State Performance

The results of the closed-loop steady-state performance are presented in the Fig. 2.8. As can be seen, the proposed sFCS-MPC-H4 is able to properly govern the M3C, achieving a symmetric waveform for the input, output and circulating currents as shown Figs. 2.8(a), 2.8(b) and 2.8(d), respectively. Additionally, in Fig. 2.8(c), the predictive strategy successfully regulates the capacitor voltages at 120 V. Moreover, the circulating currents are properly tracked in order to balance the converter clusters and reduce the capacitor voltage ripple. It is important to mention that this control strategy is able to track any current waveform, including several frequencies in comparison with control strategies that uses proportional controllers (cf. [16]).

The spectrum of the proposal is centered at low frequency and its spread because the proposed does not use a modulator. In terms of the input currents, the phase-u current presents a THD of 3.08% and a WTHD of 0.72%. However, in terms of the output currents, the phase-a current has a lower THD and WTHD, which are 1.80% and 0.30%, respectively. These different behaviors between input and output currents, in terms of distortion, is mainly given by the PI controller which regulates the average energy of the converter because it directly affects the reference generation of the input currents. Moreover, the cluster current is properly controlled even when its reference presents different frequency components as shown in Fig. 2.8(e).

The lambda value is used to adjust the compromise between the state tracking error and the control effort, allowing the dynamic response of the closed-loop system to be modified. Different values of lambda has been tested to appreciate its effects in the states. A low value of lambda allow the proposal to drastically change the state of the sub-module in order to reduce the state tracking error only. In contrast, a high value of lambda increases the importance of the duty cycle reference, so the M3C operates in open-loop. As presented in the Fig. 2.10, a very high lambda value leads to an open-loop operation, affecting the phase in the current port and

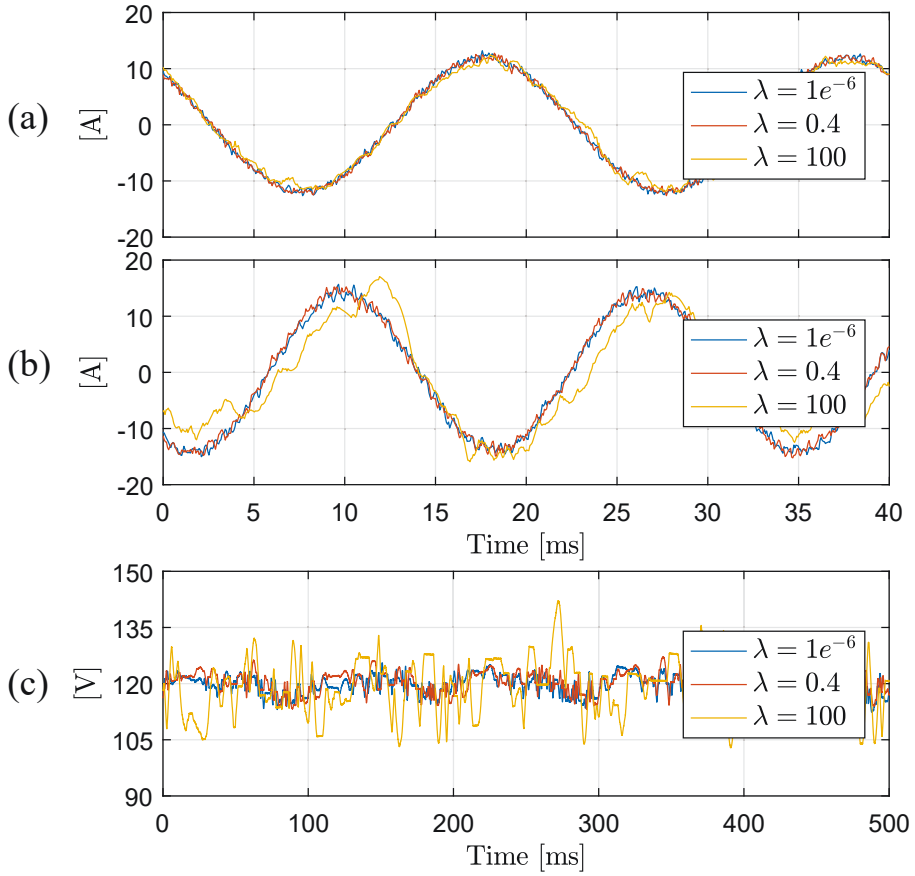

Figure 2.10: Experimental results of the proposal with horizon 4 under different values of λ. (a) output-port; (b) input-port; and (c) capacitor voltages.

with it, the state tracking error. Therefore, a middle value must be chosen in order to obtain a balance between good state tracking error and a smooth voltage waveform.

2.5.3 Closed-Loop Dynamic Response

The results of the closed-loop dynamic response performance under a power-step are presented in Fig. 2.6 and Fig. 2.11, and under an intra-cluster imbalance in the Fig. 2.12.

Power Step Change

The dynamic response, in terms of power step change, is almost instantaneous and does not present overshoot. The peak value of both ports increase due to the power step and the speed of the change is fast, as shown in Figs. 2.6a and 2.6b. In Fig. 2.6c, the ripple of the capacitor voltages augment due to the power step; nevertheless, the mean value of the capacitor voltages remains constant. Additionally, the input-port always presents a unitary power factor as is shown in Fig 2.11, where the grid voltage and its current are in phase obtaining a null reactive power, meanwhile the active power is changed from 1 to 3 kW.

Intra-Cluster Imbalances

In this test, an imbalance among *ua*-cluster cells is imposed in order to present the dynamic response of the sFCS-MPC-H4 to balance them. The dynamic response of currents and ca-

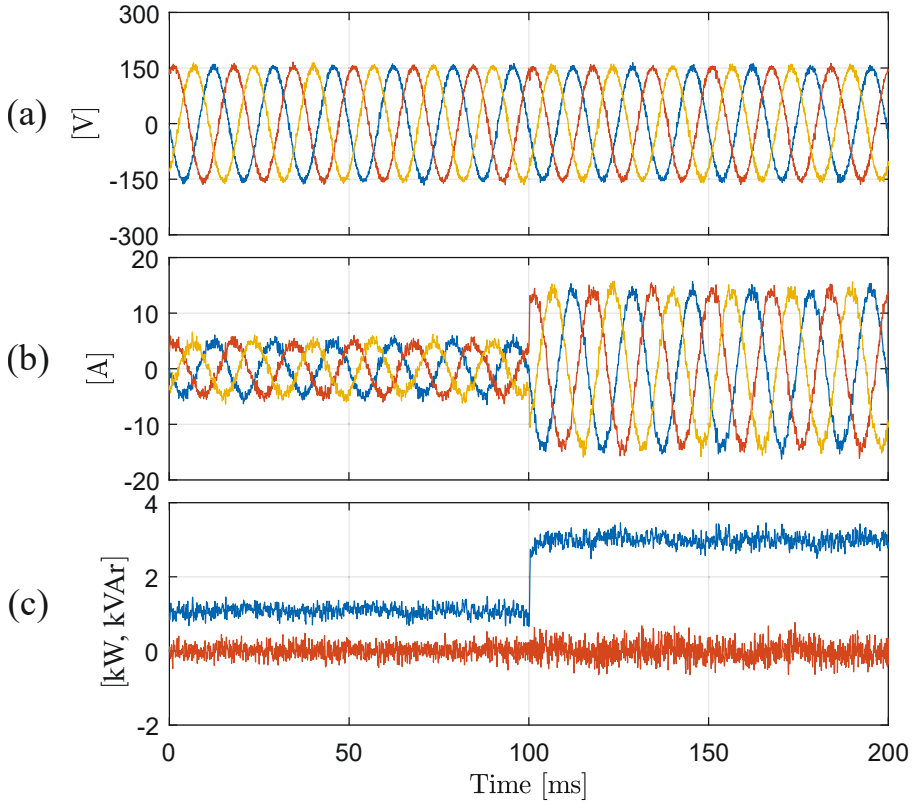

Figure 2.11: Experimental dynamic response of input-port power. (a) input-port voltage; (b) output-port current; and (c) input-port active and reactive power.

pacitor voltages are presented in Fig. 2.12. Until second 0.2, the capacitor voltages of the ua-cluster are intentionally governed to achieve an unbalanced condition of 100, 110, 130 and 140 V, respectively. Then, in the second 0.2, a balanced capacitor voltage condition is imposed to 120 V. This voltage balancing is achieved in less than 25 ms. Notice that the circulating current references are not affected since they are designed to balance the converter among cluster and not among cells of a specific cluster.

2.5.4 Different Output Frequency Performance

The results of the sFCS-MPC-H4 governing the M3C with different frequencies are presented in the Fig. 2.13. In this test, the fundamental frequency at the uvw-port is fixed at 60 Hz, while the fundamental frequency at the output-port has been changed. In the first part, the fundamental frequency at the output-port is 5 Hz; in the second part. 30 Hz; and in the last part, 50 Hz. The sFCS-MPC-H4 is able to track the current references independent of its fundamental frequency and the resulting common-mode voltage is low because the duty-cycle references consider a null common-mode voltage. The capacitor voltage ripple is ± 15 V when the fundamental frequency f_χ is 5 Hz, and is reduced to ± 8 V when the fundamental frequency f_χ is higher. The cluster current and output voltage waveform depend on the frequencies of both ports, presenting both frequencies, specifically, the subtraction of u- and a-phase. Notice when f_χ is 30 Hz, the mean value is not zero because f_ψ is twice the frequency f_χ, so the peak values are in phase.

The closed-loop dynamic response of the proposed controller under step changes on the output frequency is presented in Fig. 2.14. As shown in Fig. 2.14b, the output current response

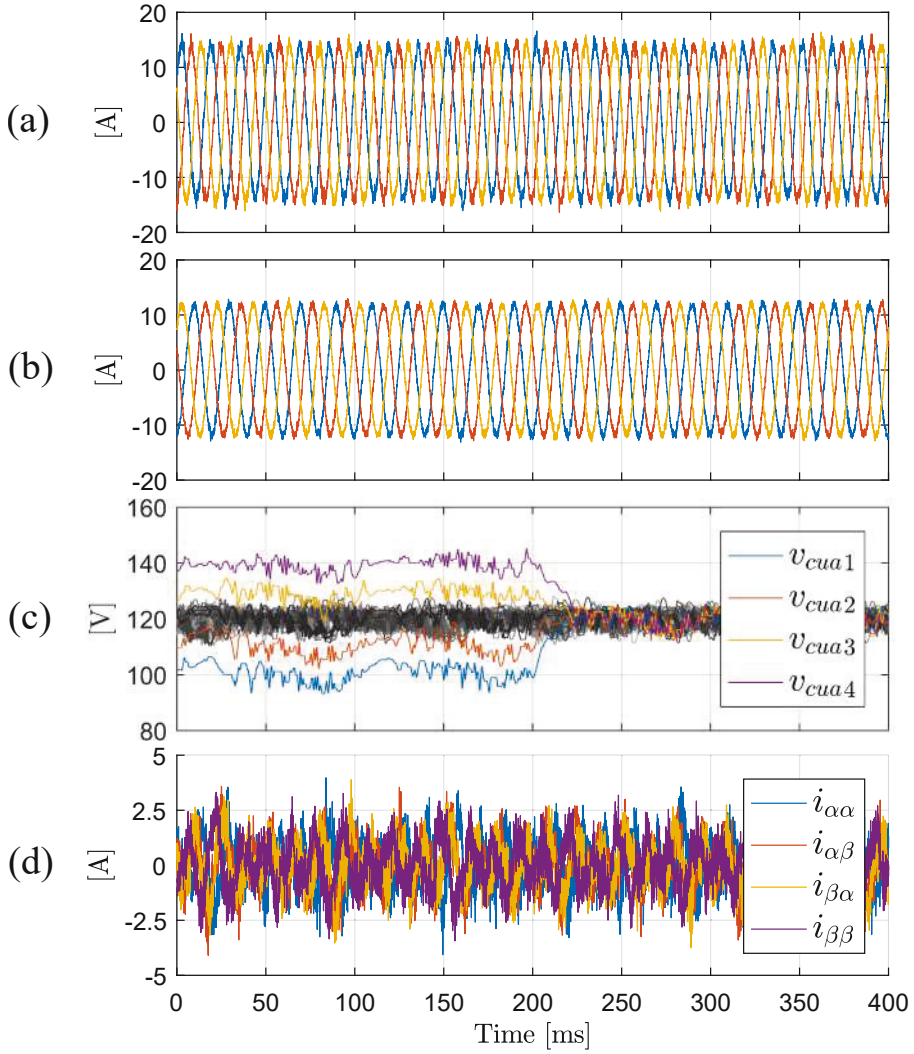

Figure 2.12: Experimental intra-cluster imbalance. (a) input currents, (b) output currents, (c) capacitor voltages, (d) circulating currents.

under a frequency change is instantaneous, similar to the one obtained under step changes on the active power presented in Fig. 2.6, Moreover, the capacitor voltages are well regulated even during sudden frequency changes, as depicted in Fig. 2.14a, proving that the proposed controller enables the converter to operate with variable frequency.

2.5.5 Scalability Analysis of the proposed sFCS-MPC-HH

The computational burden of the different MPC methods has been calculated in terms of floating point operations per second (FLOPS). On the one hand, by analyzing equations (2.14), (2.15), (2.16a), and neglecting multiplications with zeros, the proposed control algorithm presents a total number of FLOPS of $9H \cdot 3^H (8N + 13)/T_s$. On the other hand, the control methods presented in [20] and [34] have $27(7N + 10)/T_s$ and $9 \cdot 3^N (8N + 13)/T_s$ FLOPS, respectively. The number of FLOPS required per control strategy as function of the number of sub-modules are presented in Fig. 2.15, where all the control strategies have a quadratic increment, unlike [34] which increases exponentially.

The converter prototype is governed by an OPAL-RT OP4510. This control platform is equipped with an Intel Xeon Processor E3-1565L v5, capable of executing 89.6 GFLOPS with

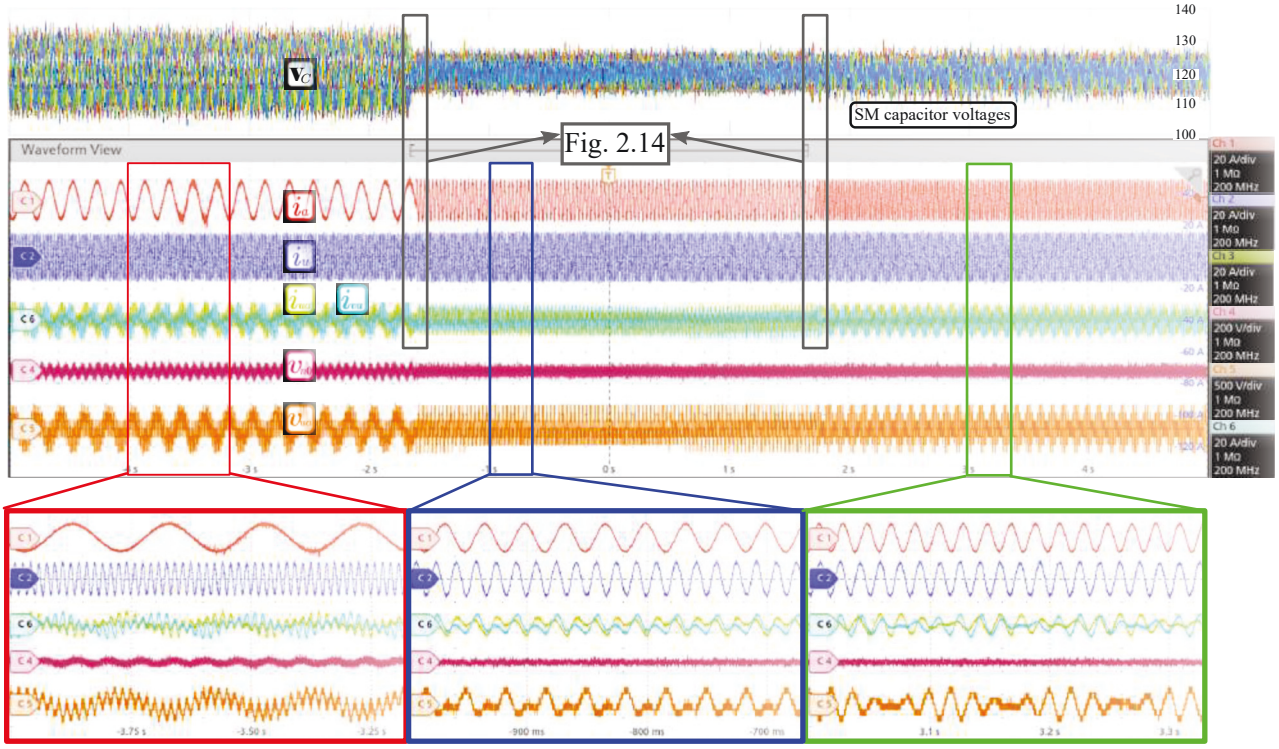

Figure 2.13: Experimental frequencies performance, *abc*-port frequency at 5, 30 and 50 Hz. (Top graph) capacitor voltages, (Ch 1) output current a, (Ch 2) input current u, (Ch 3) ua-cluster current, (Ch 4) common mode voltage, (Ch 5) ua-cluster output voltage, and (Ch 6) va-cluster current.

its four cores. Consequently, as shown in Fig. 2.15, the maximum number of SMs the proposed controller can handle are 24887, 4146, 920 and 228 for horizons 1,2,3 and 4, respectively. In contrast, [20] and [34] can handle up to 28443 and 8 SMs, respectively.

Furthermore, for the converter prototype with $N = 4$ SMs, the experimental execution times of the proposed control algorithm are 0.43, 1.13, 3.67 and 10.72 μs, for horizons 1, 2, 3 and 4, respectively. Instead, the execution times of the control method presented in [20] and [34] are 0.4 and 1.57 μs, respectively. Therefore, the control strategies can be sorted from highest computational burden to lowest as [20], sFCS-MPC-H1, sFCS-MPC-H2, [34], sFCS-MPC-H3, and sFCS-MPC-H4. This behavior is the same obtained with the FLOPS analysis previously mentioned, for $N = 4$, as shown in Fig. 2.15.

2.6 Conclusion

This chapter proposed a long-horizon sFCS-MPC strategy to govern M3Cs. The proposed controller can effectively perform the LCB control task and regulate the cluster current in a single multivariable control stage. Additionally, by considering the common-mode voltage as a known disturbance, the control strategy is independent of the other clusters and the maximum number of total possible combinations are 3^H per cluster. Therefore, in order to govern the M3C nine sFCS-MPC-HH are implemented.

The experimental results showed that the proposed sequential FCS-MPC-H4 provides a fast dynamic response and steady-state tracking for the input, the output, and the circulating

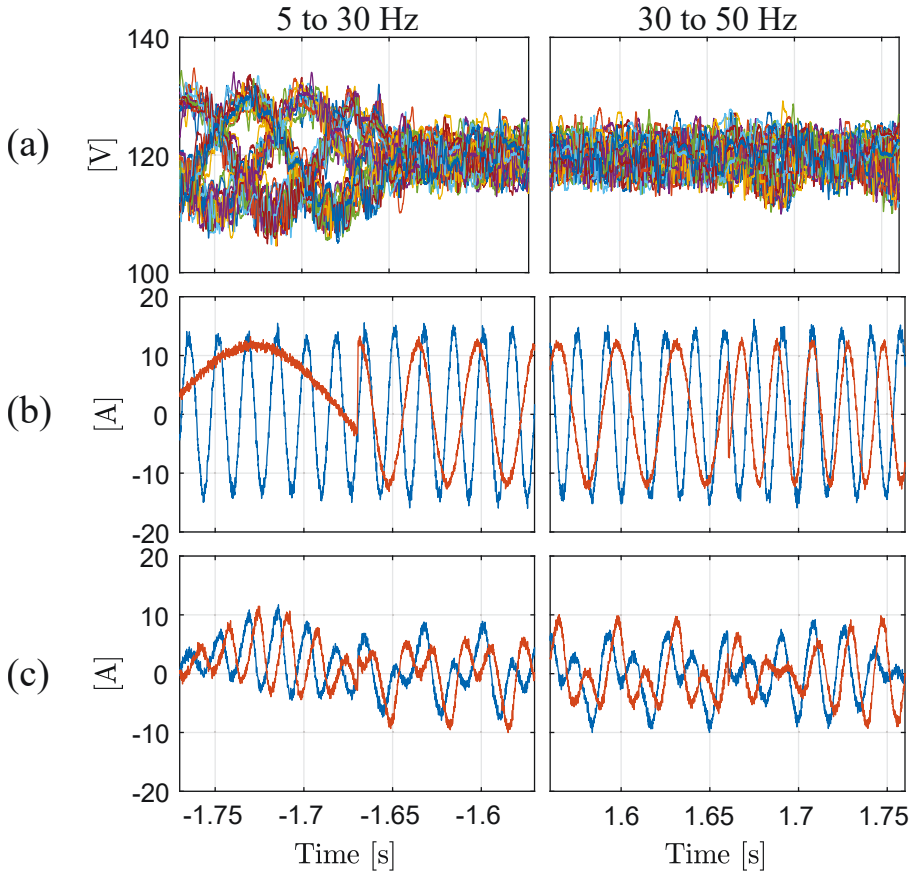

Figure 2.14: Experimental dynamic response under frequency changes. (a) capacitor voltages; (b) input and output current; and (c) $ua-$ and $va-$cluster current.

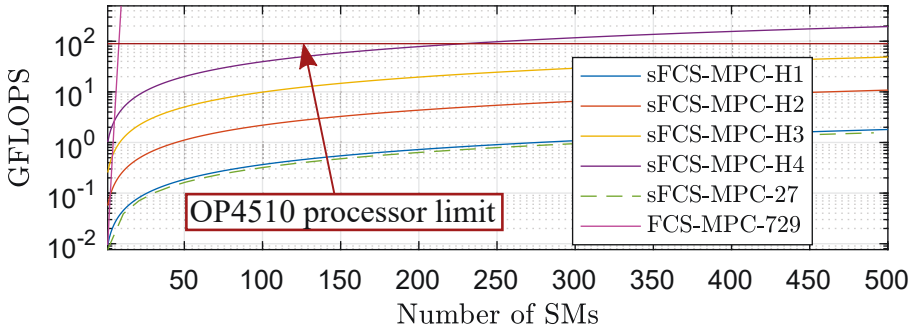

Figure 2.15: FLOPS per control strategy.

currents, even if they present multiple frequency components. Moreover, the proposed controller significantly improved the average cell switching frequency, the computational burden and its scalability in comparison with the FCS-MPC-729 [34] and reduced the capacitor voltage ripple in comparison with the standard sFCS-MPC-27 [20].

Chapter 3

COMPUTATIONALLY EFFICIENT MPC FOR MODULAR MULTILEVEL MATRIX CONVERTERS OPERATING WITH FIXED SWITCHING FREQUENCY

3.1 Introduction

Modular multilevel cascaded converters (MMCCs) are considered the next generation technology for medium and high power applications given by its high quality voltage waveform, modularity and capability to directly connect at medium and high voltages [11], [12], [35]–[37]. The cascaded H-bridge (CHB), the modular multilevel converter (M2C), the modular multilevel matrix converter (M3C) and Hexverter are some examples of MMCCs.

In terms of ac to ac power conversion, the back-to-back M2C (B2B-MMC) and the M3C are the preferred power converters to use for applications such as, wind energy conversion systems (WECS) and medium/high voltage motor drives for marine propulsion, mills, pumps, conveyors, power system interconnections (50-60 Hz) and low frequency ac (LFAC) transmission systems [10].

The M3C, also known as triple-star bridge cell (TSBC) converter, has been compared with B2B-M2C for ac-ac applications [10]. As a result, in comparison with the B2B-M2C, the M3C directly performed ac-to-ac conversion without a high voltage dc-link [11], [12] and needs less sub-modules [13]. Moreover, for low frequencies and high power applications such as LFAC transmission systems, WECS and low speed motor drives, the M3C has shown a better performance [10]. Nevertheless, the implementation of the M3C has been hampered due to its control complexity, dealing with a highly coupled system, several floating capacitors, a big number of control signals and critical operating frequencies [16], [17].

A standard approach to solve the previously mentioned challenges is considering a several proportional-integral (PI) or proportional-resonant (PR) controllers [11]–[13], [16], [18]. However, the robustness of the closed-loop response is reduced when using multiple single-input-single output (SISO) controllers in highly coupled systems with more variable than degrees of

freedom in comparison with multiple-inputs-multiple-outputs (MIMO) controllers. Additionally, the tuning of linear controllers works for a local operating point, outside this region the multiple SISO strategy performance worsens.

The finite-control-set model-predictive-control (FCS-MPC) has been proposed in the literature to solve the aforementioned SISO control limitations [20], [21], [43]. However, the FCS-MPC introduces other disadvantages such as a spread frequency spectrum, mainly concentrated at low frequencies, due to the lack of a modulation stage, and requires a high computational effort which increases exponentially with the number of sub-modules, limiting the implementation of FCS-MPC to M3Cs with a reduced number of sub-modules. In [29], a continuous-control-set MPC (CCS-MPC) has been proposed in the literature, but that strategy is designed to only control the circulating currents. In [44]–[46], the MPC strategies have been designed to balance the energy among clusters generating the optimal circulating currents. Nonetheless, these strategies do not govern the currents or balance the energy among sub-modules of the M3C. In [38], an MPC strategy is proposed to balance the energy among sub-modules in a cluster, achieving a faster dynamic response in comparison with a standard algorithm for PS-PWM. Nevertheless, this approach does not perform the current control of the M3C. To account for these drawbacks, a sequential phase-shifted model-predictive-control (PS-MPC) has been proposed for multilevel converters to improve the frequency spectrum and reduce the computational burden of the MPC. The PS-MPC exploits the sequential working principle of a phase-shifted pulse-width-modulation (PS-PWM), which allows the MPC to only optimize the duty-cycle of the switch that is going to be updated next. The PS-MPC was initially implemented in a single-phase flying capacitor converter [22], and then proposed to govern a CHB converter with independent power sub-modules [23], and an M2C in order to include multiple control objectives (ac current, circulating currents and capacitor voltages balance) [24]. Nevertheless, in [22]–[24], the optimal unconstrained solution of the control inputs are saturated and might not be the optimal during transients.

This chapter proposes a remodeling of the M3C for the design and implementation of a tailor-made sequential PS-MPC, which considers the coupling of the states, the control input constraints and simplifies the control structure in comparison with multiple-SISO-based control strategies. Thus, the proposed control strategy is formulated to control the cluster currents directly in the double $\alpha\beta 0$ framework and the SM capacitor voltages by only computing nine control signals at each sampling instant independently of the number of sub-modules of the converter. This increases the scalability and applicability in comparison with a standard FCS-MPC. In addition, the proposed strategy directly considers the dynamic of the three-phase ac-ports, allowing to include different types of loads in the optimal control problem.

The contribution and novelty of this proposal is the reformulation of the M3C modeling to apply a computationally efficient MPC strategy that fully exploits the working principle of the PS-PWM technique, including the dynamic particularities of this MMCC topology. Furthermore, in contrast to previous PS-MPC strategies, this work achieves the optimal solution not only in steady-state but also during transients.

Therefore, the M3C model was formulated to achieve a decoupled set of current equations while maintaining the control input in the original framework when they need to be constrained for a safe converter operation. Additionally, the M3C has a very particular dynamic at different operating frequencies, which was considered by the proposed model. Therefore, the contribution of this work is not the simple application of the sequential PS-MPC to an M3C but rather the remodeling of the converter and algorithm to achieve the following advantages: i) a unified

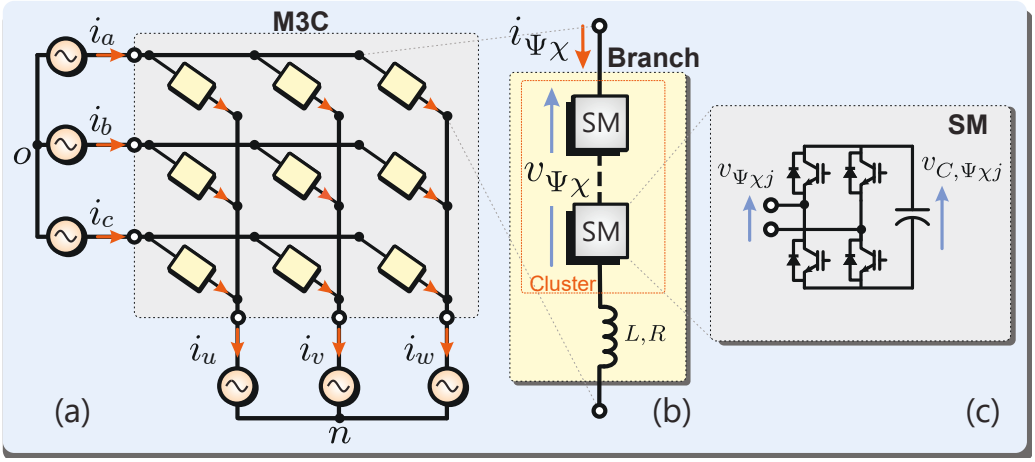

Figure 3.1: The M3C topology: (a) circuit diagram; (b) N-cell cluster; and (c) full-bridge-based submodule.

control structure to control the SM capacitor voltages and the arm currents considering the control input limits as bound constraints; ii) reduced computational burden by computing only one control signal per cluster at each sampling time; iii) scalability to operate with a large number of sub-modules; and iv) fast closed-loop transient response with low distortion and capability to track multiple frequency wave-forms in the arm currents.

Experimental results are provided to verify the proposal performance and effectiveness, showing a fast dynamic response, a low harmonic distortion, and a suitable computational burden operating with a single centralized controller.

3.2 The Modular Multilevel Matrix Converter Model

The M3C topology is composed of nine stacks or clusters to interconnect two three-phase ac-ports (Fig. 3.1(a)). Each cluster is formed by connecting several H-bridges cells or sub-modules (SMs) in cascade manner along with a series cluster inductor (Fig. 3.1(b)). Additionally, as shown in Fig. 3.1(c), each SM has a floating capacitor in its dc-link.

The M3C has four control targets: the currents of both ac-ports; the circulating currents; and the capacitor voltages of each sub-module. The balancing of the capacitor voltages can be indirectly attained by implementing three energy control strategies [25], [29], [46]: *i) Total Energy Balancing (TEB) Control*: Regulate the energy stored in all capacitors to the desired level by transferring power to or from the AC ports. *ii) Inter-Cluster Balancing (ICB) Control*: Distributes the power of the M3C among all its clusters, determining the imposition of internal command signals for the common-mode voltage and the circulating currents, without affecting the AC ports. However, the ICB should generate minimal circulating currents to increase the efficiency and power density of the converter. *iii) Local-Cluster Balancing (LCB) Control*: Locally regulates the capacitor voltage of each SM in each cluster. It is usually implemented at the modulation stage. In addition, when the converter operates at a shallow frequency in any external port, but most acutely when these frequencies get closer or equal, it is necessary to mitigate large oscillations in the SM capacitor voltages by injecting a proper CMV and additional circulating current components. The latter control task is referred to as Low-Frequency Oscillation (LFO) mitigation.

3.2.1 Modelling of the M3C

Considering the circuit diagram of the M3C shown in Fig. 3.1(a), the continuous-time model of each branch current, $i_{\Psi\chi}$, can be expressed via:

$$\frac{\mathrm{d}}{\mathrm{d}t} i_{\Psi\chi} = \frac{1}{L}\left(v_{\Psi} - r i_{\Psi\chi} - v_{\Psi\chi} - v_{\chi} - v_{no}\right) \tag{3.1}$$

where $\Psi \in \{a, b, c\}$ and $\chi \in \{u, v, w\}$. Here, L and r are the inductance and the resistance of the cluster filter, respectively. Additionally, the variables v_{Ψ} and v_{χ} stand for the input- and the output-port voltage in each phase, respectively; and v_{no} denotes voltage between the neutral points. The cluster voltage, $v_{\Psi\chi}$, is formed by the sum of all its individual sub-module voltages, i.e.:

$$v_{\Psi\chi} = \sum_{j=1}^{N} v_{\Psi\chi j} \tag{3.2}$$

In (3.2), $v_{\Psi\chi j}$ is the jth sub-module output voltage and its average value over a switching period is given by:

$$v_{\Psi\chi j} = v_{C,\Psi\chi j}\, \delta_{\Psi\chi j} \tag{3.3}$$

where $\delta_{\Psi\chi j}(t) \in \mathbb{D} \triangleq [-1, 1]$ represents the duty cycle of the j-th sub-module in the $\Psi\chi$-cluster, which is the control input of the system. Moreover, the dynamic model of each capacitor voltage, $v_{C,\Psi\chi j}$, is given by:

$$\frac{\mathrm{d}}{\mathrm{d}t} v_{C,\Psi\chi j} = \frac{1}{C} i_{\Psi\chi}\, \delta_{\Psi\chi j} \tag{3.4}$$

Then, by applying the above equations to all nine arms, the following dynamic model for the cluster currents is obtained:

$$\begin{aligned} L\frac{\mathrm{d}}{\mathrm{d}t}\begin{bmatrix} i_{au} & i_{bu} & i_{cu} \\ i_{av} & i_{bv} & i_{cv} \\ i_{aw} & i_{bw} & i_{cw} \end{bmatrix} &= \begin{bmatrix} v_a & v_b & v_c \\ v_a & v_b & v_c \\ v_a & v_b & v_c \end{bmatrix} - r\begin{bmatrix} i_{au} & i_{bu} & i_{cu} \\ i_{av} & i_{bv} & i_{cv} \\ i_{aw} & i_{bw} & i_{cw} \end{bmatrix} \\ &- \begin{bmatrix} v_{au} & v_{bu} & v_{cu} \\ v_{av} & v_{bv} & v_{cv} \\ v_{aw} & v_{bw} & v_{cw} \end{bmatrix} - \begin{bmatrix} v_u & v_u & v_u \\ v_v & v_v & v_v \\ v_w & v_w & v_w \end{bmatrix} - v_{no}\begin{bmatrix} 1 & 1 & 1 \\ 1 & 1 & 1 \\ 1 & 1 & 1 \end{bmatrix}. \end{aligned} \tag{3.5}$$

The cluster currents presented in (3.5) have input, output and circulating currents mixed. To facilitate the control design, the so-called $\alpha\beta 0$ transformation is applied to (3.5) in order to obtain decoupled currents. The $\alpha\beta 0$ transformation matrix is given by:

$$\mathbf{C}^{\alpha\beta 0} = \sqrt{\frac{2}{3}}\begin{bmatrix} 1 & -\frac{1}{2} & -\frac{1}{2} \\ 0 & \frac{\sqrt{3}}{2} & -\frac{\sqrt{3}}{2} \\ \frac{1}{\sqrt{2}} & \frac{1}{\sqrt{2}} & \frac{1}{\sqrt{2}} \end{bmatrix} = \begin{bmatrix} c_1^{\alpha} & c_2^{\alpha} & c_3^{\alpha} \\ c_1^{\beta} & c_2^{\beta} & c_3^{\beta} \\ c_1^{0} & c_2^{0} & c_3^{0} \end{bmatrix} = \begin{bmatrix} \boldsymbol{C}^{\alpha} \\ \boldsymbol{C}^{\beta} \\ \boldsymbol{C}^{0} \end{bmatrix} \tag{3.6}$$

The M3C model can be represented in the double-$\alpha\beta 0$-framework (D-$\alpha\beta 0$) premultiplying by

Table 3.1: System variables

Variable	Definition	Description
$\boldsymbol{i}^{\alpha\beta0}(k)$	$\left[i_{\alpha\alpha}\, i_{\alpha\beta}\, i_{\alpha0}\, i_{\beta\alpha}\, i_{\beta\beta}\, i_{\beta0}\, i_{0\alpha}\, i_{0\beta}\right]^{\mathrm{T}}$	D-$\alpha\beta0$ cluster current vector
$\boldsymbol{v}_{C,j}(k)$	$\left[\boldsymbol{v}_{C,aj}^{\mathrm{T}}(k) \quad \boldsymbol{v}_{C,bj}^{\mathrm{T}}(k) \quad \boldsymbol{v}_{C,cj}^{\mathrm{T}}(k)\right]^{\mathrm{T}}$	Capacitor voltage j vector
$\boldsymbol{v}_{C,\Psi j}(k)$	$\left[v_{C,\Psi uj}(k)\; v_{C,\Psi vj}(k)\; v_{C,\Psi wj}(k)\right]^{\mathrm{T}}$	Capacitor voltage Ψj vector
$\boldsymbol{\delta}_j(k)$	$\left[\boldsymbol{\delta}_{aj}^{\mathrm{T}}(k) \quad \boldsymbol{\delta}_{bj}^{\mathrm{T}}(k) \quad \boldsymbol{\delta}_{cj}^{\mathrm{T}}(k)\right]^{\mathrm{T}}$	Control signal j vector
$\boldsymbol{\delta}_{\Psi j}(k)$	$\left[\delta_{\Psi uj}(k)\; \delta_{\Psi vj}(k)\; \delta_{\Psi wj}(k)\right]^{\mathrm{T}}$	Control signal Ψj vector

$\left[\mathbf{C}^{\alpha\beta0}\right]$ and postmultiplying by $\left[\mathbf{C}^{\alpha\beta0}\right]^{\mathrm{T}}$, resulting in the following decoupled model:

$$\begin{aligned} L\frac{\mathrm{d}}{\mathrm{d}t}\begin{bmatrix} i_{\alpha\alpha} & i_{\beta\alpha} & i_{0\alpha} \\ i_{\alpha\beta} & i_{\beta\beta} & i_{0\beta} \\ i_{\alpha0} & i_{\beta0} & 0 \end{bmatrix} &= \sqrt{3}\begin{bmatrix} 0 & 0 & 0 \\ 0 & 0 & 0 \\ v_{\Psi}^{\alpha} & v_{\Psi}^{\beta} & 0 \end{bmatrix} - r\begin{bmatrix} i_{\alpha\alpha} & i_{\beta\alpha} & i_{0\alpha} \\ i_{\alpha\beta} & i_{\beta\beta} & i_{0\beta} \\ i_{\alpha0} & i_{\beta0} & 0 \end{bmatrix} \\ &- \begin{bmatrix} v_{\alpha\alpha} & v_{\beta\alpha} & v_{0\alpha} \\ v_{\alpha\beta} & v_{\beta\beta} & v_{0\beta} \\ v_{\alpha0} & v_{\beta0} & v_{00} \end{bmatrix} - \sqrt{3}\begin{bmatrix} 0 & 0 & v_{\chi}^{\alpha} \\ 0 & 0 & v_{\chi}^{\beta} \\ 0 & 0 & 0 \end{bmatrix} - \begin{bmatrix} 0 & 0 & 0 \\ 0 & 0 & 0 \\ 0 & 0 & 3v_{no} \end{bmatrix} \end{aligned} \tag{3.7}$$

The double-$\alpha\beta0$ representation allows to directly govern input, output and circulating currents of the converter because they are fully decoupled [11], [12], [16], [25]. Thus, the dynamic of the both three-phase systems can be directly considered in the model, e.g., a three-phase inductive load:

$$\begin{bmatrix} v_{\chi}^{\alpha} \\ v_{\chi}^{\beta} \end{bmatrix} = r_L \begin{bmatrix} i_{\chi}^{\alpha} \\ i_{\chi}^{\beta} \end{bmatrix} + L_L \frac{\mathrm{d}}{\mathrm{d}t}\begin{bmatrix} i_{\chi}^{\alpha} \\ i_{\chi}^{\beta} \end{bmatrix} \tag{3.8}$$

where L_L and r_L are the inductance and the resistance of the load, respectively. Moreover, the relation between the $\alpha\beta0$ $uvw-$current and the D-$\alpha\beta0$ cluster current is given by

$$\begin{bmatrix} i_{\chi}^{\alpha} \\ i_{\chi}^{\beta} \end{bmatrix} = \sqrt{3}\begin{bmatrix} i_{0\alpha} \\ i_{0\beta} \end{bmatrix} \tag{3.9}$$

Thus, the dynamic of the $abc-$port can be directly considered as function of the D-$\alpha\beta0$ cluster currents:

$$\begin{bmatrix} v_{\chi}^{\alpha} \\ v_{\chi}^{\beta} \end{bmatrix} = \sqrt{3}r_L \begin{bmatrix} i_{0\alpha} \\ i_{0\beta} \end{bmatrix} + \sqrt{3}L_L \frac{\mathrm{d}}{\mathrm{d}t}\begin{bmatrix} i_{0\alpha} \\ i_{0\beta} \end{bmatrix}. \tag{3.10}$$

3.2.2 Discrete-Time Model

This work formulates the PS-MPC strategy for an M3C to control the transformed cluster currents and to perform the LCB control in a simple and unified manner. For that purpose, the system state, at each instant k, is chosen as:

$$\boldsymbol{x}(k) = \left[\boldsymbol{i}^{\alpha\beta0\mathrm{T}}(k) \quad \boldsymbol{v}_{C,1}^{\mathrm{T}}(k) \quad \dots \quad \boldsymbol{v}_{C,N}^{\mathrm{T}}(k)\right]^{\mathrm{T}} \in \mathbb{R}^{8+9N} \tag{3.11}$$

where $\boldsymbol{i}^{\alpha\beta 0}(k) \in \mathbb{R}^8$ is the current vector in the double-$\alpha\beta 0$ framework and $\boldsymbol{v}_{C,j}(k) \in \mathbb{R}^9$ is the vector comprising the capacitor voltage of the j-SM of each cluster. Moreover, the control input vector, $\boldsymbol{u}(k)$, is defined by:

$$\boldsymbol{u}(k) = \begin{bmatrix} \boldsymbol{\delta}_1^{\mathrm{T}}(k) & \dots & \boldsymbol{\delta}_N^{\mathrm{T}}(k) \end{bmatrix}^{\mathrm{T}} \in \mathbb{D}^{9N} \tag{3.12}$$

where $\boldsymbol{\delta}_j(k)$ comprises the modulating signals arranged analogously as the capacitor voltage vector. The vectors in (3.11) and (3.12) are summarized in Table 3.1.

Additionally, the three-phase systems voltages at the input ($abc-$port) and output ($uvw-$port) of the converter in the $\alpha\beta 0$-framework are defined as:

$$\begin{aligned} \boldsymbol{v}_{\Psi}^{\alpha\beta}(k) &= \begin{bmatrix} v_{\Psi}^{\alpha}(k) & v_{\Psi}^{\beta}(k) \end{bmatrix}^{\mathrm{T}}, \\ \boldsymbol{v}_{\chi}^{\alpha\beta}(k) &= \sqrt{3} r_L \begin{bmatrix} i_{0\alpha} \\ i_{0\beta} \end{bmatrix} + \sqrt{3} L_L \frac{d}{dt} \begin{bmatrix} i_{0\alpha} \\ i_{0\beta} \end{bmatrix} \end{aligned} \tag{3.13}$$

Finally, by considering (3.11)–(3.13) and applying the forward Euler discretization to (3.4) and (3.7) using a sampling period T_s, the following discrete-time model can be obtained:

$$\boldsymbol{x}(k+1) = \mathbf{A}\boldsymbol{x}(k) + \mathbf{B}(\boldsymbol{x}(k))\boldsymbol{u}(k) + \mathbf{E}_{\Psi}\boldsymbol{v}_{\Psi}^{\alpha\beta}(k) \tag{3.14}$$

where

$$\begin{aligned} \mathbf{A} &= \begin{bmatrix} \mathbf{A}^{\mathrm{up}} & \mathbf{0}_{8\times 9N} \\ \mathbf{0}_{9N\times 8} & \mathbf{I}_{9N} \end{bmatrix}, \ \mathbf{E}_{\Psi} = \sqrt{3}\frac{T_s}{L} \begin{bmatrix} \mathbf{0}_{2\times 2} \\ 1 \quad 0 \\ \mathbf{0}_{2\times 2} \\ 0 \quad 1 \\ \mathbf{0}_{2+9N\times 2} \end{bmatrix}, \\ \mathbf{B}(\boldsymbol{x}(k)) &= \begin{bmatrix} \mathbf{B}_1^{\mathrm{up}}(\boldsymbol{x}_k) & \mathbf{B}_2^{\mathrm{up}}(\boldsymbol{x}_k) & \dots & \mathbf{B}_N^{\mathrm{up}}(\boldsymbol{x}_k) \\ \mathbf{B}_1^{\mathrm{lo}}(\boldsymbol{x}_k) & \mathbf{0}_{9\times 9} & \dots & \mathbf{0}_{9\times 9} \\ \mathbf{0}_{9\times 9} & \mathbf{B}_2^{\mathrm{lo}}(\boldsymbol{x}_k) & \ddots & \vdots \\ \vdots & \ddots & \ddots & \mathbf{0}_{9\times 9} \\ \mathbf{0}_{9\times 9} & \dots & \mathbf{0}_{9\times 9} & \mathbf{B}_N^{\mathrm{lo}}(\boldsymbol{x}_k) \end{bmatrix} \end{aligned} \tag{3.15}$$

with $\boldsymbol{x_k} := \boldsymbol{x}(k)$. This model arrangement will be exploited in the following section to design the proposed sequential PS-MPC control strategy.

3.3 PS-MPC of an M3C

This section formulates the proposed PS-MPC to directly govern the cluster currents in the double-$\alpha\beta 0$ framework and to balance the SM capacitor voltages in a unified and computation efficient manner. This formulation is not straightforward and is one of the contributions of this work.

3.3.1 Overall Optimal Control Problem

The main control targets are to balance the SMs capacitor voltages, and to track the desired references for input, output and circulating currents of the M3C, which can be expressed via:

$$\boldsymbol{x}^{\star}(k) = \begin{bmatrix} \boldsymbol{i}^{\alpha\beta 0 \star \mathrm{T}}(k) & \boldsymbol{v}_{C,1}^{\star \mathrm{T}}(k) & \dots & \boldsymbol{v}_{C,N}^{\star \mathrm{T}}(k) \end{bmatrix}^{\mathrm{T}} \tag{3.16}$$

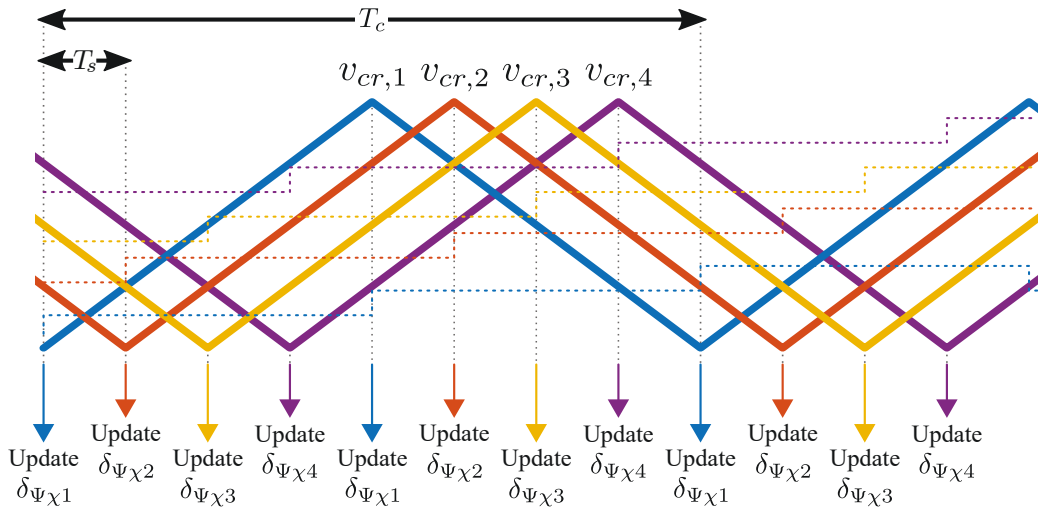

Figure 3.2: PS-PWM operating principle in double update mode for a four-sub-module arm.

In order to tackle this multi-variable closed-loop objective, the standard quadratic cost function is used:

$$J(k) = \left\|\boldsymbol{x}(k+1) - \boldsymbol{x}^{\star}(k+1)\right\|_{\mathbf{Q}}^{2} + \left\|\boldsymbol{u}(k) - \boldsymbol{u}^{\star}(k)\right\|_{\mathbf{\Lambda}}^{2} \tag{3.17}$$

where $\boldsymbol{u}^{\star}(k)$ is the required steady-state control input to keep the SMs capacitor voltages and the transformed cluster currents in the desired steady-state $\boldsymbol{x}^{\star}(k+1)$ as per (3.16). The diagonal matrix $\mathbf{\Lambda} = \lambda \mathbf{I}_{9N}$ is used to adjust the compromise between the state tracking error and the control effort, allowing the dynamic response of the closed-loop system to be modified [40]. Moreover, the weighting matrix $\mathbf{Q} = \text{diag}\left\{\sigma_1 \mathbf{I}_8, \sigma_2 \mathbf{I}_{9N}\right\}$ regulates the tracking error of the SMs capacitor voltages versus the cluster currents in the D-$\alpha\beta$0 framework.

3.3.2 Sequential Average Model of an M3C

This work considers the working principle of a PS-PWM to formulate a sequential PS-MPC for the M3C. For this converter, N carriers are phase shifted by π/N. Additionally, in a digital implementation, the control signals δ_{auj}, δ_{avj}, δ_{awj}, δ_{buj}, δ_{bvj}, δ_{bwj}, δ_{cuj}, δ_{cvj}, and δ_{cwj} are updated when its associated carrier $v_{cr,j}$ is at one of its edges (PS-PWM with double update). After that, these signals remain constant until the next update, which is after half of the carrier period ($T_c/2$). This leads to a sequential control signal update process as illustrated in Fig. 3.2 for $N = 4$ sub-modules. Notice that only nine modulating control signals (one sub-module per cluster) need to be obtained at each sampling instant, $T_s = T_c/(2N)$. If single-update is considered for the PS-PWM, the duty cycles are updated at the top or the bottom edges only, so the sampling time changes when updating the last sub-module to $(N+1)T_c/(2N)$. Because of these asymmetrical sampling times, the single-update of the PS-PWM is not commonly used for arms based on H-bridges.

Based on the double update operation of the modulator, it is possible to derive a sequential model of the M3C from (3.14) by considering at each sampling instant only the "actives" control signals $\boldsymbol{\delta}_j$ (the ones that needs to be updated) as control input as follows:

$$\boldsymbol{u}_j(k) = \boldsymbol{\delta}_j(k) \in \mathbb{D}^9 \tag{3.18}$$

and the sequential state vector as:

$$\boldsymbol{x}_j(k) = \begin{bmatrix} \boldsymbol{i}^{\alpha\beta 0\mathrm{T}}(k) & \boldsymbol{v}_{C,j}^{\mathrm{T}}(k) \end{bmatrix}^{\mathrm{T}} \in \mathbb{R}^{17} \tag{3.19}$$

Consequently, the dynamic model (3.14) can be re-written as:

$$\boldsymbol{x}_j(k+1)=\mathbf{A}_j\boldsymbol{x}_j(k)+\mathbf{B}_j\boldsymbol{u}_j(k)+\boldsymbol{h}_j(k) \tag{3.20}$$

with

$$\boldsymbol{h}_j(k)=\mathbf{E}_{\Psi,j}\boldsymbol{v}_{\Psi}^{\alpha\beta}(k)+\sum_{\substack{l=1\\l\neq j}}^{N}\begin{bmatrix}\mathbf{B}_l^{\text{up}}\\ \mathbf{0}_{9\times 9}\end{bmatrix}\boldsymbol{u}_l(k) \tag{3.21}$$

where $\boldsymbol{u}_l$ contains the "inactive" control signals that have been previously obtained. Therefore, $\boldsymbol{h}_j(k)$ can be seen as a known disturbance for the sequential average model and the sequential state, input and grid matrices are:

$$\begin{aligned}&\mathbf{A}_j=\begin{bmatrix}\mathbf{A}^{\text{up}} & \mathbf{0}_{8\times 9}\\ \mathbf{0}_{9\times 8} & \mathbf{I}_9\end{bmatrix}\in\mathbb{R}^{17\times 17},\ \mathbf{E}_{\Psi,j}=\frac{T_s}{L}\begin{bmatrix}\mathbf{0}_{2\times 2}\\ \sqrt{3}\quad 0\\ \mathbf{0}_{2\times 2}\\ 0\quad\sqrt{3}\\ \mathbf{0}_{11\times 2}\end{bmatrix}\in\mathbb{R}^{17\times 2},\\ &\mathbf{B}_j(\boldsymbol{x}_j(k))=\begin{bmatrix}\mathbf{B}_j^{\text{up}}(\boldsymbol{x}_j(k))\\ \mathbf{B}_j^{\text{lo}}(\boldsymbol{x}_j(k))\end{bmatrix}\in\mathbb{R}^{17\times 9}.\end{aligned} \tag{3.22}$$

3.3.3 Sequential Optimal Control Problem

By adopting the sequential average model in (3.20), the cost function (3.17) can be reduced taking into account only the active control signals, leading to the following sequential cost function:

$$J_j(k)=\left\|\boldsymbol{x}_j(k+1)-\boldsymbol{x}_j^{\star}(k+1)\right\|_{\mathbf{Q}_j}^2+\left\|\boldsymbol{u}_j(k)-\boldsymbol{u}_j^{\star}(k)\right\|_{\boldsymbol{\Lambda}_j}^2 \tag{3.23}$$

with

$$\mathbf{Q}_j=\begin{bmatrix}\sigma_1\mathbf{I}_8 & \mathbf{0}_{8\times 9}\\ \mathbf{0}_{9\times 8} & \sigma_2\mathbf{I}_9\end{bmatrix}\in\mathbb{R}^{17\times 17}\text{ and }\boldsymbol{\Lambda}_j=\lambda\mathbf{I}_9\in\mathbb{R}^{9\times 9}. \tag{3.24}$$

Therefore, the optimal PS-PWM active control signals are those that minimize this sequential cost function, i.e.:

$$\begin{aligned}\boldsymbol{u}_j^{\text{opt}}(k)=\arg\min_{\boldsymbol{u}_j(k)}\quad&\{J_j(k)\}\\ \text{s.t. }&-\mathbf{1}_{9\times 1}\leq\boldsymbol{u}_j(k)\leq\mathbf{1}_{9\times 1}\end{aligned} \tag{3.25}$$

Notice that (3.25) is in fact a box-constrained quadratic programming problem since $\boldsymbol{u}_j(k)\in\mathbb{D}^9\triangleq[-1,1]^9\subset\mathbb{R}^9$. In contrast to previous PS-MPC strategies reported in the literature (e.g., [22]–[24]), in which suboptimal solutions are obtained by using the saturated version of the unconstrained solution of (3.25), this work uses an exterior point active set method based on a Lagrangian function and the Karush-Kuhn-Tucker conditions to compute optimal duty cycles to be applied by the converter. For further details on the algorithm used in this work, we refer readers to [47]. The proposed optimal approach impacts the system's performance, especially during transients, as will be analyzed in the experimental validation of the proposed control strategy.

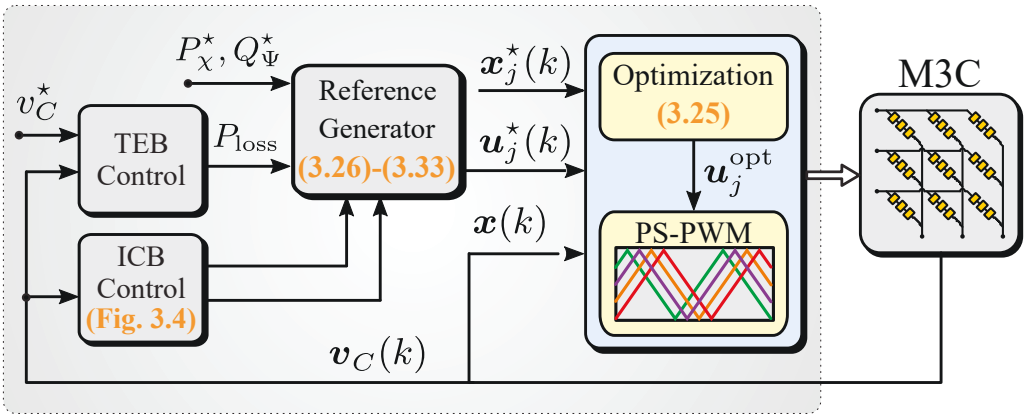

Figure 3.3: Overall control scheme.

3.4 References Design

The overall control strategy is shown in Fig. 3.3. This section aims to obtain the state references, $\boldsymbol{x}_j^\star(k)$, and the steady-state reference, $\boldsymbol{\delta}_j^\star$. Considering current of both ports, TEB and ICB controls.

$$\boldsymbol{x}_j^\star(k) = \left[\boldsymbol{i}^{\alpha\beta 0\star\mathrm{T}}(k) \quad \boldsymbol{v}_{C,j}^{\star\mathrm{T}}(k)\right]^{\mathrm{T}} \in \mathbb{R}^{17} \tag{3.26}$$

where each element of $\boldsymbol{v}_{C,j}^\star(k)$ is considered constant and equal to $v_{dc}^\star$. Additionally, the steady-state control inputs $\boldsymbol{u}_j^\star(k) = \boldsymbol{\delta}_j^\star(k) \in \mathbb{D}^9$ are also determined in this section.

3.4.1 Input and Output Current Reference

The references for input and output currents are designed in the $\alpha\beta 0$-framework. By considering an active power references for the output system, a symmetric current reference is obtained:

$$\boldsymbol{i}_\chi^{\alpha\beta} = \sqrt{\frac{P_\chi^\star}{r_L}} \begin{bmatrix} \sin(\omega_\chi t) \\ -\cos(\omega_\chi t) \end{bmatrix} \tag{3.27}$$

where $P_\chi^\star$ is the active power reference. Then, in order to regulate the average energy of the converter (TEB control), the required input active power $P_\Psi^\star$ must be the sum of the desired output active power $P_\chi^\star$ and the power consumed by the M3C, P_{loss}. This leads to the following expression for the input current reference:

$$\boldsymbol{i}_\Psi^{\alpha\beta} = \frac{1}{v_\Psi^{\alpha\,2} + v_\Psi^{\beta\,2}} \begin{bmatrix} v_\Psi^\alpha & v_\Psi^\beta \\ v_\Psi^\beta & -v_\Psi^\alpha \end{bmatrix} \begin{bmatrix} P_\chi^\star + P_{\text{loss}} \\ Q_\Psi^\star \end{bmatrix} \tag{3.28}$$

The power losses P_{loss} are obtained by the TEB control, which is composed by a PI controller as is shown in Fig. 3.3, that allows to regulate the internal energy of the converter by considering the tracking error of the sum of the capacitor voltage references and the sum of the capacitor voltage measurements.

Finally, the current references in the D-$\alpha\beta 0$ framework for both ports are given by:

$$\begin{bmatrix} i_{\alpha 0}^\star \\ i_{\beta 0}^\star \\ i_{0\alpha}^\star \\ i_{0\beta}^\star \end{bmatrix} = \frac{1}{\sqrt{3}} \begin{bmatrix} \boldsymbol{i}_\Psi^{\alpha\beta} \\ \boldsymbol{i}_\chi^{\alpha\beta} \end{bmatrix}. \tag{3.29}$$

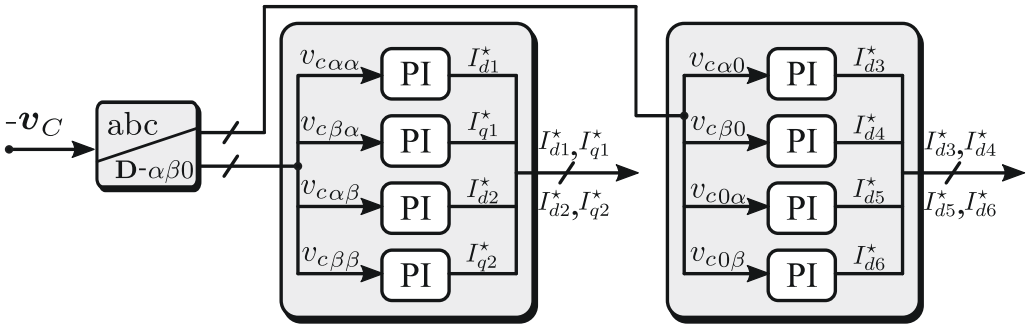

Figure 3.4: Inter-Cluster Balancing control proposed in [11].

3.4.2 Circulating Current Reference

The ICB control considers the energy balance among clusters, designing a proper circulating current. By analyzing the cluster powers and cluster voltages in the D-$\alpha\beta$0-framework the waveform for the circulating current can be deduced as presented in [11], [12], [25]. In this work, the ICB control introduced in [11] is implemented. Where the circulating currents are given by the sum of positive and negative sequence in phase with the input-port; and the amplitudes $I^\star_{d1}$, $I^\star_{d2}$, $I^\star_{d3}$, $I^\star_{d4}$, $I^\star_{d5}$, $I^\star_{d6}$, $I^\star_{q1}$ and $I^\star_{q2}$ are obtained by PI controllers in order to regulate the cluster imbalance in the D-$\alpha\beta$0-framework as shows Fig. 3.4.

3.4.3 Modulation Index Reference

The modulation index references for each arm is key to obtain a good steady-state performance and a reduced current spectra under the PS-MPC scheme. These references are generated by considering the system in the desired steady-state, i.e., $\boldsymbol{i}^{\alpha\beta0}(k) = \boldsymbol{i}^{\alpha\beta0\star}(k)$. Thus, by substituting the current references into the dynamic model (3.7), it is possible to calculate the desired steady-state voltages in the $\alpha\beta$0-framework as:

$$\begin{aligned}\begin{bmatrix} v^\star_{\alpha\alpha} & v^\star_{\beta\alpha} & v^\star_{0\alpha} \\ v^\star_{\alpha\beta} & v^\star_{\beta\beta} & v^\star_{0\beta} \\ v^\star_{\alpha0} & v^\star_{\beta0} & v^\star_{00} \end{bmatrix} &= \sqrt{3}\begin{bmatrix} 0 & 0 & 0 \\ 0 & 0 & 0 \\ v^\alpha_\Psi & v^\beta_\Psi & 0 \end{bmatrix} - L\frac{d}{dt}\begin{bmatrix} i^\star_{\alpha\alpha} & i^\star_{\beta\alpha} & i^\star_{0\alpha} \\ i^\star_{\alpha\beta} & i^\star_{\beta\beta} & i^\star_{0\beta} \\ i^\star_{\alpha0} & i^\star_{\beta0} & 0 \end{bmatrix} \\ &\quad -r\begin{bmatrix} i^\star_{\alpha\alpha} & i^\star_{\beta\alpha} & i^\star_{0\alpha} \\ i^\star_{\alpha\beta} & i^\star_{\beta\beta} & i^\star_{0\beta} \\ i^\star_{\alpha0} & i^\star_{\beta0} & 0 \end{bmatrix} - \sqrt{3}\begin{bmatrix} 0 & 0 & v^\alpha_\chi \\ 0 & 0 & v^\beta_\chi \\ 0 & 0 & 0 \end{bmatrix} - \begin{bmatrix} 0 & 0 & 0 \\ 0 & 0 & 0 \\ 0 & 0 & 3v_{no} \end{bmatrix}\end{aligned} \tag{3.30}$$

Then, by premultiplying by $\left[\mathbf{C}^{\alpha\beta0}\right]^{\mathrm{T}}$ and postmultiplying by $\left[\mathbf{C}^{\alpha\beta0}\right]$, the voltages obtained in (3.30) can be represented in the original framework:

$$\begin{bmatrix} v^\star_{au} & v^\star_{bu} & v^\star_{cu} \\ v^\star_{av} & v^\star_{bv} & v^\star_{cv} \\ v^\star_{aw} & v^\star_{bw} & v^\star_{cw} \end{bmatrix} = \left[\mathbf{C}^{\alpha\beta0}\right]^{\mathrm{T}} \begin{bmatrix} v^\star_{\alpha\alpha} & v^\star_{\beta\alpha} & v^\star_{0\alpha} \\ v^\star_{\alpha\beta} & v^\star_{\beta\beta} & v^\star_{0\beta} \\ v^\star_{\alpha0} & v^\star_{\beta0} & v^\star_{00} \end{bmatrix} \left[\mathbf{C}^{\alpha\beta0}\right]. \tag{3.31}$$

Thus, the modulation index are obtained by dividing the desired ac cluster voltage $v^\star_{\Psi\chi}$ by the available cluster capacitor voltage:

$$\delta^\star_{\Psi\chi j} = \frac{v^\star_{\Psi\chi}}{\sum_{l=1}^{N} v_{C,\Psi\chi l}}. \tag{3.32}$$

Table 3.2: System Parameters for Comparison.

Variable	Description	Comparison
P	Rated power	3 kW
v_Ψ	Input grid voltage (line-to-line rms)	190 V
f_Ψ	Input grid frequency	60 Hz
r_L	Output resistance	14 Ω
L_L	Output inductance	1 mH
f_χ	Output frequency	50 Hz
N	SMs per clusters	4
C	SM capacitance	987 μF
$v_{dc}^\star$	dc cap. voltage per SM	100 V
L	Cluster filter inductance	5 mH
r	Cluster filter resistance	0.1 Ω
f_{cr}	Carrier frequency	1 kHz

Finally, the input reference $\boldsymbol{u}_j^\star$ required by the proposed controller in (3.23) is obtained by arranging multiple modulation indexes as:

$$\boldsymbol{\delta}_j^\star = \left[\delta_{auj}^\star\, \delta_{avj}^\star\, \delta_{awj}^\star\, \delta_{buj}^\star\, \delta_{bvj}^\star\, \delta_{bwj}^\star\, \delta_{cuj}^\star\, \delta_{cvj}^\star\, \delta_{cwj}^\star\right]^{\mathrm{T}}. \tag{3.33}$$

3.5 Control Strategies Comparison

Simulation results have been performed to compare the proposed sequential PS-MPC strategy performance with existing strategies when governing an M3C connected to a three-phase system and a passive load. The parameters used for simulations are presented in Table 3.2.

Two strategies have been considered to compare the proposal, the first control strategy is the standard PI strategy for the current and LCB control presented in [11], [12], [16], [17] and a reduced FCS-MPC strategy [34]. The PI strategy considers four PIs controllers to control the input and output currents in two dq-frameworks, four proportional (P) controllers to govern the circulating currents and 36 P controllers to achieve the balance among SMs. The second control strategy is based on a FCS-MPC strategy [34]. The FCS-MPC considers the feasible SM output voltage, so for a four-SM M3C converter the total states are $3^{9N} = 3^{36} \approx 1.5\times10^{17}$ which cannot be implemented in a simulation environment, even less in a real application. However, the total combinations can be reduced by considering the common-mode voltage as a known disturbance. Therefore, the total combinations are reduced to $9 \times 3^N = 9 \times 3^4 = 729$, making its implementation feasible, at least in simulation. Nonetheless, the computational burden of this predictive strategy increases exponentially with the number of SMs of the converter. As the common-mode voltage is considered as a known disturbance, each cluster is decoupled in terms of control objectives of the others. In terms of control structure, the proposed PS-MPC and FCS-MPC strategies present a simpler structure than the PI strategy, reducing from four PIs and 40 Ps SISO controllers to one MIMO controller. The tuning process of the predictive strategies is heuristic, considering standard steps. Regarding the PI controllers, the tuning was made in order to obtain a second-order close-loop response with a natural frequency of 150 Hz and a damping factor of 0.7071 and the LCB proportional controllers were tuned with a gain of 0.1.

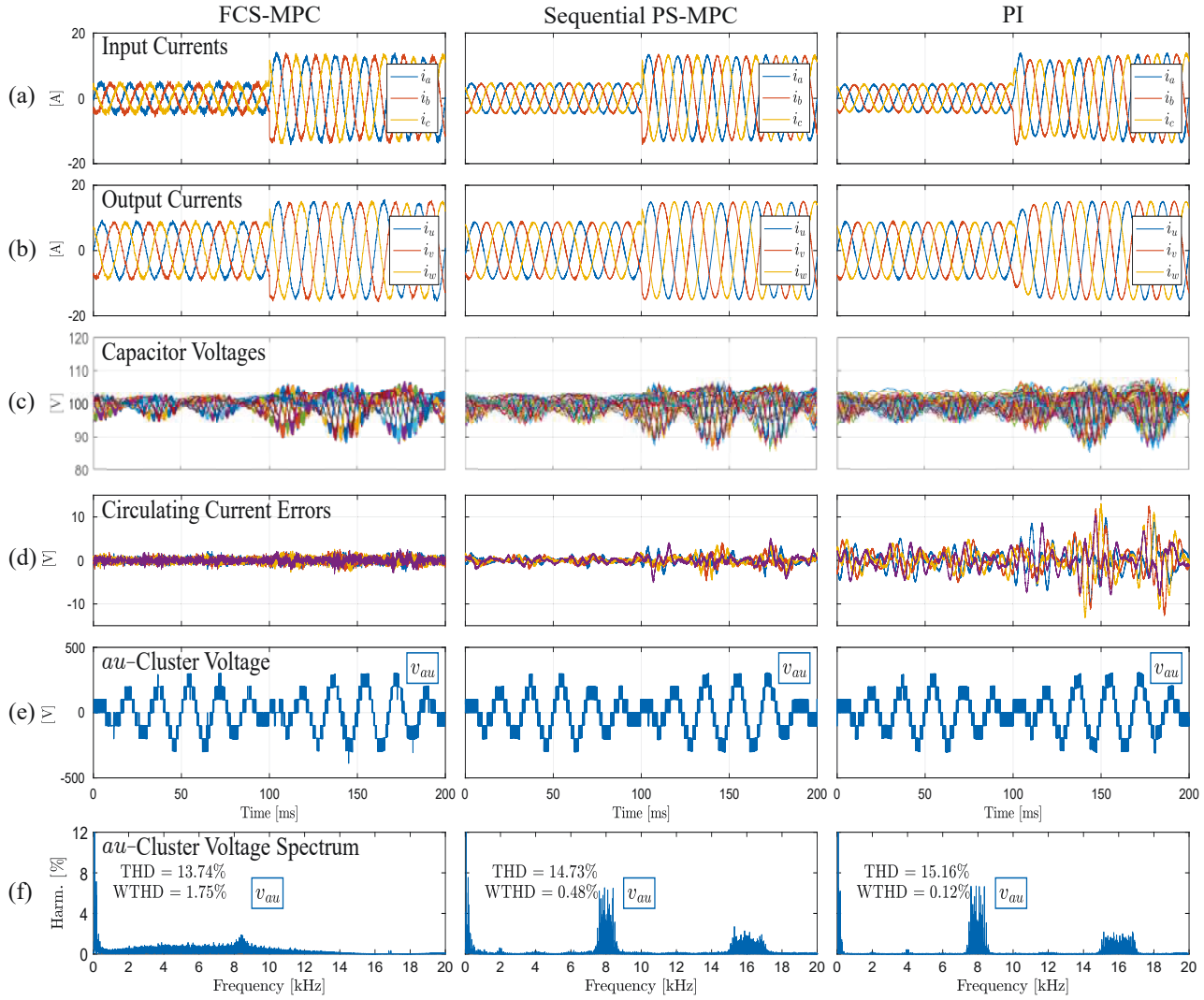

Figure 3.5: Simulation comparison, FCS-MPC strategy (left), the proposed sequential PS-MPC strategy (middle) and PI in dq-framework strategy proposed in [11] (right). (a) input currents, (b) output currents, (c) capacitor voltages, (d) circulating currents tracking error, (e) au-cluster voltage and (f) au-cluster voltage spectra.

The comparison of the three strategies is shown in Fig. 3.5 and Fig. 3.6. In steady-state, all the strategies achieve the references, obtaining balanced input and output currents, and balanced clusters and SMs with a mean capacitor voltage equal to 100 V as present Fig. 3.5a, Fig. 3.5b and Fig. 3.5c. However, the proposal achieves a mix of advantages from the other two strategies, such as, fast dynamic and tracking error response, low harmonic distortion and scalability.

Power Step Change

The comparison in terms of input and output currents are presented in Fig. 3.5a and 3.5b. In term of the settling time, the dynamic response of the predictive strategies is considerably faster than the PI strategy. The response of the FCS-MPC and PS-MPC is practically instantaneous, in contrast, the PI strategy achieves the input and output current reference after 60 and 25 ms, respectively.

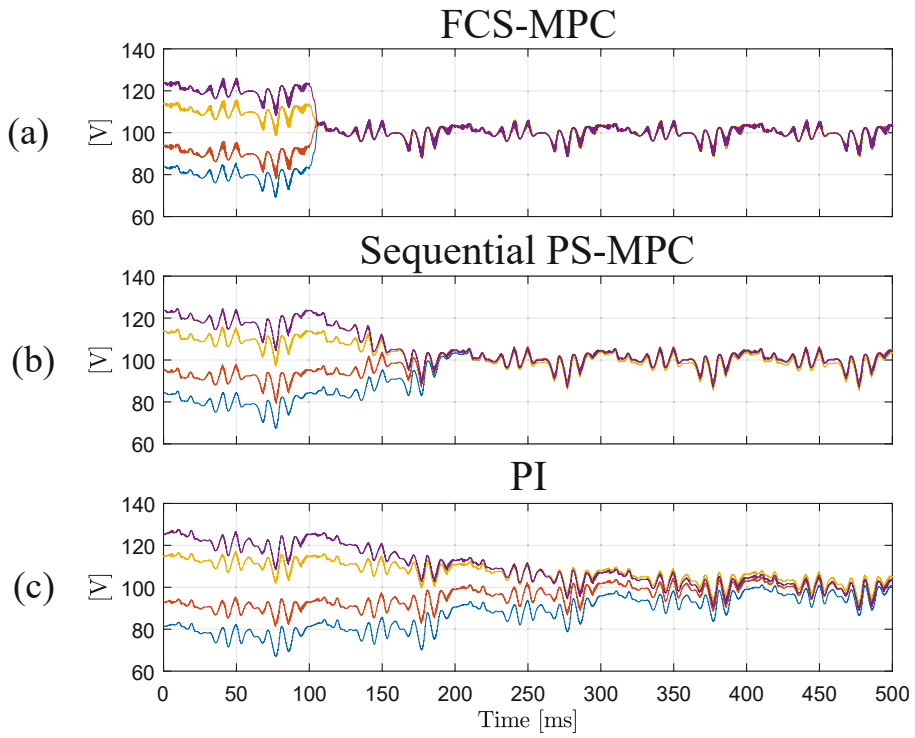

Figure 3.6: Comparison under local-cluster imbalance. Capacitor voltages of *au*-cluster with (a) FCS-MPC strategy, (b) sequential PS-MPC proposed strategy and (c) PI strategy.

Circulating Current Tracking

The circulating current tracking error for the PI strategy is bounded by ±15 A. Nevertheless, the tracking error for the predictive strategies is lower than 5 A, where he FCS-MPC achieves the best performance (Fig. 3.5d).

Cluster Voltages

The *au*-cluster voltage and its spectrum are presented in Fig. 3.5e and Fig. 3.5f, respectively. The FCS-MPC strategy generates a disperse spectrum around 8 kHz as it does not have a modulator. On the other hand, the PS-MPC and PI strategies generate a spectrum centered on 8 kHz and its multiples, which comes from the PS-PWM with 1 kHz carriers ($f_{o,sw} = 2Nf_{cr} = 8$ kHz). The PI strategy generates the highest cluster voltage THD (15.16%), while the FCS-MPC strategy has the lowest THD (13.74%). Additionally, the FCS-MPC strategy has the highest weighted total harmonic distortion (WTHD=1.75%), and the PI strategy has the lowest WTHD (0.12%). In summary, the proposal considerably reduces the WTHD (73% lower than the FCS-MPC), achieving a lower input and output current ripple than the FCS-MPC (see Fig. 3.5a and 3.5b), and limiting the frequency spectrum to a band determined by the PS-PWM.

Local-Cluster Balancing Control

The performance of the LCB control is shown in Fig. 3.6. At the beginning, the capacitor voltage references of the *au*-cluster are set for different values while maintaining its average voltage of 100 V. At the instant $t = 100$ ms, the references for all capacitor voltages are set to 100 V. The FCS-MPC strategy achieves the fastest dynamic response ($t = 110$ ms), followed by the proposed PS-MPC ($t = 180$ ms), and far behind is the classical PI strategy ($t = 475$ ms). The PI strategy adjusts the duty cycle per SM using a proportional controller before the

Table 3.3: Comparison among the proposed and existing control methods in steady-state at 3 kW ($N = 4$).

	PI [4]	FCS-MPC	Proposed
Controller	Multiple PI Loops	Reduced FCS-MPC	Sequential PS-MPC
Cluster coupling consideration	No	No	Yes
Average current tracking error	16.02 %	4.13 %	8.55 %
Average voltage tracking error	2.59 %	2.03 %	2.18 %
Average SM switching frequency	2 kHz	3.6 kHz	2 kHz
Input/output current quality	Very good	Fair (noisy)	Very Good
Input/output current response	Slow	Fast	Fast
Capacitor voltage balance	Slow	Very fast	Fast
Circulating current tracking error	High peaks	Noisy with very low peaks	Noiseless with low peaks
Output voltage THD	15.16%	13.74%	14.73%
Output voltage WTHD	0.12%	1.75%	0.48%
Output voltage spectrum	Fixed at 8 and 16 kHz	Spread at low frequencies (<12 kHz)	Fixed at 8 and 16 kHz
Modulation	PS-PWM (1 kHz)	None	PS-PWM (1 kHz)
Sample time	125 [μs]	*60 [μs]	125 [μs]
Scalability effort	Low	High (exponentially with N)	Low

*The sampling time was adjusted in order to obtain an average switching frequency of 8 kHz.

modulation stage. When the duty cycle saturates, its control action is limited. Unlike the PI, which considers two stages to control currents and balance capacitors, the PS-MPC controls currents and balances capacitors in a single stage. The formulated PS-MPC optimizes each duty cycle, adjusting the duty cycle to balance the voltage of the SMs by considering not only the tracking error of capacitor voltages, but the tracking error of the current and steady-state duty cycle reference. Therefore, the boundary of the SM balancing control depends on the tracking errors, the control effort and the weighting factors.

The Table 3.3 summarizes the comparison among the control strategies. The proposed sequential PS-MPC, against the standard PI strategy, presents a faster dynamic response, a better cluster current and voltage tracking. The proposal overcomes the FCS-MPC with a lower WTHD and a fixed frequency spectrum. Moreover, unlike the FCS-MPC, the computational burden does not depend of the number of SMs, the predictive model considers the coupling among clusters and a lower average SM switching frequency. In terms of average tracking error, the best strategy is the reduced FCS-MPC with a current and voltage error of 0.48 A and 2.03 V, the worst strategy is the PI with a current and voltage error of 1.57 A and 2.59 V. So, the performance of the proposed sequential PS-MPC is a balance between the PI and FCS-MPC strategies. The differences between the predictive strategies and the PI strategy, in terms of tracking error, is given by capability to track multiple-frequency waveforms that the predictive strategies have.

Finally, it is important to emphasise that even though FCS-MPC might offer some benefits when compared to the proposed PS-MPC (e.g., fast capacitor voltage balancing), its disadvantages are substantial: 1) it has a dispersed frequency spectrum that complicates the design of reactors and filters, in addition to producing random switching losses and low-order harmonics (it has the highest WTHD) (see Fig. 3.5); 2) it has the highest average SM switching frequency, leading to a higher power losses than the other strategies (see Table 3.3); and 3) it has a high computational cost that cannot be implemented when the number of SMs increases (see Section 3.6.3).

These are where the benefits of the proposed PS-MPC can be appreciated, as will be experimentally validated in the following Section.

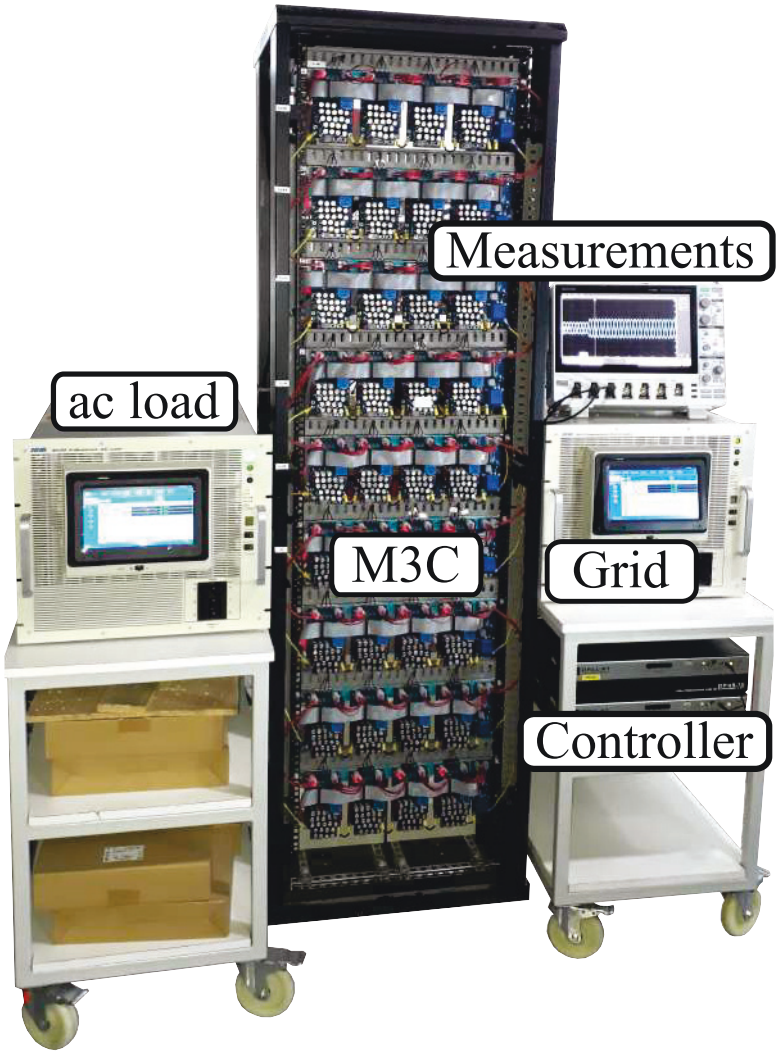

Figure 3.7: 3 kVA experimental prototype

3.6 Experimental Results

Experimental results have been performed to analyze and verify the proposed sequential PS-MPC strategy performance when governing an M3C connected to a three-phase system and a passive load. The grid-voltage of the first system was generated by a grid-simulator NHR9410 and the passive load of the second was generated by a regenerative ac load NHR9430. The predictive control scheme was implemented on an OPAL-RT OP4510 system. The data is acquired by the OPAL-RT software every 62.5 μs and is not post-processed. The prototype is presented in Fig. 3.7 and the main setup parameters are summarized in Table 3.4. The proposed PS-MPC generates an apparent output switching frequency of $f_{o,sw} = 2Nf_{cr} = 16$ kHz. However, since a double update mode is considered, it results in a sampling frequency of $f_s = 32$ kHz. Additionally, the PS-MPC was tuned heuristically with $\sigma_1 = 1$, $\sigma_2 = 0.2$ and $\lambda = 20$ [22], [23], and the execution time is $T_e = 7.5$ μs.

3.6.1 Steady-State Performance.

The results of the closed-loop steady-state performance are presented in the left side of the Fig. 3.8. The sequential PS-MPC is able to properly govern the M3C, achieving a symmetric

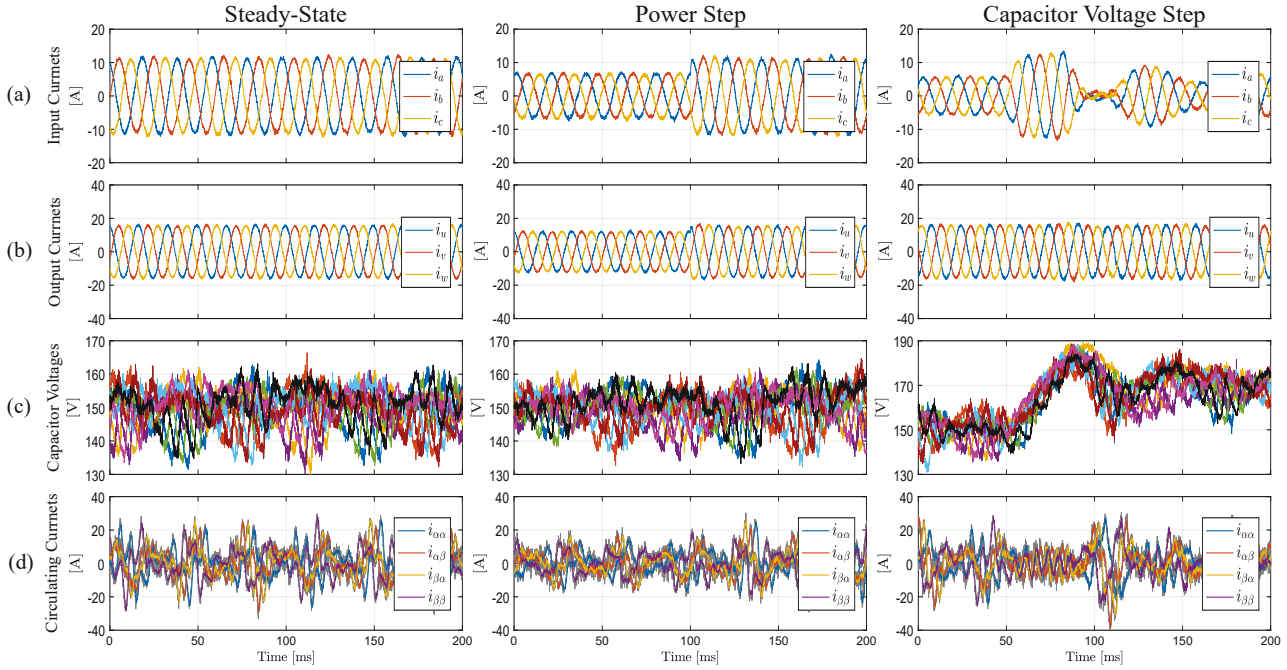

Figure 3.8: Experimental steady-state performance (left), dynamic response performance under a sudden power change (middle) and dynamic response under a sudden capacitor voltage change (right). (a) input currents, (b) output currents, (c) capacitor voltages and (d) circulating current.

Table 3.4: System Parameters for Experimental Results.

Variable	Description	Fig. 3.8 / Other
P	Rated power	5 / 3 kW
v_Ψ	Input grid voltage (line-to-line rms)	380 / 190 V
f_Ψ	Input grid frequency	50 / 60 Hz
r_L	Output resistance	14 Ω
L_L	Output inductance	1 mH
f_χ	Output frequency	60 / 10-59 Hz
N	SMs per clusters	4
C	SM capacitance	987 μF
$v_{dc}^\star$	dc cap. voltage per SM	150 / 100 V
L	Cluster filter inductance	5 mH
r	Cluster filter resistance	0.1 Ω
f_{cr}	Carrier frequency	2 kHz

waveform for the input and the output currents as shown Figs. 3.8a and 3.8b. Additionally, in Fig. 3.8c, the control strategy successfully regulates the capacitor voltages, keeping them around the reference of 150 V. Moreover, the circulating currents are properly tracked in order to balance the converter clusters and reduce the capacitor voltage ripple. It is important to mention that this control strategy is able to track any current waveform, including several frequencies in comparison with other control strategies that uses proportional controllers [11], [12], [16], [17]. This can be seen in Fig. 3.8d, where the circulating currents are tracked and

they present more than one frequency (references are presented behind in gray).

3.6.2 Dynamic Performance

The results of the closed-loop dynamic response performance are presented in the middle and right side of the Fig. 3.8. The middle part of Fig. 3.8 corresponds to the dynamic response of the control strategy under a step change in the power transferred from the input- to the output-port from 3 kW to 5 kW and the right side is the dynamic response under a step change in the capacitor voltage reference of each sub-module from 150 V to 170 V.

Power Step Change

The dynamic response, in terms of a sudden power change, is almost instantaneous and does not present overshoot. The peak value of the input and output currents increase due to the power step and the speed of the change is fast as it is shown in Figs. 3.8a and 3.8b. In Fig. 3.8c, the ripple of the capacitor voltages augment because the power step, nevertheless, the mean value of the capacitor remains constant. Finally, the circulating currents increase their peak values proportional to the change of the power and, despite the step change, the tracking error is properly followed as Fig. 3.8d shows.

Capacitor Voltage Step Change

The results of the dynamic response under a step change in the capacitor voltages are presented in the right side of the Fig. 3.8. In terms of capacitor voltage, the dynamic response is mainly given by the outer PI controller since this PI regulates the inner energy of the converter which is directly related with the capacitor voltages and this behavior can be seen in Fig. 3.8c. Additionally, the input current in Fig.3.8a is directly affected by the outer PI controller because this creates the reference, P_{loss}, that is used for the reference of the input currents. Nonetheless, the output current is not directly affected by the outer PI, the speed of the stabilization is mainly given by the sequential PS-MPC as is shown in Fig. 3.8b. Finally, the circulating current reference, in Fig. 3.8d are slightly reduced due to the increment of the capacitor voltage reference. This occurs because the system is still exchanging the same energy from input to output and the relation between the energy and the capacitor voltage is quadratic.

Different Output Frequencies Performance

The proposed strategy allows to govern the M3C for different output frequencies, Fig. 3.9 shows experimental results for three different output frequencies (50 Hz, 10 Hz and 59 Hz, respectively). The illustrated measurements are the phase-a current, the phase-u current, the au-cluster current, and the output voltage of au-cluster with its frequency domain. The output current is achieved independent of the frequency. Moreover, the converter is able to operate close to critical points (0 and 60 Hz). Mitigation currents must be considered in order to achieve critical points; however, this is not the scope of this proposal. Considering a carrier frequency of 2 kHz and a PS-PWM modulation, the output voltage spectrum is centered at 16 kHz, this behavior occurs for the three cases. The phase-a input current presents a THD of 2.29% and a WTHD of 0.59%. On the other hand, the phase-u output current has a lower THD and WTHD, which are 0.79% and 0.15%, respectively. These different behaviors between input and output currents, in terms of distortion, is mainly given by the PI controller which regulates the

(a)

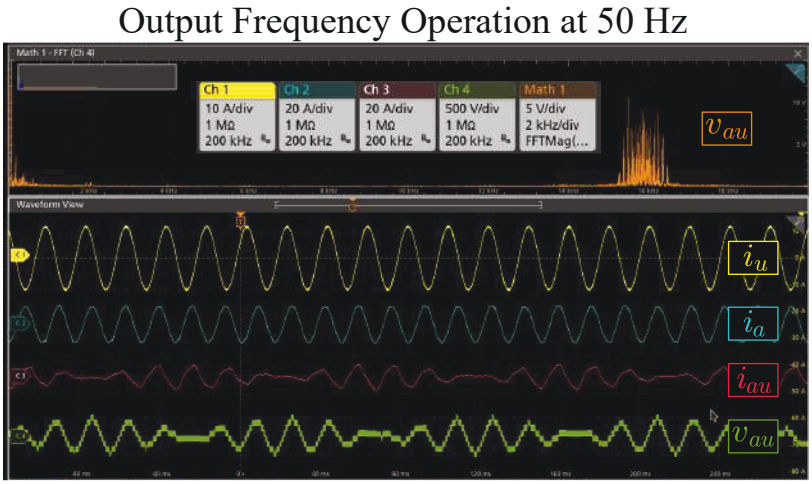

(b)

(c)

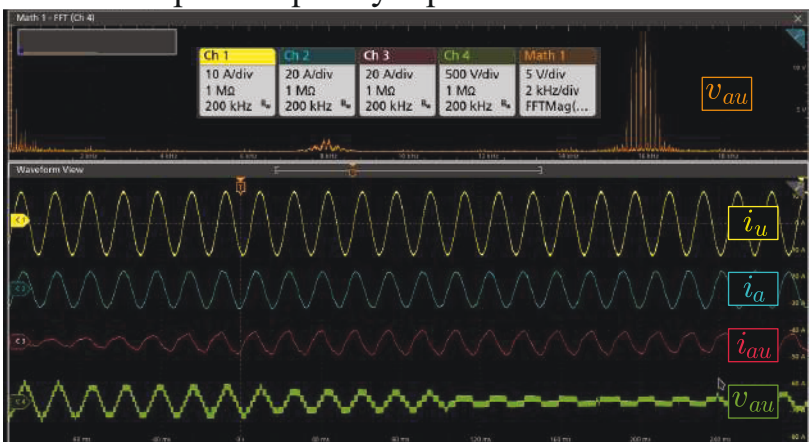

Figure 3.9: Experimental steady-state performance. (Ch 1) output current u, (Ch 2) input current a, (Ch 3) current au-cluster, (Ch 4) output voltage au-cluster, and (Math 1) output voltage au-cluster spectrum. (a) output frequency at 50 Hz, (b) output frequency at 10 Hz, and (c) output frequency at 59 Hz.

average energy of the converter because it directly affects the reference generation of the input currents.

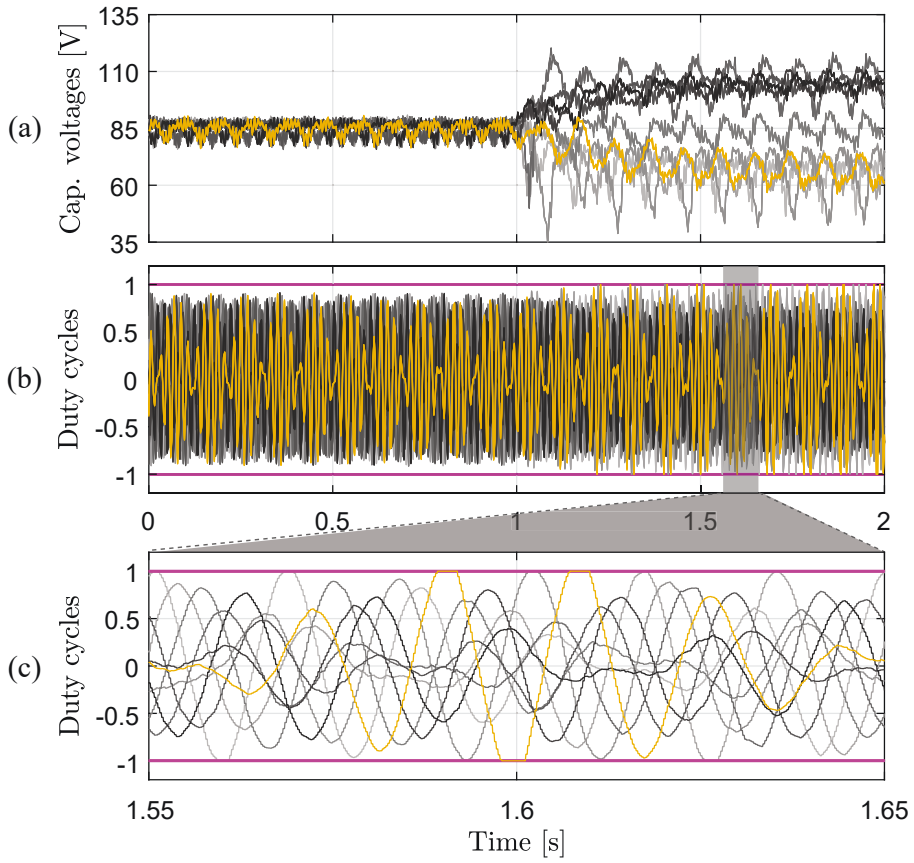

Figure 3.10: Experimental constraints activation under an imbalance condition. (a) capacitor voltages, (b) control signals and (c) control signals zoom.

Optimization with Active Constraints

The proposal obtains the optimal duty cycles considering upper and lower constraints, this is shown in Fig. 3.10 where the operating point of the M3C is set in order to force the activation of constraints. The constraints are activated by considering a mean capacitor voltage reference equal to 85 V and forcing a cluster imbalance. The duty cycles generated by the proposed sequential PS-MPC are always optimal, during transient and steady-state, feature that standard control strategies are not able to achieve.

3.6.3 Scalability Analysis of PS-MPC

The dimension of the optimal problem solved by the sequential PS-MPC is fixed, independently of the number of SMs. By increasing the number of SMs, the expected behavior in the execution time is a linear increment due to each SM contributes to the output voltage, but only one is optimized per sampling time. This linear behavior in the execution time was experimentally proved by the OPAL-RT OP4510. Additionally, the computational burden of the PI and FCS-MPC as function of the number of SMs is presented in Fig. 3.11. The execution time of the sequential PS-MPC and the PI strategies increase linearly with the number of SMs, meanwhile, the increment of the execution time of the FCS-MPC strategy is exponential, limiting the implementation of the FCS-MPC in real-time applications to a reduced number of SMs.

In MMCCs with a large number of SMs for high power and high voltage applications, the carrier frequency should be set as low as possible to reduce the switching losses. The sampling

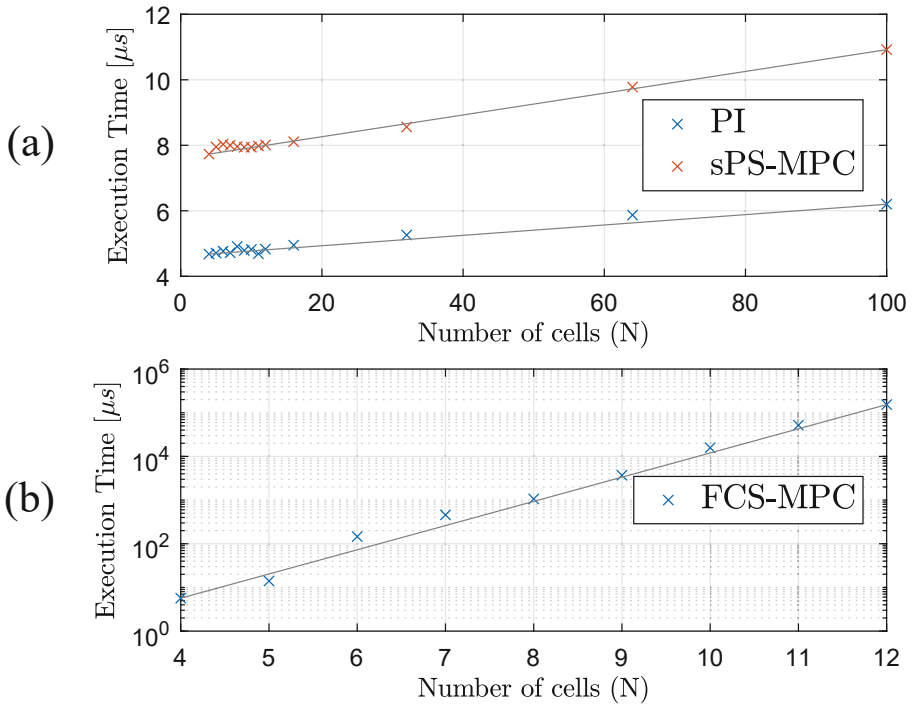

Figure 3.11: Experimental execution time control strategies. (a) PI and sequential PS-MPC strategies and (b) FCS-MPC strategy.

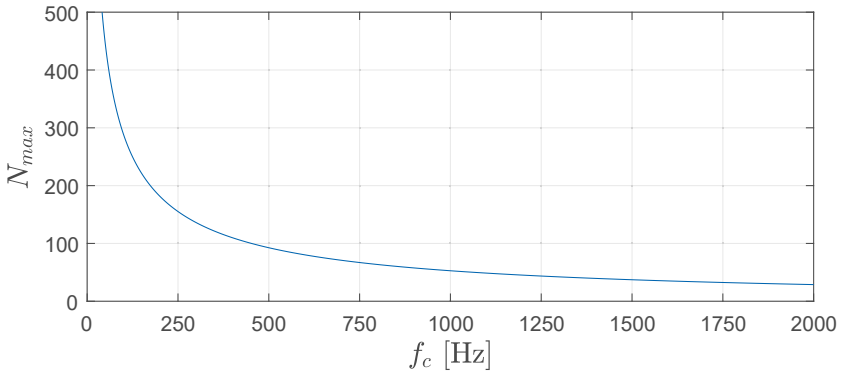

Figure 3.12: Maximum number of SMs per carrier frequency that the proposal can handle considering the linear execution time presented in Fig. 3.11.

frequency of the proposal is given by $T_s = 1/(2Nf_c)$. Therefore, in order to estimate the maximum number of SM per cluster that the proposal can handle as function of the carrier frequency, it is important to determine the execution time as function of N, which is provided in Fig. 3.11a. Finally, by considering the sampling time equal to the execution time $T_{\text{ex}} = T_s = 1/(2Nf_c)$, the maximum number of SM that the proposal is able to govern as function of the carrier frequency is presented in Fig. 3.12. It is estimated that the sequential PS-MPC can drive up to 32 SMs per cluster for a carrier frequency of 2 kHz, and up to 249 SMs per cluster when the carrier frequency is reduced to 125 Hz.

3.7 Conclusion

This chapter proposed the formulation and assessment of a sequential PS-MPC strategy to govern an M3C. The proposed controller effectively performs the LCB control task and regulates the input, output, and circulating currents in a single control stage, using an MPC embedded with the load and control input model directly in the optimization. Furthermore, by exploiting the PS-PWM working principle, the proposed PS-MPC method updates, at each sampling instant, only one control signal for every cluster. This significantly reduces the computational burden of the controller, while making it independent of the number of sub-modules. Therefore, the PS-MPC can be easily scalable to govern M3C with a large number of SMs.

As evidenced by the experimental results, the proposed PS-MPC formulation results in a fast closed-loop dynamic response and effective tracking of the input, output, and circulating currents. In addition, the proposal considers the control input limits in the optimization process and obtains the optimal duty cycles during steady-state and transients. Moreover, the M3C governed by the proposed PS-MPC operates with a fixed switching frequency, low harmonic distortion, and distributed power losses among power switches.

Appendix

State Matrix Component of M3C Model

Matrix $\mathbf{A}^{\text{up}}(k)$, presented in the M3C model (3.14) and the sequential model (3.22), is given by:

$$\mathbf{A}^{\text{up}} = \text{diag}\left\{\begin{bmatrix} 1-\frac{r}{L}T_s \\ 1-\frac{r}{L}T_s \\ 1-\frac{r}{L}T_s \\ 1-\frac{r}{L}T_s \\ 1-\frac{r}{L}T_s \\ 1-\frac{r}{L}T_s \\ 1-\frac{r_{eq}}{L_{eq}}T_s \\ 1-\frac{r_{eq}}{L_{eq}}T_s \end{bmatrix}\right\} \tag{3.34}$$

where $r_{eq} = r + 3r_L$ and $L_{eq} = L + 3L_L$.

Input Matrix Components of M3C Model

Matrix $\mathbf{B}_j^{\mathrm{up}}(k)$, presented in the M3C model (3.14) and the sequential model (3.22), is given by:

$$\mathbf{B}_j^{\mathrm{up}}(k) = -T_s \begin{bmatrix} \frac{1}{L}\, \boldsymbol{v}_{C,j}^{\mathrm{T}}(k)\mathbf{M}_{\alpha\alpha} \\ \frac{1}{L}\, \boldsymbol{v}_{C,j}^{\mathrm{T}}(k)\mathbf{M}_{\alpha\beta} \\ \frac{1}{L}\, \boldsymbol{v}_{C,j}^{\mathrm{T}}(k)\mathbf{M}_{\alpha 0} \\ \frac{1}{L}\, \boldsymbol{v}_{C,j}^{\mathrm{T}}(k)\mathbf{M}_{\beta\alpha} \\ \frac{1}{L}\, \boldsymbol{v}_{C,j}^{\mathrm{T}}(k)\mathbf{M}_{\beta\beta} \\ \frac{1}{L}\, \boldsymbol{v}_{C,j}^{\mathrm{T}}(k)\mathbf{M}_{\beta 0} \\ \frac{1}{L_{eq}}\, \boldsymbol{v}_{C,j}^{\mathrm{T}}(k)\mathbf{M}_{0\alpha} \\ \frac{1}{L_{eq}}\, \boldsymbol{v}_{C,j}^{\mathrm{T}}(k)\mathbf{M}_{0\beta} \end{bmatrix} \tag{3.35}$$

where

$$\mathbf{M}_{\alpha\beta} = \begin{bmatrix} c_1^{\alpha}\mathrm{diag}\left(\boldsymbol{C}^{\beta}\right) & \mathbf{0}_{3\times 3} & \mathbf{0}_{3\times 3} \\ \mathbf{0}_{3\times 3} & c_2^{\alpha}\mathrm{diag}\left(\boldsymbol{C}^{\beta}\right) & \mathbf{0}_{3\times 3} \\ \mathbf{0}_{3\times 3} & \mathbf{0}_{3\times 3} & c_3^{\alpha}\mathrm{diag}\left(\boldsymbol{C}^{\beta}\right) \end{bmatrix}. \tag{3.36}$$

Moreover, matrix $\mathbf{B}_j^{\mathrm{lo}}(k)$ is given by:

$$\mathbf{B}_j^{\mathrm{lo}}(k) = \frac{T_s}{C}\mathrm{diag}\left\{\left(\begin{bmatrix} \mathbf{C}^{\alpha\beta 0} & \mathbf{0}_{3\times 3} & \mathbf{0}_{3\times 3} \\ \mathbf{0}_{3\times 3} & \mathbf{C}^{\alpha\beta 0} & \mathbf{0}_{3\times 3} \\ \mathbf{0}_{3\times 3} & \mathbf{0}_{3\times 3} & \mathbf{C}^{\alpha\beta 0} \end{bmatrix}^{\mathrm{T}} \mathbf{T}\right)^{2} \begin{bmatrix} \boldsymbol{i}_{\alpha\beta 0}(k) \\ 0 \end{bmatrix}\right\} \tag{3.37}$$

with

$$\mathbf{T} = \begin{bmatrix} 1 & 0 & 0 & 0 & 0 & 0 & 0 & 0 & 0 \\ 0 & 0 & 0 & 1 & 0 & 0 & 0 & 0 & 0 \\ 0 & 0 & 0 & 0 & 0 & 0 & 1 & 0 & 0 \\ 0 & 1 & 0 & 0 & 0 & 0 & 0 & 0 & 0 \\ 0 & 0 & 0 & 0 & 1 & 0 & 0 & 0 & 0 \\ 0 & 0 & 0 & 0 & 0 & 0 & 0 & 1 & 0 \\ 0 & 0 & 1 & 0 & 0 & 0 & 0 & 0 & 0 \\ 0 & 0 & 0 & 0 & 0 & 1 & 0 & 0 & 0 \\ 0 & 0 & 0 & 0 & 0 & 0 & 0 & 0 & 1 \end{bmatrix}. \tag{3.38}$$

Chapter 4

CONSTRAINED MPC FOR INTER–CLUSTER ENERGY CONTROL OF MODULAR MULTILEVEL MATRIX CONVERTERS

4.1 Introduction

Modular multilevel matrix converters (M3Cs) have emerged as an attractive and suitable alternative to directly interlink two AC systems at medium or high voltage, presenting several prominent advantages, such as modularity, scalability, power quality, and fault-tolerant operation capability [36]. Some applications of the M3C are low-frequency AC (LFAC) transmission systems [48], power-flow control for power distribution systems [13], medium-voltage static synchronous compensators [28], high-power motor drives [49], railway power conditioning [50], and high-power wind energy conversion systems (WECSs) [11].

The three-phase M3C, also known as triple-star bridge cell converter [51], is characterized by the series connection of sub-modules (SM), usually based on full-bridges (FB) with floating DC-capacitors, as illustrated in Fig. 4.1. Thus, depending on the voltage level required by a specific application, the M3C voltage rating can be easily enlarged by increasing the number of SMs per cluster N. As shown in Fig. 4.1(b), the cluster of N sub-modules connected in series along with a single inductor L constitute a branch (or arm).

In the M3C, the AC-AC power conversion is directly performed without the need of a intermediate DC stage, which significantly reduces the voltage oscillations of the SM capacitor voltages, compared with Modular Multilevel Converters (M2C), when the frequency on the output side is low (around units of Hz) [17], [44]. Consequently, lower circulating currents and common-mode voltage (CMV) are required to mitigate the capacitor voltage oscillations compared with those required in the M2C [17], [49]. This advantage makes the M3C a promising topology for high-power variable-speed drives, such as medium-voltage motor drives [44], offshore wind-power generations [11], and LFAC transmission systems [52]. Moreover, and in contrast to the back-to-back-M2C topology, the control system driving the M3C can still be extended when

the converter operates with lower branches [53].

M3Cs require many passive and active components to process electrical power, as shown in Fig. 4.1. Consequently, these converters must govern not only external variables at their input and output ports, but also multiple internal ones. Thus, the required multivariable control scheme is normally accomplished by using various control loops, some coupled to each other and others uncoupled, making them challenging design and implement. Among the control tasks to be performed, the SM capacitor voltages regulation is fundamental to achieve a high-performance current control system, improving power quality in terms of reactive power and harmonics. Usually, the SM capacitor-voltages regulation is performed by implementing four control processes [12], [25], [32], [45]:

(1) Total Energy Balancing (TEB) Control. Regulate the energy stored in all capacitors to the desired level by transferring power to or from the AC ports.

(2) Inter-Cluster Balancing (ICB) Control Distributes the power of the M3C among all its clusters, determining the imposition of internal command signals for the CMV and the circulating currents, without affecting the AC ports. However, the ICB should generate minimal circulating currents to increase the efficiency and power density of the converter.

(3) Low-frequency Oscillations (LFO) Mitigation Mitigates large oscillations in SM capacitor voltages by injecting CMV and circulating currents with high harmonic. It is required only at the critical points of operation, when the M3C operates at a very low frequency, but most acutely when these frequencies approach or equal [16].

(4) Local-Cluster Balancing (LCB) Control Locally regulates the capacitor voltage of each SM in each cluster. It is usually implemented at the modulation stage.

Recently, nested control systems based on decoupled modelling of the M3C topology have been proposed in the literature to enable a decoupled control of input, output, and circulating currents in M3Cs [29], [54]. In this regard, the control actions of each decoupled system do not interfere with each other, which enables performing the ICB control and the LFO mitigation without affecting the external control systems. One of the most utilized decoupling mappings is the, so-called, double-$\alpha\beta 0$ transformation [12]. Based on this decoupled modelling, four independent current paths for the M3C can be established (circulating currents), and their command signals are typically determined by the ICB and LFO controllers.

Most of the ICB control strategies reported in literature define a set of specific sinusoidal components of known frequencies and phases for the circulating currents. However, the amplitudes of these components are hard to compute and optimize. For that reason, they are typically determined using open- and closed-loop strategies [11], [12], [16], [54]. For instance, in [11], [16] multiple PI controllers implemented in several synchronous reference frames are used to determine the amplitudes of the set of pre-defined sinusoidal components for the circulating currents. In [55], a branch current reallocation is proposed using a theoretical analysis to find an energy equilibrium of the M3C. Recently, a control approach based on continuous control set MPC (CCS-MPC) to obtain the optimal circulating current references in the transformed space (four independent current paths for the M3C) for a given CMV was introduced in [45]. This control strategy is formulated to perform the ICB and LFO control tasks in a unique control algorithm since it requires only one penalty cost to be adjusted. However, although this method ensures regulation of the cluster energies, the resulting branch currents could be detrimental during transients, violating the maximum rated current in each branch since the output constraints are not included in the CCS-MPC formulation. Overcurrents are a critical

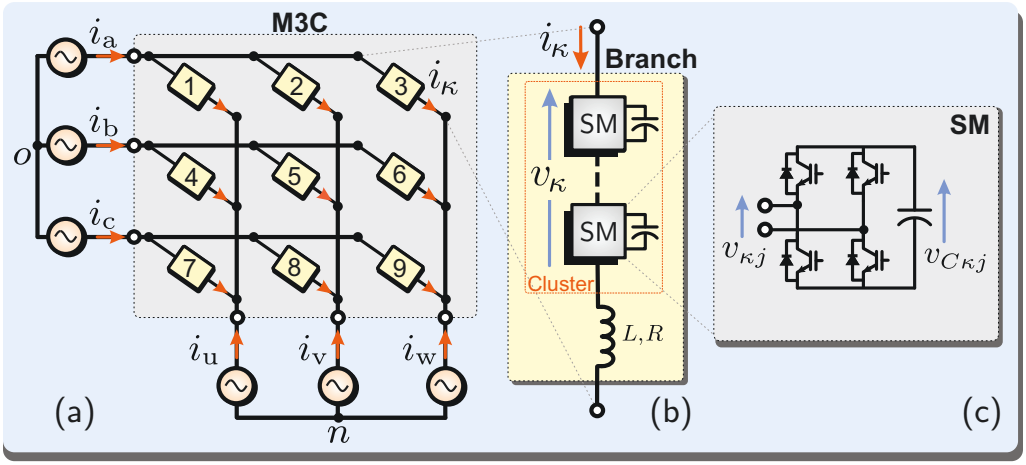

Figure 4.1: The M3C topology: (a) circuit diagram and directed graph; (b) N-cell cluster; and (c) full-bridge-based submodule.

issue for SMs, and consequently, an unconstrained MPC strategy is not suitable to achieve a safe M3C operation.

Motivated by the above mentioned concerns, this work proposes a circulating-current reference generator based on a constrained MPC to perform the ICB control task in M3Cs. The contribution and novelty of the proposal rely on the complete formulation of an optimal control problem to generate the circulating current component in every branch, leading to box-constrained quadratic programming. Furthermore, the inclusion of bound constraints on the decision variables allows for obtaining the optimal circulating currents in a computationally efficient manner, enabling the operation of the M3C even during critical frequency points and significant power steps at the output port while maintaining every cluster current within its feasible limits. Moreover, with the proposed control strategy, the safe operation of the M3C does not depend on the controller tuning since it is directly included as bound constraints in the optimal control problem.

Experimental results are provided to verify the performance and effectiveness of the proposal, showing a fast dynamic response, an effective ICB regulation for a wide frequency range, and an adequate computational burden for a single centralized multivariable controller.

4.2 The M3C

To introduce the MPC-based ICB control, the model of the M3C is firstly presented. To do so, let us consider the set of nine branches $\mathcal{K} = \{1, \ldots, 9\}$, a set of three phases (or nodes) at the input-side of the converter, $\Psi = \{\mathrm{a}, \mathrm{b}, \mathrm{c}\}$, and another set of three nodes at the output-side, $\chi = \{\mathrm{u}, \mathrm{v}, \mathrm{w}\}$. Thus, the M3C can be represented as a directed graph where each branch connects one input-port node to an output one, as illustrated in Fig. 4.1(a). The branch currents are comprised in the vector $\boldsymbol{i}_{\mathrm{s}} = \begin{bmatrix} i_1 & \cdots & i_9 \end{bmatrix}^{\mathrm{T}} \in \mathbb{R}^9$ and the input- and output-port currents are defined as $\boldsymbol{i}_{\Psi} = [i_{\mathrm{a}}\, i_{\mathrm{b}}\, i_{\mathrm{c}}]^{\mathrm{T}}$ and $\boldsymbol{i}_{\chi} = [i_{\mathrm{u}}\, i_{\mathrm{v}}\, i_{\mathrm{w}}]^{\mathrm{T}}$, respectively. On the one hand, by inspecting the circuit topology in Fig. 4.1(a), it is possible to establish the following relationship between the branch, and the input- and output-currents:

$$\begin{bmatrix} \boldsymbol{i}_\Psi \\ \boldsymbol{i}_\chi \end{bmatrix} = \underbrace{\begin{bmatrix} 1 & 1 & 1 & 0 & 0 & 0 & 0 & 0 & 0 \\ 0 & 0 & 0 & 1 & 1 & 1 & 0 & 0 & 0 \\ 0 & 0 & 0 & 0 & 0 & 0 & 1 & 1 & 1 \\ -1 & 0 & 0 & -1 & 0 & 0 & -1 & 0 & 0 \\ 0 & -1 & 0 & 0 & -1 & 0 & 0 & -1 & 0 \\ 0 & 0 & -1 & 0 & 0 & -1 & 0 & 0 & -1 \end{bmatrix}}_{:=\mathbf{A}} \boldsymbol{i}_\mathrm{s}. \tag{4.1}$$

where $\mathbf{A} \in \mathbb{R}^{6\times 9}$ is the incidence matrix of the directed graph.

By applying the standard (amplitude-invariant) Clarke transformation [56], namely $\mathbf{T}_{\alpha\beta 0}$, the input and output currents can be mapped to the $\alpha\beta 0$ space as:

$$\begin{bmatrix} \boldsymbol{i}_\Psi^{\alpha\beta 0} \\ \boldsymbol{i}_\chi^{\alpha\beta 0} \end{bmatrix} = \underbrace{\begin{bmatrix} \mathbf{T}_{\alpha\beta 0} & \mathbf{0} \\ \mathbf{0} & \mathbf{T}_{\alpha\beta 0} \end{bmatrix}}_{:=\mathbf{P}} \begin{bmatrix} \boldsymbol{i}_\Psi \\ \boldsymbol{i}_\chi \end{bmatrix} \tag{4.2}$$

Thereby, by using (4.1) and (4.2), the following linear map can be stated for the branch and external currents in the $\alpha\beta 0$ space:

$$\begin{bmatrix} \boldsymbol{i}_\Psi^{\alpha\beta 0} \\ \boldsymbol{i}_\chi^{\alpha\beta 0} \end{bmatrix} = \underbrace{\mathbf{P}\,\mathbf{A}}_{:=\mathbf{A}'_{\alpha\beta 0}} \boldsymbol{i}_\mathrm{s}. \tag{4.3}$$

In (4.3), the third and last rows establish that the zero-sequence components satisfy $i_\Psi^0 = -i_\chi^0$. Thus, the last row of matrix $\mathbf{A}'_{\alpha\beta 0} = \mathbf{PA}$ can be removed in the subsequent, and the resulting matrix is denoted as $\mathbf{A}_{\alpha\beta 0} \in \mathbb{R}^{5\times 9}$. Therefore, the input and output currents in the $\alpha\beta$ frame, i.e., $\boldsymbol{i}_\Psi^{\alpha\beta} = [i_\Psi^\alpha \;\; i_\Psi^\beta]^\mathrm{T}$ and $\boldsymbol{i}_\chi^{\alpha\beta} = [i_\chi^\alpha \;\; i_\chi^\beta]^\mathrm{T}$, and the zero-sequence current $i_0{=}i_\Psi^0$ can be expressed as:

$$\begin{bmatrix} \boldsymbol{i}_\Psi^{\alpha\beta} \\ i_0 \\ \boldsymbol{i}_\chi^{\alpha\beta} \end{bmatrix} = \mathbf{A}_{\alpha\beta 0}\, \boldsymbol{i}_\mathrm{s}. \tag{4.4}$$

On the other hand, as shown in Figs. 4.1(b)-(c), the voltage synthesized by each cluster is $v_\kappa = \sum_{j=1}^{N} u_{\kappa j} v_{C\kappa j}$, where $u_{\kappa j} \in \{-1, 0, 1\}$ and $v_{C\kappa j}$ are the switching state and the capacitor voltage of the jth SM in the kth cluster. Thus, by considering the Kirchhoff's voltage law for the nine branches, the dynamic model is expressed as:

$$\mathbf{A}^\mathrm{T} \begin{bmatrix} \boldsymbol{v}_\Psi \\ \boldsymbol{v}_\chi \end{bmatrix} = L\frac{\mathrm{d}\boldsymbol{i}_\mathrm{s}}{\mathrm{d}t} + R\boldsymbol{i}_\mathrm{s} + \boldsymbol{v}_\mathrm{s} - \mathbf{1}_{9\times 1} v_{on}, \tag{4.5}$$

where $\boldsymbol{v}_\mathrm{s} = \begin{bmatrix} v_1 & \cdots & v_9 \end{bmatrix}^\mathrm{T} \in \mathbb{R}^9$ is the cluster voltage vector, $\boldsymbol{v}_\Psi = [v_\mathrm{a} \; v_\mathrm{b} \; v_\mathrm{c}]^\mathrm{T}$ and $\boldsymbol{v}_\chi = [v_\mathrm{u} \; v_\mathrm{v} \; v_\mathrm{w}]^\mathrm{T}$ are the input- and output-voltage vectors, v_{on} is the voltage between the neutral points, and L and R are the inductance and resistance of the branch filter, respectively.

4.2.1 The circulating currents and the decoupling map

The control system proposed in this work injects a circulating current component in each cluster, namely $i_{\kappa z}$, to compensate for possible cluster energy deviations and low-frequency oscillations in the SM-capacitor voltages. These additional branch currents represent the first degrees of

freedom to deal with the ICB control and LFO mitigation tasks. Therefore, the total current in every cluster can be expressed as:

$$i_\kappa = i_{\kappa\Psi\chi} + i_{\kappa z}\,, \quad \forall \kappa \in \mathcal{K} \tag{4.6}$$

where $i_{\kappa\Psi\chi}$ is the current flowing in the branch when null circulating currents (namely basic branch current). It only depends on the external port currents. For instance, the basic current for the first branch in Fig. 4.1(a) is $i_{1\mathrm{au}} = \frac{1}{3}(i_\mathrm{a} - i_\mathrm{u})$.

Now, the additional branch currents $i_{\kappa z}$ can be grouped in the following vector:

$$\boldsymbol{i}_z = \begin{bmatrix} i_{1z} & \dots & i_{9z} \end{bmatrix}^\mathrm{T} \in \mathbb{R}^9 \tag{4.7}$$

It is worth remarking that, the additional branch currents in (4.7) must satisfy the nullspace condition, i.e., $\{\boldsymbol{i}_z \in \mathbb{R}^9 \,|\, \mathbf{A}\boldsymbol{i}_z = 0\}$, to be considered as circulating current components. Therefore, for any injected branch currents $\boldsymbol{i}_z$ satisfying the nullspace condition, the input and output currents are not affected, achieving a decoupled control of the converter. Moreover, since the nullity of incidence matrix $\mathbf{A}$ is four, only four independent internal current paths, namely circulating currents, can be established for the converter. Thus, vector $\boldsymbol{i}_z$ can be rewritten as a function of the standard circulating current vector $\boldsymbol{i}_\varepsilon = [i_{\varepsilon 1} \ \cdots \ i_{\varepsilon 4}]^\mathrm{T} \in \mathbb{R}^4$ as:

$$\boldsymbol{i}_z = \mathbf{N}\boldsymbol{i}_\varepsilon, \tag{4.8}$$

where $\mathbf{N} = [\boldsymbol{n}_1 \ \dots \boldsymbol{n}_4] \in \mathbb{R}^{9\times 4}$ is the nullspace matrix of $\mathbf{A}$. This matrix is not unique (see [29]). However, in this work, the following null space matrix is used:

$$\mathbf{N} = \begin{bmatrix} 1 & 1 & 1 & 1 \\ -1 & 0 & -1 & 0 \\ 0 & -1 & 0 & -1 \\ -1 & -1 & 0 & 0 \\ 1 & 0 & 0 & 0 \\ 0 & 1 & 0 & 0 \\ 0 & 0 & -1 & -1 \\ 0 & 0 & 1 & 0 \\ 0 & 0 & 0 & 1 \end{bmatrix}. \tag{4.9}$$

Noting that the column vectors of $\mathbf{N}$ defined in (4.9) describe the four independent current paths shown in Fig. 4.2 and every branch is affected by at least one circulating current. Moreover, from (4.8), the circulating currents $\boldsymbol{i}_\varepsilon$ can be rewritten in term of the additional branch currents $\boldsymbol{i}_z$ as:

$$\boldsymbol{i}_\varepsilon = \underbrace{\frac{1}{9}\begin{bmatrix} 1 & -2 & 1 & -2 & 4 & -2 & 1 & -2 & 1 \\ 1 & 1 & -2 & -2 & -2 & 4 & 1 & 1 & -2 \\ 1 & -2 & 1 & 1 & -2 & 1 & -2 & 4 & -2 \\ 1 & 1 & -2 & 1 & 1 & -2 & -2 & -2 & 4 \end{bmatrix}}_{:=\mathbf{N}^\dagger} \boldsymbol{i}_z \tag{4.10}$$

being $\mathbf{N}^\dagger$, the Moore–Penrose inverse of matrix $\mathbf{N}$.

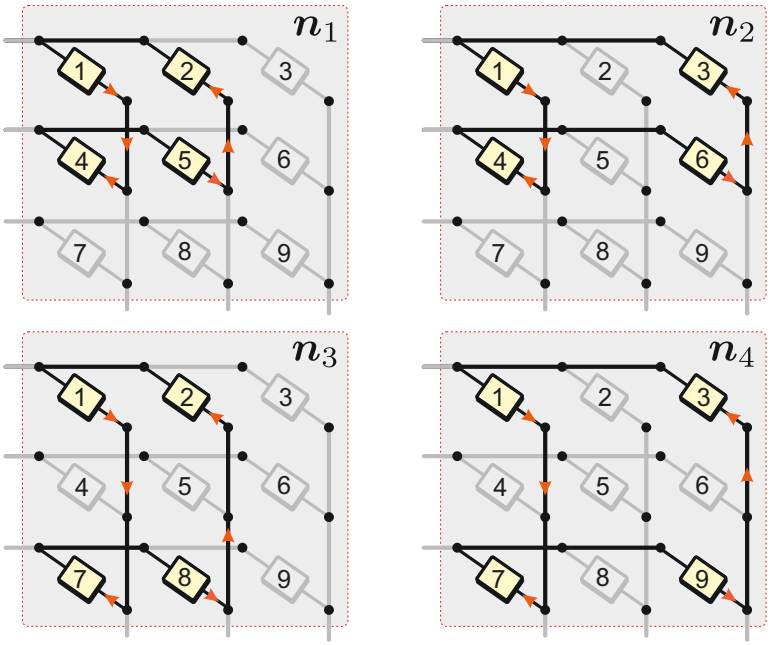

Figure 4.2: Four circulating current paths in the M3C.

For all that, the linear map $\mathbf{T} : \mathbb{R}^9 \to \mathbb{R}^9$ defined in (4.11) is used in this work to decouple the control of the input $\boldsymbol{i}_{\Psi}^{\alpha\beta}$, output $\boldsymbol{i}_{\Psi}^{\alpha\beta}$, circulating $\boldsymbol{i}_{\varepsilon}$, and zero-sequence current i_0.

$$\boldsymbol{i}'_{\mathrm{s}} = \begin{bmatrix} \boldsymbol{i}_{\Psi}^{\alpha\beta} \\ i_0 \\ \boldsymbol{i}_{\chi}^{\alpha\beta} \\ \boldsymbol{i}_{\varepsilon} \end{bmatrix} = \underbrace{\begin{bmatrix} \mathbf{A}_{\alpha\beta 0} \\ \mathbf{N}^{\dagger} \end{bmatrix}}_{:=\mathbf{T}} \boldsymbol{i}_{\mathrm{s}} \tag{4.11}$$

Therefore, a decoupled model for the input, output, and circulating currents is obtained by applying the linear map $\mathbf{T}$ to (4.5). This model together with the decoupling mapping $\mathbf{T}$ are presented in detail in the Appendix.

4.2.2 Energy–Circulating–Current Model of the M3C

To deal with the ICB control, the cluster energy $E_{C\kappa}$ is used as the variable to be controlled. From the circuit diagram shown in Fig. 4.1(b), the κth cluster energy can be expressed as $E_{C\kappa} = \frac{1}{2}C\sum_{j=1}^{N} v_{C\kappa j}^2$, where C is the average SM's capacitance. By introducing the cluster energy vector, i.e.,

$$\mathbf{E}_C = \begin{bmatrix} E_{C1} & \dots & E_{C9} \end{bmatrix}^{\mathrm{T}} \in \mathbb{R}^9, \tag{4.12}$$

the following dynamic model can be stated:

$$\frac{\mathrm{d}}{\mathrm{d}t}\mathbf{E}_C = \begin{bmatrix} \mathrm{diag}\{\boldsymbol{v}_{\mathrm{s}}\} \end{bmatrix} \boldsymbol{i}_{\mathrm{s}}. \tag{4.13}$$

It is worth remarking that, each capacitor should be regulated to the same average voltage V_C^* for the proper operation of the M3C. Therefore, the ICB condition can be achieved by directly controlling the average value of every component of $\mathbf{E}_C$ to the desired value $E_C^* = \frac{1}{2}CNV_C^{*2}$.

To explicitly model the influence of the circulating currents $\boldsymbol{i}_{\varepsilon}$ on the cluster energy vector, the decoupling transformation is applied to (4.13). Moreover, by neglecting the filter voltage drop

in (4.5), the continuous-time model for the cluster energy in the transformed space, $\mathbf{E}'_C = \mathbf{T}\,\mathbf{E}_C$, can be expressed by:

$$\frac{\mathrm{d}}{\mathrm{d}t}\mathbf{E}'_C = \underbrace{\mathbf{T}\,\mathbf{V}_\mathrm{s}\mathbf{T}^{-1}}_{:=\mathbf{V}'_\mathrm{s}}\,\boldsymbol{i}'_\mathrm{s} \tag{4.14}$$

where $\mathbf{V}_\mathrm{s}$ is a 9×9 diagonal matrix defined as:

$$\mathbf{V}_\mathrm{s} = \mathrm{diag}\left\{\mathbf{A}^\mathrm{T}\mathbf{P}^{-1}\begin{bmatrix}\boldsymbol{v}_\Psi^{\alpha\beta 0}\\ \boldsymbol{v}_\chi^{\alpha\beta 0}\end{bmatrix} + \mathbf{1}_{9\times 1}v_{on}\right\} \tag{4.15}$$

The ICB condition is fulfilled when the transformed cluster energy vector operates at the following point:

$$\mathbf{E}'^{*}_C = \mathbf{T}E^*_C\mathbf{1}_{9\times 1} = \begin{bmatrix}0 & 0 & 3E^*_C & 0 & 0 & 0 & 0 & 0 & 0\end{bmatrix}^\mathrm{T} \tag{4.16}$$

In (4.16), the third component in $\mathbf{E}'^{*}_C$ is related to the total stored energy in the capacitors of the M3C. Moreover, from the third row in (4.14), the dynamic model of E_{C0} is given by:

$$\frac{\mathrm{d}}{\mathrm{d}t}E_{C0} = \frac{1}{2}\left(v^\alpha_\Psi i^\alpha_\Psi + v^\beta_\Psi i^\beta_\Psi\right) + \frac{1}{2}\left(v^\alpha_\chi i^\alpha_\chi + v^\beta_\chi i^\beta_\chi\right) + \frac{1}{3}v_{\mathrm{s}0}i_0. \tag{4.17}$$

As shown in (4.17), E_{C0} depends on the total power flowing into the converter but not on the circulating currents. Hence, E_{C0} can be regulated by the TEB controller. Consequently, from the ICB control point of view, the remaining eight components in $\mathbf{E}'_C$ are the variables to be controlled. They are comprised in the imbalance vector $\Delta\mathbf{E}'_C \in \mathbb{R}^8$, and the ICB condition is now fulfilled when $\Delta\mathbf{E}'_C \to 0$.

Thus, by eliminating the third row in $\mathbf{V}'_\mathrm{s} = \mathbf{T}\,\mathbf{V}_\mathrm{s}\mathbf{T}^{-1}$, and denoting the resulting matrix as $\mathbf{V}_{\Psi\chi\varepsilon} \in \mathbb{R}^{8\times 9}$, the dynamic energy model (4.14) can be explicitly rewritten in terms of the circulating current vector $\boldsymbol{i}_\varepsilon$ as:

$$\frac{\mathrm{d}}{\mathrm{d}t}\Delta\mathbf{E}'_C = \mathbf{V}_{\Psi\chi}\begin{bmatrix}\boldsymbol{i}_\Psi^{\alpha\beta}\\ i_0\\ \boldsymbol{i}_\chi^{\alpha\beta}\end{bmatrix} + \mathbf{V}_\varepsilon\boldsymbol{i}_\varepsilon, \tag{4.18}$$

where $\mathbf{V}_{\Psi\chi} \in \mathbb{R}^{8\times 5}$ and $\mathbf{V}_\varepsilon \in \mathbb{R}^{8\times 4}$ are the submatrices in $\mathbf{V}_{\Psi\chi\varepsilon} = \begin{bmatrix}\mathbf{V}_{\Psi\chi} & \mathbf{V}_\varepsilon\end{bmatrix}$. They are defined in details in the Appendix.

4.3 Proposed MPC-based ICB control

The energy–circulating-current model shown in (4.18) represents a time-varying system in which the circulating currents $\boldsymbol{i}_\varepsilon$ can be considered as the control action. The time-varying matrix $\mathbf{V}_z$ depends on the input- and output-voltages and also on the injected CMV $v_{\mathrm{s}0}$ [see (4.35),(4.36) at the Appendix]. Hence, the energy–circulating-current model (4.18) is a highly coupled dynamical system since each circulating current component affects more than one element of $\Delta\mathbf{E}'_C$, making difficult to design a suitable control strategy to balance the energy among all clusters. In addition, the number of circulating currents is smaller than the number of variables to be controlled. Therefore, from a control point of view, the system described by (4.18) represents a very challenging dynamic system.

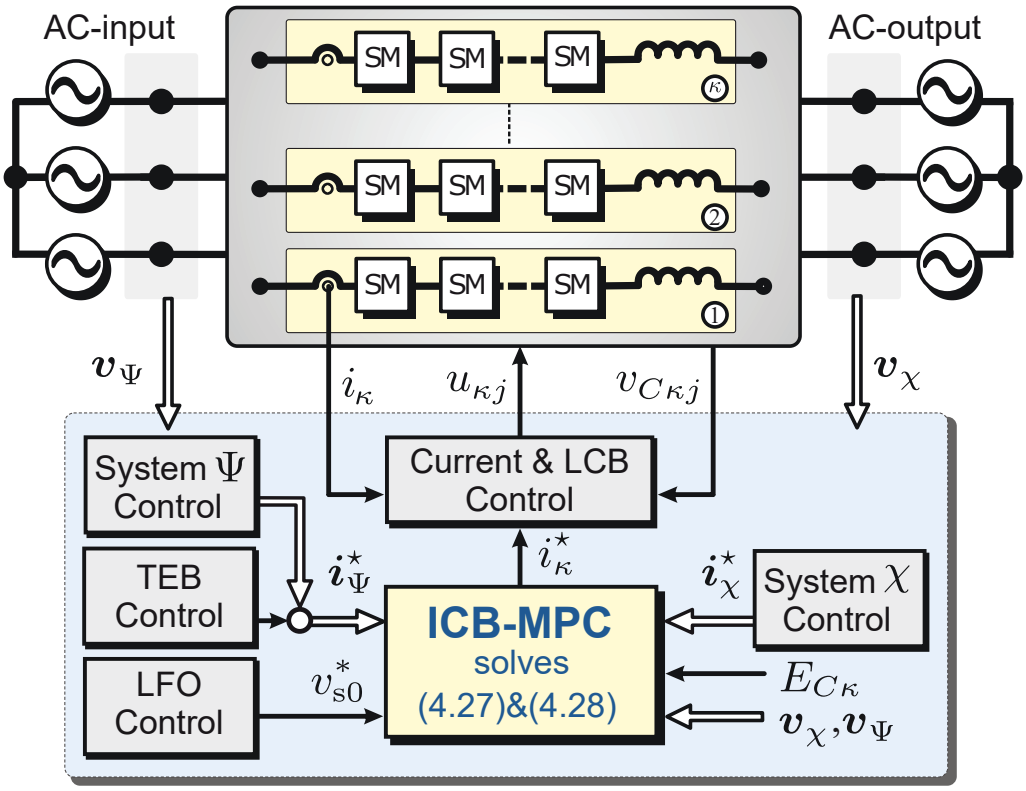

Figure 4.3: Overall control scheme.

4.3.1 MPC formulation for online reference generator

To introduce the proposed MPC-based ICB control, a discrete-time version of (4.18) is determined first. Thus, by using the Forward Euler method with a sampling period T_s, the following discrete-time model is obtained:

$$\Delta\mathbf{E}'_C(k{+}1) = \boldsymbol{b}(k) + \boldsymbol{B}(k)\boldsymbol{i}_\varepsilon(k), \tag{4.19}$$

where $\boldsymbol{B}(k) = T_s\mathbf{V}_\varepsilon(k)$ and $\boldsymbol{b}(k) = \Delta\mathbf{E}'_C(k) + T_s\boldsymbol{p}_{\Psi\chi 0}(k)$, being

$$\boldsymbol{p}_{\Psi\chi 0}(k) = \mathbf{V}_{\Psi\chi}(k)\begin{bmatrix}\boldsymbol{i}^{\alpha\beta}_\Psi(k)\\ i_0(k)\\ \boldsymbol{i}^{\alpha\beta}_\chi(k)\end{bmatrix}. \tag{4.20}$$

In contrast to the controller introduced in [45], in this work, the optimal control problem underlying the ICB controller is stated to directly compute the additional branch currents $\boldsymbol{i}_z{\in}\mathbb{R}^9$ introduced in (4.7). To do so, the circulating current vector $\boldsymbol{i}_\varepsilon{\in}\mathbb{R}^4$ is replaced in (4.19) by $\boldsymbol{i}_z$, using (4.10). Therefore, to determine the optimal circulating current components in each branch $\boldsymbol{i}^\star_z$, the following constrained optimal control problem is proposed in this work:

$$\min_{\boldsymbol{i}_z}\ J = \left\|\Delta\mathbf{E}'_C(k{+}1)\right\|^2_{\boldsymbol{Q}} + \lambda_z\left\|\boldsymbol{i}_z(k)\right\|^2_2 \tag{4.21a}$$

$$\text{s.t.}\ \ \Delta\mathbf{E}'_C(k{+}1) = \boldsymbol{b}(k) + \boldsymbol{B}(k)\mathbf{N}^\dagger\boldsymbol{i}_z(k) \tag{4.21b}$$

$$I_{\mathrm{L}\kappa}(k) \le i_{\kappa z}(k) \le I_{\mathrm{U}\kappa}(k) \quad \forall\kappa\in\mathcal{K} \tag{4.21c}$$

where $I_{\mathrm{L}\kappa}(k)$ and $I_{\mathrm{U}\kappa}(k)$ are the lower and upper bound for the circulating current component in the κth cluster, respectively. These are time-varying limits since they depend on the command

signals for the input and output currents, i.e., $i^{\star}_{\Psi}$ and $i^{\star}_{\chi}$, respectively, and also on the tolerable branch over-current limit, namely $I_{\max}$. Consequently, according to (4.6), the upper and lower bounds for the κth circulating current component $i_{\kappa z}$ are computed from:

$$-I_{\max} \leq i^{\star}_{\kappa\Psi\chi} + i_{\kappa z} \leq I_{\max} \tag{4.22}$$

Therefore, the upper and lower bounds utilized by the controller are computed by:

$$\begin{cases} I_{\mathrm{U}\kappa}(k) & = I_{\max} - \frac{1}{3}\big(i^{\star}_{\Psi}(k) - i^{\star}_{\chi}(k)\big) \\ I_{\mathrm{L}\kappa}(k) & = -I_{\max} - \frac{1}{3}\big(i^{\star}_{\Psi}(k) - i^{\star}_{\chi}(k)\big) \end{cases} \tag{4.23}$$

where $i^{\star}_{\Psi}$ and $i^{\star}_{\chi}$ are the input and output current references on the κth cluster. They are determined by the high-level control systems and the TEB controller, as illustrated in Fig. 4.3.

The cost function presented in (4.21a) penalizes the predicted tracking error weighted by the diagonal matrix $\boldsymbol{Q} = \mathrm{diag}\{q_1, \cdots, q_8\}$, and the control effort, which in this case are the circulating current components in each cluster $i_{\kappa z}$. Therefore, the non-negative scalar $\lambda_z > 0$ is a tuning parameter that adjusts the trade-off between the tracking accuracy and the control effort. The latter is proportional to the power losses produced by the circulating currents and must be reduced as much as possible.

It is worth remarking that certain components in $\boldsymbol{b}(k)$ and $\boldsymbol{B}(k)$ in (4.19) rely on the CMV (see matrices $\mathbf{V}_{\Psi\chi}$ and $\mathbf{V}_{\varepsilon}$ in the Appendix). Thus, the proposed ICB controller can incorporate a specified CMV reference, denoted as $v^{\star}_{\mathrm{s}0}$, into the discrete-time model, allowing for the use of any CMV generator in combination with the proposed ICB controller.

4.3.2 Box-constrained optimal control problem

Based on (4.22), the bound constraints in (4.21c) can be compactly rewritten as:

$$\boldsymbol{I}_{\mathrm{L}}(k) \leq \boldsymbol{i}_z \leq \boldsymbol{I}_{\mathrm{U}}(k) \tag{4.24}$$

where the upper and lower current vector are defined as

$$\boldsymbol{I}_{\mathrm{U}}(k) = [I_{\mathrm{U}1}(k)\ I_{\mathrm{U}2}(k)\ \ldots\ I_{\mathrm{U}9}(k)]^{\mathrm{T}} \tag{4.25}$$

$$\boldsymbol{I}_{\mathrm{L}}(k) = [I_{\mathrm{L}1}(k)\ \ I_{\mathrm{L}2}(k)\ \ldots\ I_{\mathrm{L}9}(k)]^{\mathrm{T}} \tag{4.26}$$

Therefore, if we define $\mathbf{G}(k) = \mathbf{B}(k)\mathbf{N}^{\dagger} \in \mathbb{R}^{8\times 9}$, the optimal circulating current components can be obtained by solving the following constrained optimal control problem:

$$\boldsymbol{i}^{\star}_z = \arg\min_{\boldsymbol{i}_z}\Big\{\big\|\mathbf{G}(k)\boldsymbol{i}_z + \boldsymbol{b}(k)\big\|^2_{\boldsymbol{Q}} + \lambda_z\big\|\boldsymbol{i}_z\big\|^2_2\Big\} \tag{4.27a}$$

$$\text{s.t.}\ \ \boldsymbol{I}_{\mathrm{L}}(k) \leq \boldsymbol{i}_z \leq \boldsymbol{I}_{\mathrm{U}}(k) \tag{4.27b}$$

This problem is known as a box-constrained quadratic programming (QP), which involves minimizing a quadratic cost function subject to bounds on the decision variables. One key property of this problem is that the Hessian matrix associated with the cost function in (4.27a), i.e., $\mathbf{H} = \mathbf{G}^{\mathrm{T}}\mathbf{Q}\mathbf{G} + \lambda_z\mathbf{I}$ is symmetric positive definite for any $\lambda_z > 0$, which guarantees the existence of a unique solution.

To efficiently solve the optimal control problem introduced in (4.27), various iterative algorithms have been proposed in the literature [57], [58]. In this work, we adopt an exterior point active

Table 4.1: System Parameters for Experimental Results.

Parameter	Value
Line-to-line Input voltage, V_g	190 V
Input grid frequency, f_Ψ	60 Hz
Branch over-current limit, $I_{\max}$	15A
Output resistance, R_L	14 Ω
Output inductance, L_L	1 mH
SMs per clusters, N	4
SM capacitance, C	987 μF
SM's Nominal DC voltage, V_{dc}	100 V
Cluster filter resistance, R	0.1 Ω
Cluster filter inductance, L	5 mH
PS-PWM carrier frequency, f_{cr}	2 kHz

set method based on a Lagrangian function and the Karush-Kuhn-Tucker (KKT) conditions. This approach has been shown to be effective for solving box-constrained QP problems. For further details on the algorithm used in our work, we refer readers to [47].

Once the optimal circulating current components are determined by solving (4.27), the current reference for each branch is finally computed as:

$$i_\kappa^\star = i_{\kappa\Psi\chi}^\star + i_{\kappa z}^\star\,, \quad \forall \kappa \in \mathcal{K} \tag{4.28}$$

It is worth to emphasize that the solution provided by MPC-based ICB controller does not impose pre-define harmonic components on the circulating currents. However, it computes instantaneous circulating currents to minimize the (weighted) magnitude of the energy imbalance vector, i.e., $\|\Delta\mathbf{E}'_C\|_{\boldsymbol{Q}}$.

In contrast to [45], where the weighting factor associated with the control action must be carefully tuned to obtain feasible circulating current references, the proposed ICB controller can determine the circulating current references by explicitly considering the available current in each converter branch as bound constraints in the problem formulation, enabling the ICB controller to be an effective and safe circulating current generator. Hence, with the proposed controller, the inner controllers always receive feasible branch current references $i_\kappa^\star$ for any $\lambda_z > 0$.

The overall control scheme is illustrated in Fig. 4.3. As shown, the external control systems provide the input and output current references to fulfill the requirements of a specific application. Additionally, in the outer loops, the TEB controller defines an active current component (from the input port) required to balance the overall M3C's energy. The circulating current references and the CMV to be injected are determined by the ICB and LFO controllers, respectively. Finally, once the cluster current references are computed using (4.28), the inner control loop performs both the LCB control and regulates the branch currents of the M3C.

4.4 Experimental Results

Experimental results have been performed to analyze and verify the proposed strategy performance when governing an M3C prototype with 4 SMs in each branch (36 SMs in total)

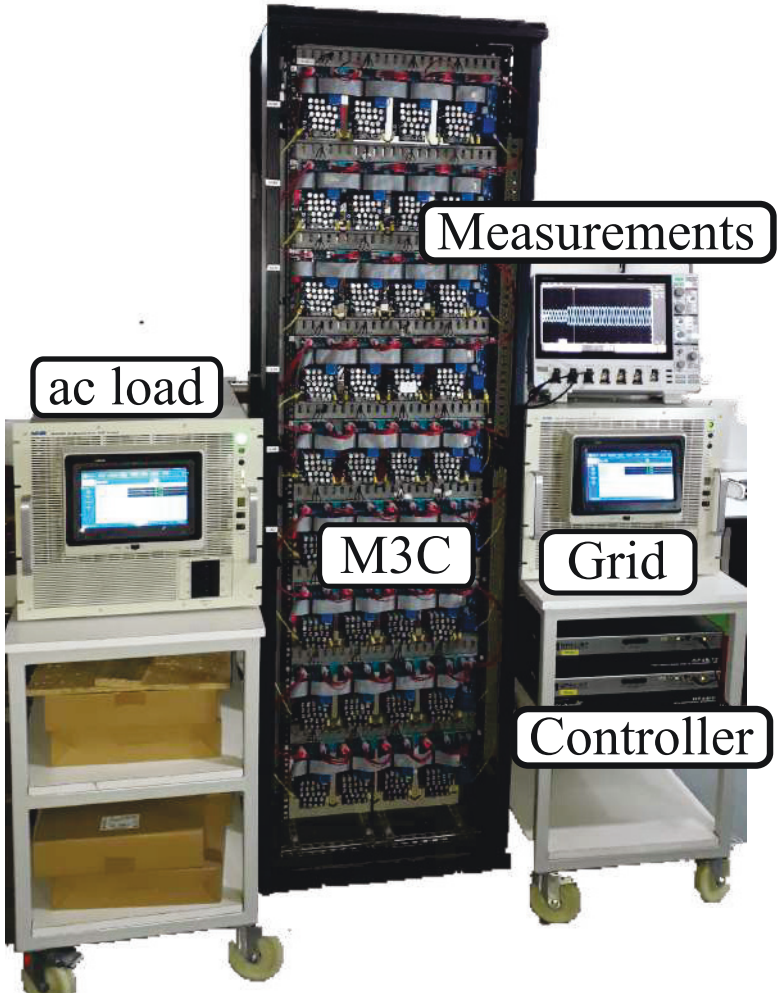

Figure 4.4: Experimental setup with a downscale M3C prototype of 36 SMs.

connected to a three-phase system and a passive load, as shown in Fig. 4.4. The grid-voltage was generated by a regenerative grid-simulator (NHR9410) and the passive load was implemented by a regenerative ac load (NHR9430). The setup parameters are summarized in Table 4.1. The predictive control scheme was implemented on an OPAL-RT OP4510 as well as the box-constrained algorithm with $\lambda_z = 0.2$.

Variable Output Frequency Performance

In this test, the input frequency is fixed at 60 Hz, and the output power is set at 3 kW and 500 VAr. In contrast, the output frequency presents the following pattern. Initially, it is fixed at 1 Hz for 3.3 seconds to increase suddenly to 50 Hz, a frequency at which it is also maintained for 3.3 seconds. Finally, another step in the output frequency takes it to 60Hz, bringing the system to the equal-frequency mode, which is one of the most challenging operating points of this MMC topology.

The experimental close-loop results considering variable output frequencies are depicted in Fig. 4.5. In this figure, on the one hand, the capacitor voltages are plotted directly from the data obtained from ADCs. On the other hand, the input, output and branch current (i_{a}, i_{u}, and i_{au}, respectively), as well as the cluster voltage v_{au}, and the injected CMV v_{s0}, are registered directly from the oscilloscope, showing a close-up during each subinterval.

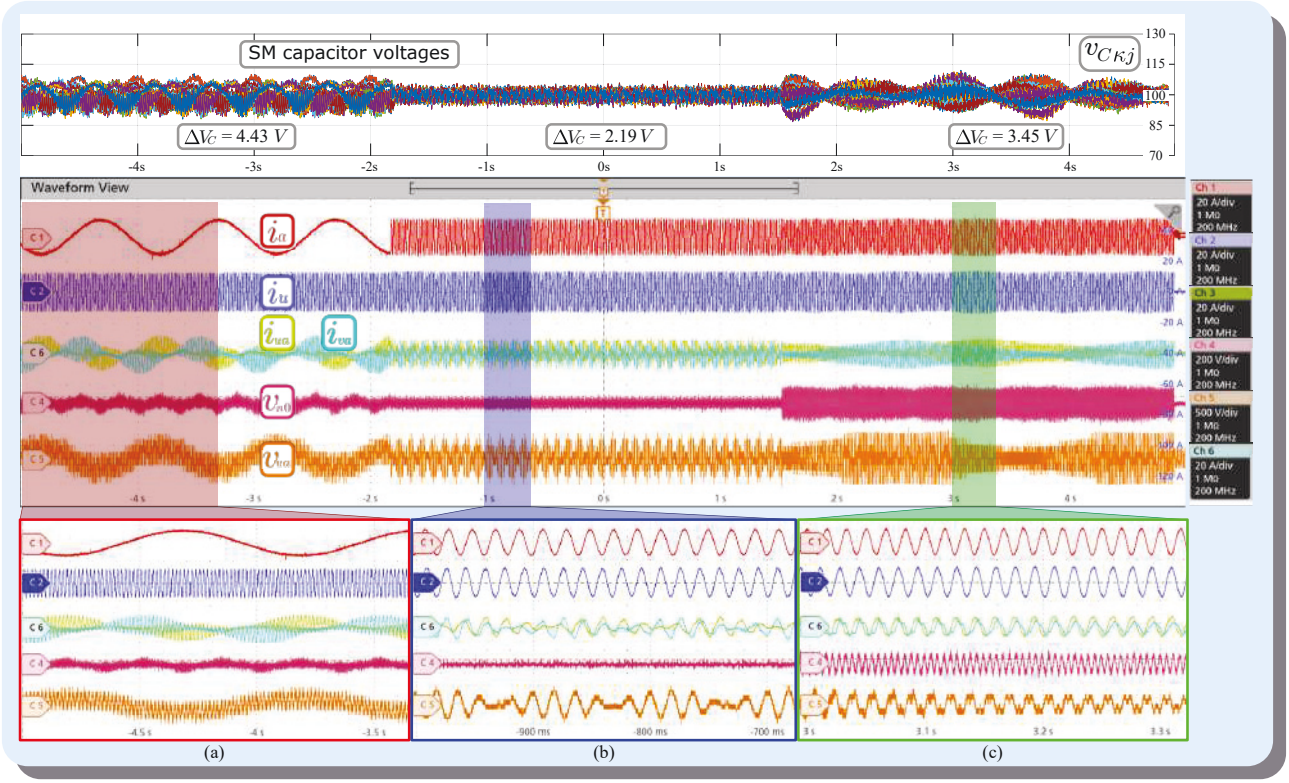

Figure 4.5: Experimental performance for the variable-frequency test. Output frequency at 1 Hz (a), 50 Hz (b), and 60 Hz (c). Top graph: capacitor voltages. Bottom graphs (oscilloscope waveforms): i_u (Ch 1), i_a (Ch 2), i_{au} (Ch 3), v_{s0} (Ch 4), v_{ua} (Ch 5), and i_{av} (Ch 6).

In the first and second intervals (i.e., 1 Hz and 50 Hz at the output) it is not necessary to apply CMV, which represents a great advantage of the method since it only requires the limited injection of CMV during equal frequency mode. As shown in the Ch4 of Fig. 4.5(c), the injected CMV is a sinusoidal signal 50 Vrms at 180 Hz. However, any CMV generator which ensure mitigation during equal frequency mode can be used. Moreover, as depicted in Fig. 4.5, the input, output, and branch currents, as well as capacitor voltages are controlled at 100 V, even when operating at critical operating points (low frequency at the output or equal frequency mode). The waveform of each of the signals shown in Fig. 4.5 allows checking the performance of the reference generation over the entire frequency range.

Furthermore, to evaluate the steady-state performance, the root mean squared error of the capacitor voltages, denoted as ΔV_C, is explicitly added in Fig. 4.5 for the three frequencies tested ($\Delta V_C = \{4.43, 2.19, 3.45\}$). These values are obtained by computing the average of the squared errors of all SM capacitor voltages during one second, i.e.,

$$\Delta V_C = \frac{1}{9N} \sum_{\kappa=1}^{9} \sum_{j=1}^{N} \sqrt{\frac{1}{N_P} \sum_{k=1}^{N_p} (v_{C\kappa j}(k) - V_C^*)^2} \tag{4.29}$$

where the number of sampled data in one second is $N_p = 1/T_s = 16,000$.

The capacitor voltage fluctuations presented in Fig. 4.5 achieve a maximum voltage deviation of 14%. These oscillations occur when the M3C operates near or in the critical points (0 or 60 Hz), which are expected to be higher than those when it works far from the critical points. Multiple factors impact the capacitor voltages' oscillations, such as capacitance, CMV, and

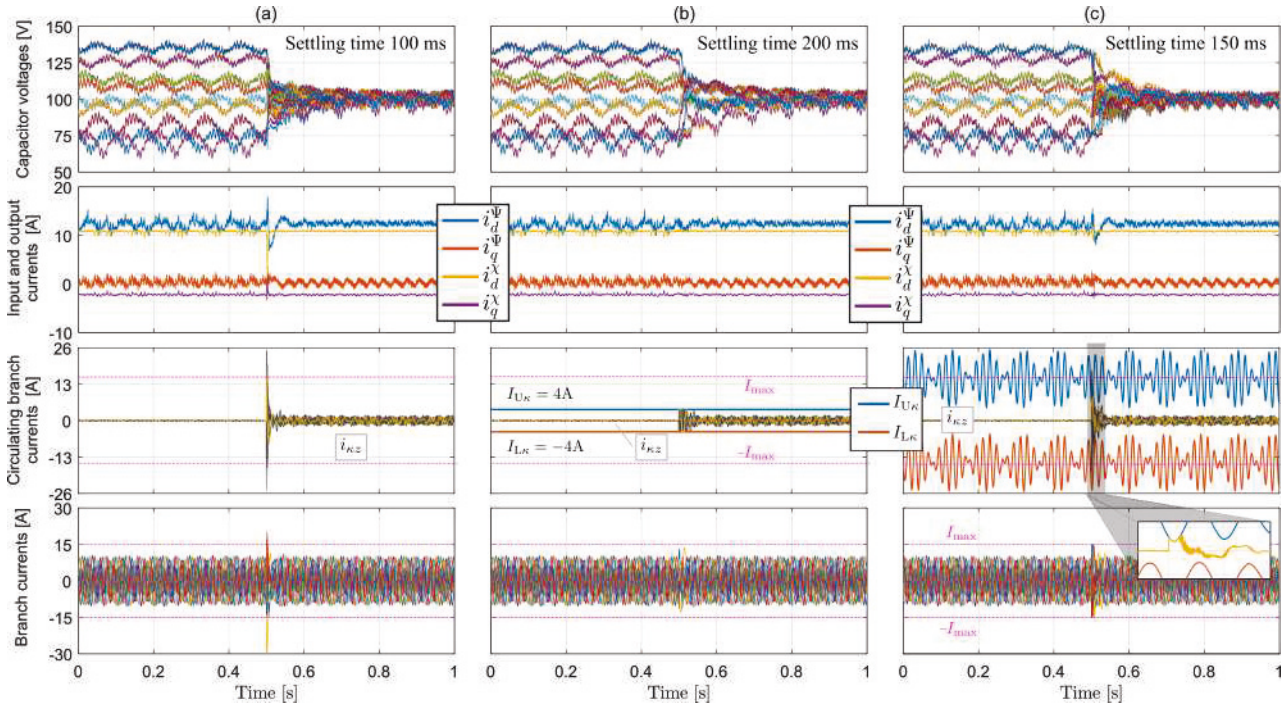

Figure 4.6: Experimental results under imbalance cluster energies: (a) performance of the reference generator introduced in [45], and performance of the proposed ICB-MPC with static (b) and dynamic (c) upper and lower bounds for $i^{\star}_{\kappa z}$.

input and output frequencies, among others. The CMV is also fundamental for mitigation when the M3C operates at a critical point. Therefore, an alternative CMV generator would mitigate the capacitor voltage fluctuations differently under acute conditions. Nevertheless, both the impact of these voltage fluctuations on the capacitor's life span and the generation of optimal CMV are out of the scope of this work.

Cluster Imbalance Control

This section will discuss the dynamic behaviour of the controlled system under a scenario of cluster energy imbalance. The voltage at the input port is set to 190 V at 60 Hz; meanwhile, the output operates at 200V and 50 Hz with 3 kW and 500 VAr. No CMV is required.

Moreover, the performance of the proposed MPC-based circulating current references generator is compared to the one introduced in [45]. In this regard, three experiments were performed in the downscale converter prototype initially operating unbalanced around ±30% of the nominal voltage value. For the sake of a fair comparison, the controllers weighting factors are adjusted to obtain the same closed-loop dynamic response.

The results obtained from this experiment are shown in Fig. 4.6. On the one hand, the performance of the reference generator introduced in [45] is shown in Fig. 4.6(a). As shown, after 500 ms with the unbalance in the capacitor voltages, the generation of circulating current references in the transformed space, i.e., $\boldsymbol{i}^{\star}_{\varepsilon}$, is activated to perform the ICB control, reaching the balance operating condition shortly but injecting branch currents over the current limit, set as 15A. In this case, the branch currents reach a peak value of 30A (corresponding to an overcurrent of 100%). In addition, the input and output currents are highly impacted by the activation of the ICB controller, as shown in the second row of Fig. 4.6(a).

On the other hand, the proposed MPC-based ICB controller, which explicitly includes the current limits into the underlying optimal control problem to determine the branch circulating current components $\boldsymbol{i}_z$, is implemented considering two options for the upper and lower bounds of the circulating branch currents. The first one establishes a fixed or static current limit of 4A for the circulating branch currents amplitude. As shown in Fig. 4.6(b), despite the inter-cluster energy balance being reached 100 ms later than the previous test, the maximum current for the circulating branch currents is certainly limited to the established value during the transient.

Finally, in order to use the entire current margin between the current needed to supply the load and the tolerable branch over-current limit of the SMs, namely $I_{\max} = 15$A, a test is performed by using the upper and lower bounds introduced in (4.23). The experimental result in Fig. 4.6(c) shows that the dynamic response of the capacitor voltages is similar to the one obtained with the controller introduced in [45]. However, branch currents during the transient always fulfill the over-current limit. Also, during the activation of the proposed reference generator at instant 500 ms, the input and output currents are not affected as much as the first case (Fig. 4.6(a)) and the settling time is between (a) and (b).

It is important to mention that in [45], the circulating current reference might be unfeasible (physically unfeasible) for inner controllers due to the optimization does not consider any restriction. Nevertheless, the design of the proposed ICB-MPC considers suitable upper and lower restrictions, avoiding unfeasible current references. Hence, the inner controllers always receive feasible current references. The experimental results show the proposed controller outperforms the one introduced in [45].

Notice that the upper and lower bounds in (4.23) allow to limit the branch current to 15A while balance the cluster energies Fig. 4.6(c). Meanwhile, the converter operates in a sub-optimal condition during the transient if fixed bounds are apply to the circulating currents Fig. 4.6(b), cause does not use all the available branch current to balance the cluster energies. Finally, if no constraints are apply, the converter operates with branch currents over the desire limits (15A) Fig. 4.6(a).

Power Step Change

Finally, a step-change from 2 kW to 3 kW in the active power reference is performed. This test sets the input and output frequencies to 60 Hz and 50 Hz, respectively. The experimental close-loop result is shown in Fig. 4.7. Here, the upper and lower bounds for the circulating current components vary after the active power step-changed is applied at 300 ms, reducing the margin to inject circulating currents in the branches. This behaviour is expected since the basic branch current increases as the active power increase [see (4.6)]. Furthermore, as shown in Fig. 4.7(c) and (d), neither the circulating branch current component nor the branch currents saturate at any time.

Scalability Analysis of the proposed ICB-MPC

To analyse the scalability of the proposed circulating current reference generator, the floating point operations per second (FLOPS) required to obtain the unconstrained optimal solution of the proposed optimal control problem (4.27) is presented first. In this regard, the unconstrained solution is given by:

$$\boldsymbol{i}_z^{\mathrm{uc}}(k) = -\mathbf{H}^{-1}(k)\mathbf{F}(k) \tag{4.30}$$

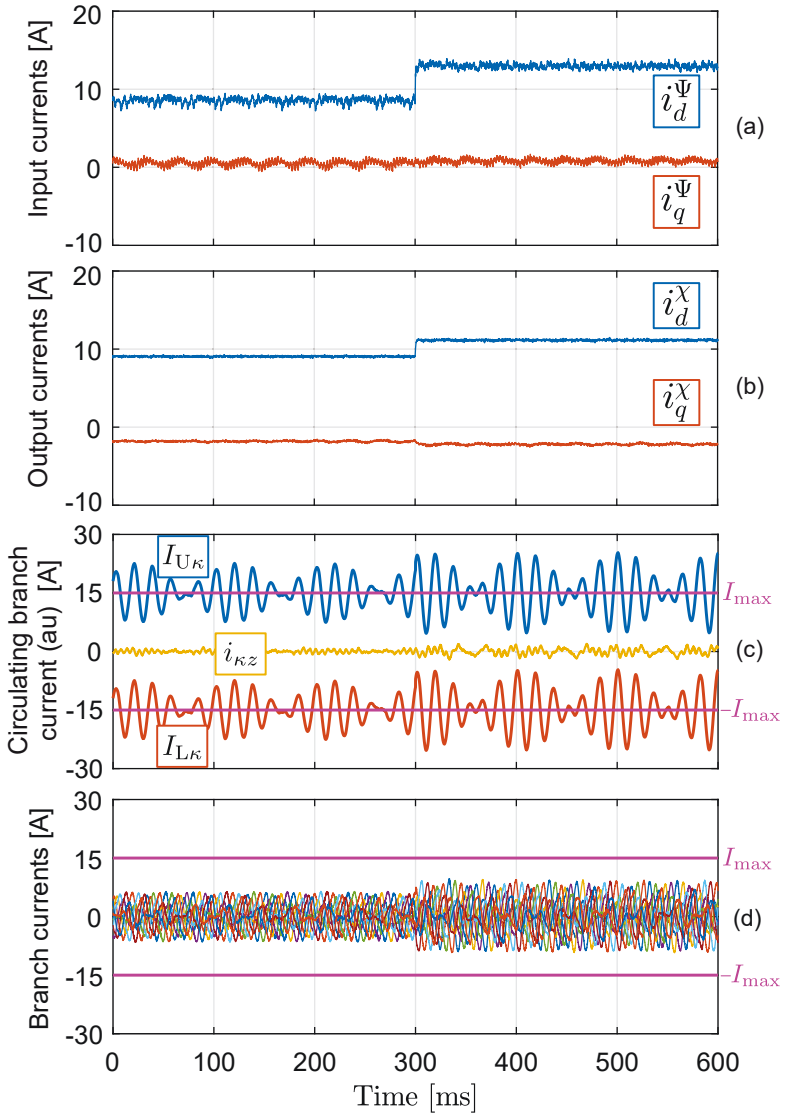

Figure 4.7: Power step performance: input (a) and output (b) currents in rotating dq frames, circulating branch current with their bounds (c), and the total branch currents (d).

with

$$\begin{aligned} \mathbf{H}(k) &= \mathbf{G}(k)^T \boldsymbol{Q} \mathbf{G}(k) + \lambda_z \mathbf{I}_9 \\ \mathbf{F}(k) &= \mathbf{G}(k)^T \boldsymbol{Q} \boldsymbol{b}(k) \end{aligned} \tag{4.31}$$

The matrices in (4.30) and (4.31) have fixed dimensions and do not depend on the number of SMs. Thus, the FLOPS required to compute the matrix operations in (4.30) and (4.31) is 4516.

Nevertheless, the dependency of the FLOPS on the number of SMs lies in the calculation of the total energy of each cluster $E_{C\kappa} = \frac{1}{2} C \sum_{j=1}^{N} v_{C\kappa j}^2$, whose expression requires $2N$ FLOPS per cluster.

Therefore, the total FLOPS required to obtain the unconstrained optimal solution (4.30) can be expressed by:

$$\mathrm{FLOPS} = \frac{(4516 + 18N)}{T_s}. \tag{4.32}$$

In addition, the processing time was measured experimentally to address the influence of the

exterior point active set algorithm on the computational burden. The experimental execution time of the proposed ICB-MPC in the OPAL-RT OP4510 has an average value of 1.54 μs, with a minimum of 1.5 μs (for steady-steady when the limits are not violated and the unconstrained solution provide the optimal one), and a maximum value of 2.22 μs. This maximum processing time considers the time required by the exterior point active set method to solve the proposed box-constrained QP in (4.27) and occurs for transients when limits are reached. Thus, considering (4.32) with N = 4 cells, the control approach requires approximately 108 MFLOPS ($2.22/1.5 \cdot 73408000$ FLOPS) for the downscale converter prototype depicted in Fig. 4.4.

The OPAL-RT OP4510 is is equipped with an Intel Xeon Processor E3-1565L v5. With four cores, this processor is capable of executing 89.6 GFLOPS. Based on this estimation, the proposed ICB-MPC can handle approximately 209000 cells with a sampling frequency of 16 kHz. However, it is important to note that this calculation does not take into account the computational burden of the inner control loop, which means that the maximum number of SMs will be lower than 209000.

4.5 Conclusions

This chapter presents a constrained MPC strategy to perform the inter-cluster balancing control task for modular multilevel matrix converters. In addition, this chapter comprehensively derives an energy-circulating-currents model using a decoupling mapping based on the nullspace of the converter topology's incidence matrix. Based on this model, a constrained optimal control problem is formulated, where the inclusion of current constraints as bounds on the decision variables allows obtaining the optimal circulating currents in a computationally efficient manner. As a result, the proposed reference generator effectively balances the energy among all the clusters of the converter while maintaining every branch current within its feasible limits, even during severe imbalance levels and also for steady-state challenging operating conditions, such as equal-frequency mode.

The proposed MPC-based ICB controller has been experimentally validated using a M3C prototype of 36 SMs. The presented results show that the proposed control scheme outperforms a similar MPC controller recently introduced in the literature, making it possible to take full advantage of the circulating currents injection. At the same time, the safe operation of the M3C is guaranteed with the proposed control strategy since it does not depend on the controller tuning. Future work may consider the stability analysis of the proposed MPC-based ICB controller.

Appendix

The decoupling mapping presented in (4.11) is defined as:

$$\mathbf{T} = \frac{1}{9}\begin{bmatrix} 6 & 6 & 6 & -3 & -3 & -3 & -3 & -3 & -3 \\ 0 & 0 & 0 & 3\sqrt{3} & 3\sqrt{3} & 3\sqrt{3} & -3\sqrt{3} & -3\sqrt{3} & -3\sqrt{3} \\ 3 & 3 & 3 & 3 & 3 & 3 & 3 & 3 & 3 \\ -6 & 3 & 3 & -6 & 3 & 3 & -6 & 3 & 3 \\ 0 & -3\sqrt{3} & 3\sqrt{3} & 0 & -3\sqrt{3} & 3\sqrt{3} & 0 & -3\sqrt{3} & 3\sqrt{3} \\ 1 & -2 & 1 & -2 & 4 & -2 & 1 & -2 & 1 \\ 1 & 1 & -2 & -2 & -2 & 4 & 1 & 1 & -2 \\ 1 & -2 & 1 & 1 & -2 & 1 & -2 & 4 & -2 \\ 1 & 1 & -2 & 1 & 1 & -2 & -2 & -2 & 4 \end{bmatrix} \tag{4.33}$$

The decoupled model is:

$$L\frac{\mathrm{d}}{\mathrm{d}t}\boldsymbol{i}_{\Psi}^{\alpha\beta} + R\boldsymbol{i}_{\Psi}^{\alpha\beta} = -\boldsymbol{v}_{\mathrm{s}\Psi} + 3\boldsymbol{v}_{\Psi}^{\alpha\beta} \tag{4.34a}$$

$$L\frac{\mathrm{d}}{\mathrm{d}t}i_0 + Ri_0 = -v_{\mathrm{s}0} + 3v_{\Psi 0} - 3v_{\chi 0} + 3v_{on} \tag{4.34b}$$

$$L\frac{\mathrm{d}}{\mathrm{d}t}\boldsymbol{i}_{\chi}^{\alpha\beta} + R\boldsymbol{i}_{\chi}^{\alpha\beta} = -\boldsymbol{v}_{\mathrm{s}\chi} + 3\boldsymbol{v}_{\chi}^{\alpha\beta} \tag{4.34c}$$

$$L\frac{\mathrm{d}}{\mathrm{d}t}\boldsymbol{i}_{\varepsilon} + R\boldsymbol{i}_{\varepsilon} = -\boldsymbol{v}_{\mathrm{s}\varepsilon} \tag{4.34d}$$

where $\boldsymbol{v}_{\mathrm{s}\Psi} = \begin{bmatrix} v_{\mathrm{s}\Psi}^{\alpha} & v_{\mathrm{s}\Psi}^{\beta} \end{bmatrix}^{\mathrm{T}}$ and $\boldsymbol{v}_{\mathrm{s}\chi} = \begin{bmatrix} v_{\mathrm{s}\chi}^{\alpha} & v_{\mathrm{s}\chi}^{\beta} \end{bmatrix}^{\mathrm{T}}$ are the input and output cluster voltage in the $\alpha\beta$ frame, $\boldsymbol{v}_{\mathrm{s}\varepsilon} = \begin{bmatrix} v_{\varepsilon 1} & v_{\varepsilon 2} & v_{\varepsilon 3} & v_{\varepsilon 4} \end{bmatrix}^{\mathrm{T}}$ is the internal (circulating) cluster voltage, and $v_{\mathrm{s}0} = \frac{1}{3}\sum_{\kappa\in\mathcal{K}} v_{\mathrm{s}\kappa}$ is the CMV imposed by the cluster. These cluster voltage vectors are determined using $\boldsymbol{v}_{\mathrm{s}}' = \mathbf{T}\boldsymbol{v}_{\mathrm{s}}$.

As shown in (4.34), the transformed cluster voltages $\boldsymbol{v}_{\mathrm{s}\Psi}$, $\boldsymbol{v}_{\mathrm{s}\chi}$, and $\boldsymbol{v}_{\mathrm{s}\varepsilon}$ only impacts on the input $\boldsymbol{i}_{\Psi}^{\alpha\beta}$, output $\boldsymbol{i}_{\chi}^{\alpha\beta}$, and circulating currents $\boldsymbol{i}_{\varepsilon}$, respectively; achieving therefore a decoupled model. The system is only coupled at the zero-sequence components, as described in (4.34b).

Finally, the matrices involved in the energy-circulating-current model presented in (4.18) are defined as:

$$\mathbf{V}_{\Psi\chi} = \frac{1}{12}\begin{bmatrix} 4v_{\mathrm{s}0} + 6v_{\Psi}^{\alpha} & -6v_{\Psi}^{\beta} & 12v_{\Psi}^{\alpha} & 0 & 0 \\ -6v_{\Psi}^{\beta} & 4v_{\mathrm{s}0} - 6v_{\Psi}^{\alpha} & 12v_{\Psi}^{\beta} & 0 & 0 \\ 0 & 0 & 12v_{\chi}^{\alpha} & 4v_{\mathrm{s}0} - 6v_{\chi}^{\alpha} & 6v_{\chi}^{\beta} \\ 0 & 0 & 12v_{\chi}^{\beta} & 6v_{\chi}^{\beta} & 4v_{\mathrm{s}0} + 6v_{\chi}^{\alpha} \\ -v_{\chi}^{\alpha} + \sqrt{3}v_{\chi}^{\beta} & \sqrt{3}v_{\chi}^{\alpha} - 3v_{\chi}^{\beta} & 0 & -v_{\Psi}^{\alpha} + \sqrt{3}v_{\Psi}^{\beta} & \sqrt{3}v_{\Psi}^{\alpha} - 3v_{\Psi}^{\beta} \\ -v_{\chi}^{\alpha} - \sqrt{3}v_{\chi}^{\beta} & \sqrt{3}v_{\chi}^{\alpha} + 3v_{\chi}^{\beta} & 0 & -v_{\Psi}^{\alpha} + \sqrt{3}v_{\Psi}^{\beta} & -\sqrt{3}v_{\Psi}^{\alpha} + 3v_{\Psi}^{\beta} \\ -v_{\chi}^{\alpha} + \sqrt{3}v_{\chi}^{\beta} & -\sqrt{3}v_{\chi}^{\alpha} + 3v_{\chi}^{\beta} & 0 & -v_{\Psi}^{\alpha} - \sqrt{3}v_{\Psi}^{\beta} & \sqrt{3}v_{\Psi}^{\alpha} + 3v_{\Psi}^{\beta} \\ -v_{\chi}^{\alpha} - \sqrt{3}v_{\chi}^{\beta} & -\sqrt{3}v_{\chi}^{\alpha} - 3v_{\chi}^{\beta} & 0 & -v_{\Psi}^{\alpha} - \sqrt{3}v_{\Psi}^{\beta} & -\sqrt{3}v_{\Psi}^{\alpha} - 3v_{\Psi}^{\beta} \end{bmatrix} \tag{4.35}$$

$$\mathbf{V}_{\varepsilon} = \frac{1}{6}\begin{bmatrix} -9v_{\chi}^{\alpha} + 3\sqrt{3}v_{\chi}^{\beta} & -9v_{\chi}^{\alpha} - 3\sqrt{3}v_{\chi}^{\beta} \\ 3\sqrt{3}v_{\chi}^{\alpha} - 3v_{\chi}^{\beta} & 3\sqrt{3}v_{\chi}^{\alpha} + 3v_{\chi}^{\beta} \\ -9v_{\Psi}^{\alpha} + 3\sqrt{3}v_{\Psi}^{\beta} & -9v_{\Psi}^{\alpha} - 3\sqrt{3}v_{\Psi}^{\beta} \\ 3\sqrt{3}v_{\Psi}^{\alpha} - 3v_{\Psi}^{\beta} & -3\sqrt{3}v_{\Psi}^{\alpha} + 3v_{\Psi}^{\beta} \\ 2v_{\mathrm{s}0} + 2\sqrt{3}v_{\Psi}^{\beta} - 2\sqrt{3}v_{\chi}^{\beta} & -3v_{\chi}^{\alpha} - \sqrt{3}v_{\chi}^{\beta} \\ -3v_{\chi}^{\alpha} + \sqrt{3}v_{\chi}^{\beta} & 2v_{\mathrm{s}0} + 2\sqrt{3}v_{\Psi}^{\beta} + 2\sqrt{3}v_{\chi}^{\beta} \\ 3v_{\Psi}^{\alpha} - \sqrt{3}v_{\Psi}^{\beta} & 0 \\ 0 & 3v_{\Psi}^{\alpha} - \sqrt{3}v_{\Psi}^{\beta} \\ -9v_{\chi}^{\alpha} + 3\sqrt{3}v_{\chi}^{\beta} & -9v_{\chi}^{\alpha} - 3\sqrt{3}v_{\chi}^{\beta} \\ -3\sqrt{3}v_{\chi}^{\alpha} + 3v_{\chi}^{\beta} & -3\sqrt{3}v_{\chi}^{\alpha} - 3v_{\chi}^{\beta} \\ -9v_{\Psi}^{\alpha} + 3\sqrt{3}v_{\Psi}^{\beta} & -9v_{\Psi}^{\alpha} - 3\sqrt{3}v_{\Psi}^{\beta} \\ 3\sqrt{3}v_{\Psi}^{\alpha} + 3v_{\Psi}^{\beta} & -3\sqrt{3}v_{\Psi}^{\alpha} - 3v_{\Psi}^{\beta} \\ 3v_{\Psi}^{\alpha} + \sqrt{3}v_{\Psi}^{\beta} & 0 \\ 0 & 3v_{\Psi}^{\alpha} + \sqrt{3}v_{\Psi}^{\beta} \\ 2v_{\mathrm{s}0} - 2\sqrt{3}v_{\Psi}^{\beta} - 2\sqrt{3}v_{\chi}^{\beta} & -3v_{\chi}^{\alpha} - \sqrt{3}v_{\chi}^{\beta} \\ -3v_{\chi}^{\alpha} + \sqrt{3}v_{\chi}^{\beta} & 2v_{\mathrm{s}0} - 2\sqrt{3}v_{\Psi}^{\beta} + 2\sqrt{3}v_{\chi}^{\beta} \end{bmatrix} \tag{4.36}$$

Chapter 5

AN IMPROVED REFERENCE GENERATOR BASED ON MPC OF CIRCULATING CURRENTS AND COMMON-MODE VOLTAGE FOR MODULAR MULTILEVEL MATRIX CONVERTERS

5.1 Introduction

Modular multilevel converters are the next generation for medium/high voltage and high power applications [35], [43], [59]. Among them, the leading exponents for ac to ac power conversion are the back-to-back modular multilevel converter (B2B-M2C), the modular multilevel matrix converter (M3C) and the Hexverter (HxC) [10]. These converters can be used for critical ac-ac applications such as low-frequency ac (LFAC) transmission systems, wind power conversion systems (WECS), power system interconnections (60-50 Hz) [10], fault-tolerant applications [60] and medium/high voltage motor drives for pumps, mills, conveyors, marine propulsion, among other applications [32].

The M3Cs present advantages for high-power and low-frequency applications compared to the B2B-M2C and the HxC [25]. Compared with B2B-M2Cs, the M3Cs converts directly from ac to ac, requiring fewer sub-modules (SMs) [13], and have obtained a better performance for low-frequency operations such as LFAC transmission systems, WECS and low-speed motor drives [10]. Compared with the HxC, the M3Cs have been proved to be more suitable in terms of semiconductor ratings and control flexibility for different and equal frequency mode [14]. Additionally, unlike HxC, the reactive power of both ac-ports are independent.

Nonetheless, B2B-M2Cs, HxCs and M3Cs have technical challenges for their use, for instance, highly coupled internal states, complex control and balance of several floating capacitors, a large number of control signals, and capacitor voltage oscillations at critical frequencies [16],

[17].

The M3C has four control targets: the currents of both ac-ports; the circulating currents; and the capacitor voltages of each sub-module. The regulation of the capacitor voltages considers four control balancing strategies:
i) *Total Energy Balancing (TEB):* regulates the energy stored in all capacitors to the desired level by transferring power to or from the AC ports.
ii) *Inter-Cluster Balancing (ICB):* distributes the power of the M2C among all its clusters, determining the imposition of internal command signals for the common mode voltage and the circulating currents, without affecting the external ports. The ICB should generate minimal circulating currents and common-mode voltage (CMV) to maintain the efficiency and power density of the converter.
iii) *Low-frequency Oscillations Mitigation (LFOM):* compensates large oscillations in SM capacitor voltages by injecting CMV and circulating currents with high harmonic components. It is required only at the critical points of operation, when the M3C operates at a very low frequency, but most acutely when these frequencies approach or equal [16].
iv) *Local-Cluster Balancing (LCB):* regulates the SM's capacitor voltage in each cluster, using phase-shifted pulse-width modulation (PS-PWM) with proportional controllers or level-shifted PWM (LS-PWM) and nearest level modulation (NLM) with sorting algorithms [38].

The literature has proposed nested control schemes based on decoupled M3C models, which allow decoupled control of input, output and circulating currents [61]. This decoupled control strategy allows ICB and LFOM to be performed without interfering with external control ports. This decoupled model establishes four circulating currents for the M3C and their references are generally determined by the ICB and LFOM control strategies.

Most ICB control strategies reported in the literature define a set of predefined sinusoidal components of fixed frequencies and phases for the circulating currents. The amplitudes of these components are then determined using open and closed loop strategies [11], [12], [16]. For example, the work [11] uses multiple PI controllers implemented in synchronous reference frames to determine the amplitudes of the set of predefined sinusoidal components for the circulating currents. One of the most utilized decoupling mappings is the, so-called, double-$\alpha\beta 0$ transformation [12]. In [16], the amplitudes of the sinusoidal components are obtained in a transformed frame, using the standard transformation double-$\alpha\beta 0$ and then the $\Sigma\Delta$ transformation, which allows to isolate specific frequencies for circulating currents.

Recently [45] introduced a control approach based on continuous control ensemble MPC (CCS-MPC) to obtain the optimal circulating current references in the transformed space (four independent current paths for the M3C) for a given CMV. This control strategy performs the ICB and LFOM in a unique control algorithm, since it requires only one penalty cost to be adjusted. However, although this method ensures regulation of the cluster energies, the resulting branch currents could be detrimental during transients, violating the maximum rated current in each branch since the output constraints are not included in the CCS-MPC formulation. Over-currents are a critical issue for SMs, and consequently, an unconstrained MPC strategy is not suitable to achieve a safe M3C operation. This issue is solved in [46], where the cluster energies are obtained in the transformed space. However, the circulating currents are kept in the original framework, which allows for the limitation of the circulating currents in the optimal problem by considering the maximum cluster current, always obtaining feasible cluster currents. Nonetheless, none of these works have considered the CMV generation in their proposals.

The contribution and novelty of this work is that the circulating currents and CMV refer-

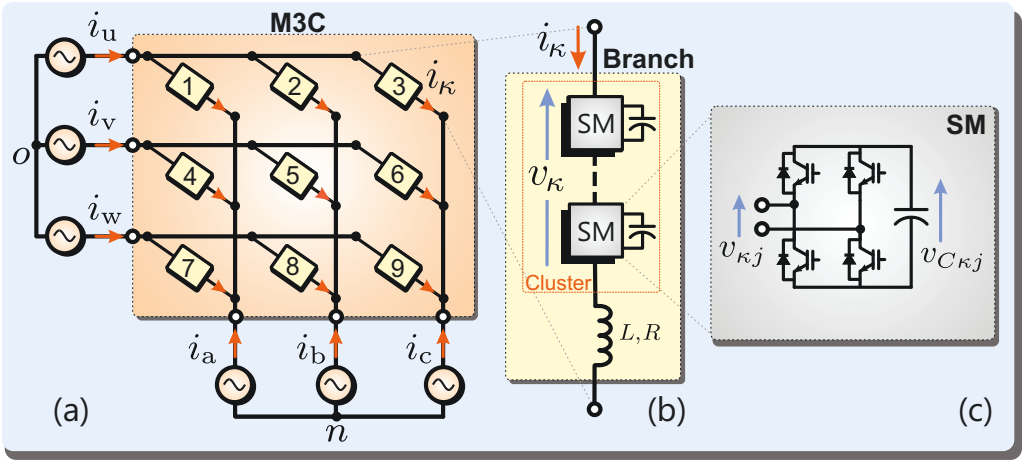

Figure 5.1: The M3C topology: (a) circuit diagram and directed graph; (b) N-cell cluster; and (c) full-bridge-based sub-module.

ences are generated optimally with the aim of performing the ICB and the LFOM jointly. The proposed reference generator, based on MPC, considers the coupling of circulating currents and CMV, obtaining optimal references for the circulating currents and the CMV. Compared with state-of-the-art reference generators, this proposal improves the performance of the M3C, especially in balancing and mitigating low-frequency oscillation in the capacitor voltages. Additionally, the MPC structure includes constraints for CMV and circulating currents, allowing the operation of the M3C under a safe operation range of currents and voltages independent of the inner current controller. Moreover, the proposal is designed in the original framework, achieving a transformer-less reference generator for the M3C. The main contributions of this work are the following: i) optimal circulating current and CMV reference generator; ii) consideration of the coupling among circulating currents and CMV; iii) wide output frequency operation for the M3C, including the critical points; and iv) design in the original framework.

Experimental results are provided to verify the proposal performance and effectiveness, showing a fast dynamic response, fixed harmonic spectrum, an effective ICB and LFOM regulation for a wide frequency range, and a suitable computational burden operating with a single centralized controller.

5.2 Modular Multilevel Matrix Converter Model

The M3C topology is composed of nine stacks or clusters to interconnect two three-phase ac-ports (Fig. 5.1). Each cluster is formed by connecting several H-bridges cells or sub-modules in cascade manner along with a series cluster inductor. Each sub-module has a floating capacitor in its dc-port.

To introduce the MPC-based ICB control, the model of the M3C is firstly presented. To do so, let us consider the set of nine branches $\mathcal{K} = \{1, \ldots, 9\}$, a set of three phases (or nodes) at the input-side of the converter, $\Psi = \{\mathrm{u}, \mathrm{v}, \mathrm{w}\}$, and another set of three nodes at the output-side, $\chi = \{\mathrm{a}, \mathrm{b}, \mathrm{c}\}$. The branch currents are comprised in the vector $\boldsymbol{i}_{\mathrm{s}} = \begin{bmatrix} i_1 & \cdots & i_9 \end{bmatrix}^{\mathrm{T}} \in \mathbb{R}^9$ and the input- and output-port currents are defined as $\boldsymbol{i}_{\Psi} = [i_{\mathrm{u}}\, i_{\mathrm{v}}\, i_{\mathrm{w}}]^{\mathrm{T}}$ and $\boldsymbol{i}_{\chi} = [i_{\mathrm{a}}\, i_{\mathrm{b}}\, i_{\mathrm{c}}]^{\mathrm{T}}$, respectively.

On the one hand, by inspecting the circuit topology in Fig. 5.1(a), it is possible to establish

the following relationship between the branch, and the input- and output-currents:

$$\begin{bmatrix} \boldsymbol{i}_\Psi \\ \boldsymbol{i}_\chi \end{bmatrix} = \underbrace{\begin{bmatrix} 1 & 1 & 1 & 0 & 0 & 0 & 0 & 0 & 0 \\ 0 & 0 & 0 & 1 & 1 & 1 & 0 & 0 & 0 \\ 0 & 0 & 0 & 0 & 0 & 0 & 1 & 1 & 1 \\ -1 & 0 & 0 & -1 & 0 & 0 & -1 & 0 & 0 \\ 0 & -1 & 0 & 0 & -1 & 0 & 0 & -1 & 0 \\ 0 & 0 & -1 & 0 & 0 & -1 & 0 & 0 & -1 \end{bmatrix}}_{:=\mathbf{A}} \boldsymbol{i}_\mathrm{s}. \tag{5.1}$$

where $\mathbf{A} \in \mathbb{R}^{6\times 9}$ is the incidence matrix of the directed graph.

On the other hand, as shown in Figs. 5.1(b)-(c), the voltage synthesized by each cluster is $v_\kappa = \sum_{j=1}^{N} u_{\kappa j} v_{C\kappa j}$, where $u_{\kappa j} \in \{-1, 0, 1\}$ and $v_{C\kappa j}$ are the switching state and the capacitor voltage of the jth SM in the kth cluster. Thus, by considering the Kirchhoff's voltage law for the nine branches, the dynamic model is expressed as:

$$\mathbf{A}^\mathrm{T} \begin{bmatrix} \boldsymbol{v}_\Psi \\ \boldsymbol{v}_\chi \end{bmatrix} = L\frac{\mathrm{d}\boldsymbol{i}_\mathrm{s}}{\mathrm{d}t} + R\boldsymbol{i}_\mathrm{s} + \boldsymbol{v}_\mathrm{s} - \mathbf{1}_{9\times 1} v_{on}, \tag{5.2}$$

where $\boldsymbol{v}_\mathrm{s} = \begin{bmatrix} v_1 & \cdots & v_9 \end{bmatrix}^\mathrm{T} \in \mathbb{R}^9$ is the cluster voltage vector, $\boldsymbol{v}_\Psi = [v_\mathrm{u}\ v_\mathrm{v}\ v_\mathrm{w}]^\mathrm{T}$ and $\boldsymbol{v}_\chi = [v_\mathrm{a}\ v_\mathrm{b}\ v_\mathrm{c}]^\mathrm{T}$ are the input- and output-voltage vectors, v_{on} is the voltage between the neutral points, and L and R are the inductance and resistance of the branch filter, respectively.

In (5.2), the cluster current vector can be expressed as [46]:

$$\boldsymbol{i}_\mathrm{s} = \boldsymbol{i}_\mathrm{B} + \boldsymbol{i}_z \tag{5.3}$$

where $\boldsymbol{i}_\mathrm{B} \in \mathbb{R}^9$ is the basic branch current vector which depends on the external currents. Thus, it is determined from (5.1) by using the Moore–Penrose inverse of the incidence matrix as:

$$\boldsymbol{i}_\mathrm{B} = \mathbf{A}^\dagger \begin{bmatrix} \boldsymbol{i}_\Psi^\mathrm{T} & \boldsymbol{i}_\chi^\mathrm{T} \end{bmatrix}^\mathrm{T}. \tag{5.4}$$

Also, $\boldsymbol{i}_z \in \mathbb{R}^9$ is the injected circulating current vector to compensate for possible cluster energy deviations and low-frequency oscillations in the SM-capacitor voltages. These additional branch currents represent the first degrees of freedom to control the cluster energies in the M3C. It is worth remarking that, this additional branch currents must satisfy the nullspace condition, i.e., $\boldsymbol{i}_z \in \mathbb{R}^9 \,|\, \mathbf{A}\boldsymbol{i}_z = 0$, to be considered as circulating current components. Therefore, for any injected branch currents $\boldsymbol{i}_z$ satisfying the nullspace condition, the input and output currents are not affected, achieving a decoupled control of the M3C.

5.3 Proposed MPC-Based Reference Generator

The overall control scheme is illustrated in Fig. 5.2. As shown, the external control systems provide the input and output current references $\boldsymbol{i}_\Psi^\star$ and $\boldsymbol{i}_\chi^\star$ to fulfill the requirements of a specific application. Additionally, in the outer loops, the TEB controller defines an active current component (from the input port) required to regulate the overall M3C's energy. The circulating current references and the CMV to be injected are determined by the proposed MPC-based ICB and LFOM control strategy. The innermost stage determines the switching states $u_{\kappa j}$ aiming to control the cluster current vector $\boldsymbol{i}_\mathrm{s}$ and to perform the LCB control to locally regulate each SM's capacitor voltage in every cluster. To this end, the PS-MPC strategy presented in [62] is implemented in this work.

In the following, the proposed reference generator is formulated to perform the ICB and LFOM jointly by generating suitable circulating currents and CMV.

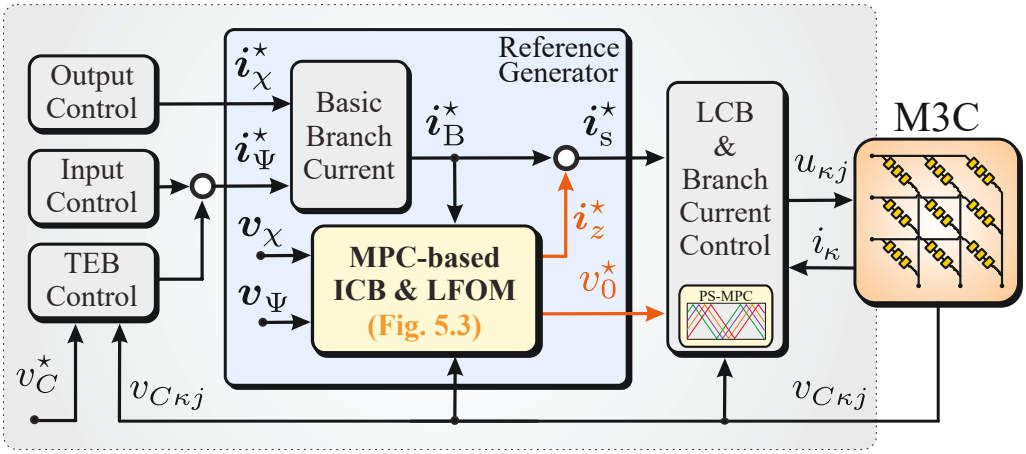

Figure 5.2: Overall control scheme.

5.3.1 Cluster Energy Model

To deal with the proposed energy control strategy, the cluster energy $E_{C\kappa}$ is used as the variable to be controlled. From the circuit diagram shown in Fig. 5.1(b), the κth cluster energy can be expressed as $E_{C\kappa} = \frac{1}{2}C\sum_{j=1}^{N} v_{C\kappa j}^2$, where C is the rated SM's capacitance. By introducing the cluster energy vector, i.e.,

$$\mathbf{E}_C = \begin{bmatrix} E_{C1} & \dots & E_{C9} \end{bmatrix}^{\mathrm{T}} \in \mathbb{R}^9, \tag{5.5}$$

and by neglecting the filter voltage drop in (5.2), the discrete-time model can be stated as:

$$\mathbf{E}_C(k{+}1) = \underbrace{\mathbf{E}_C(k) + T_s\big[\mathbf{V}(k){+}v_0(k)\mathbf{I}_9\big]\big(\boldsymbol{i}_{\mathrm{B}}(k){+}\boldsymbol{i}_z(k)\big)}_{\boldsymbol{f}_{\mathrm{NL}}(\cdot)}, \tag{5.6}$$

where $v_0(k) \in \mathbb{R}$ is the CMV to be injected by the M3C, and $\mathbf{V}(k)$ is a diagonal matrix depending on the external voltages at instant k, i.e.,

$$\mathbf{V}(k) = \mathrm{diag}\left\{ \mathbf{A}^{\mathrm{T}} \begin{bmatrix} \boldsymbol{v}_{\Psi}(k) \\ \boldsymbol{v}_{\chi}(k) \end{bmatrix} \right\} \in \mathbb{R}^{9\times 9} \tag{5.7}$$

The energy model shown in (5.6) represents a time-varying system in which the circulating currents $\boldsymbol{i}_z$ as well as the common-mode voltage v_0 can be considered as the control actions. It is a highly coupled dynamical non-linear system since each circulating current component as well as the CMV affect more than one element of the branch power vector. In addition, the number of degrees of freedom is smaller than the number of variables to be controlled. Therefore, the control of the system can be considered a very challenging problem.

5.3.2 Optimal Control Problem

To determine the optimal circulating currents $\boldsymbol{i}_z$ and the CMV v_0, the following cost function at instant k is proposed in this work:

$$J = \big\|\mathbf{E}_C(k{+}1) - \mathbf{E}_C^{\star}(k)\big\|_{\boldsymbol{Q}}^2 + \lambda_z\big\|\boldsymbol{i}_z(k)\big\|_2^2 + \lambda_0 v_0^2(k) \tag{5.8}$$

where each component in $\mathbf{E}_C^{\star}$ is computed as $E_{C\kappa}^{\star}{=}\frac{1}{2}CNv_{C\kappa}^{\star 2}$. This cost function penalizes the predicted tracking error and the control effort. As shown in (5.8), the control effort has one

component proportional to the squared sum of the circulating current components and another proportional to the squared of the CMV amplitude. The non-negative parameters λ_z and λ_0 are tuning parameters that adjust the trade-off between the tracking accuracy and the control effort. Moreover, $\boldsymbol{Q}$=diag$\{q_1, \cdots, q_9\} \in \mathbb{R}^{9\times 9}$ provides a relative weight to every component of the predicted tracking error.

Therefore, the proposed constrained optimal control problem (COCP) underlying the ICB and LFOM is stated as:

$$\min_{\boldsymbol{i}_z(k), v_0(k)} \quad J(\mathbf{E}_C(k{+}1), \boldsymbol{i}_z(k), v_0(k)) \tag{5.9a}$$

$$\text{s.t.} \quad \mathbf{E}_C(k{+}1){=}\boldsymbol{f}_{\text{NL}}(\mathbf{E}_C(k), \boldsymbol{i}_z(k), v_0(k)) \tag{5.9b}$$

$$\mathbf{A}\boldsymbol{i}_z(k) = \mathbf{0}_{6\times 1} \tag{5.9c}$$

$$\boldsymbol{I}_{\text{L}}(k) \leq \boldsymbol{i}_z(k) \leq \boldsymbol{I}_{\text{U}}(k) \tag{5.9d}$$

$$V_{\text{L}}(k) \leq v_0(k) \leq V_{\text{U}}(k) \tag{5.9e}$$

In (5.9), the decision variables are the circulating current vector and the common-mode voltage. Thus, the controller aims to minimize the cost function (5.9a) over the control inputs that satisfy the inequality constraints regarding the upper and lower bounds for the cluster currents and CMV given in (5.9d) and (5.9e), respectively. Moreover, to certainly inject circulating currents, we explicitly added the nullspace condition (5.9c) to ensure that the circulating currents in $\boldsymbol{i}_z(k)$ neither affect the input nor the output currents. Notice that the dynamic model presented in (5.9b) is a nonlinear system due to the multiplication of both control signals so the COCP presented in (5.9a) is a nonlinear programming problem (NLP).

5.3.3 Proposed Solver Approach

To face this problem, solver algorithms presented in the literature are based on assuming the CMV to be injected $v_0^\star$ as a known variable [45], [46]. In this regard, a high-frequency signal is preferred to avoid extra low-frequency components in the cluster power. As a result, the discrete-time model becomes linear and the complexity of the problem is reduced since the circulating currents become the only decision variables.

However, to address the complexities of this NLP, this work employs the iterative optimization approach shown in Fig. 5.3. This method is based on the block coordinate descent (BCD) algorithm [63] and divides the NLP presented in (5.9) into two linear subproblems. In the first subproblem, we optimize the circulating currents, assuming the CMV is a known variable. Analogously, the second subproblem optimizes the CMV while assuming the circulating currents are known. The proposed solver algorithm converges towards an optimal solution by solving both linear subproblems iteratively.

Circulating Current Subproblem

The optimal control problem for the circulating current is obtained by assuming known the CMV and taken as its previously iteration value $v_0^{(i)}$. This approach allows redefining the constraint in (5.9b) as a linear function of circulating currents, i.e.:

$$\mathbf{E}_C(k{+}1) = \mathbf{E}_C(k) + \mathbf{B}_z(k)\boldsymbol{i}_z(k) + \boldsymbol{d}_z(k) \tag{5.10}$$

where the input matrix is defined as:

$$\mathbf{B}_z(k) = T_s\big(\mathbf{V}(k){+}v_0^{(i)}\mathbf{I}_9\big) \tag{5.11}$$

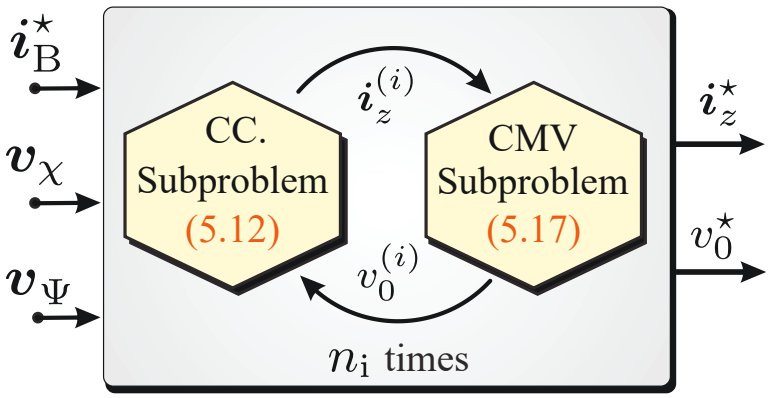

Figure 5.3: Proposed iterative optimal control problem.

and $\boldsymbol{d}_z(k) = \mathbf{B}_z(k)\boldsymbol{i}_{\mathrm{B}}(k)$ is a known disturbance.

Consequently, the COCP stated in (5.9) can be rewritten as the following convex optimization subproblem:

$$\min_{\boldsymbol{i}_z(k)} \ \left\|\mathbf{E}_C(k{+}1) - \mathbf{E}_C^\star(k)\right\|_{\boldsymbol{Q}}^2 + \lambda_z \left\|\boldsymbol{i}_z(k)\right\|_2^2 \tag{5.12a}$$

$$\text{s.t.} \ \ \mathbf{E}_C(k{+}1) = \mathbf{E}_C(k) + \mathbf{B}_z(k)\boldsymbol{i}_z(k) + \boldsymbol{d}_z(k) \tag{5.12b}$$

$$\mathbf{A}\boldsymbol{i}_z(k) = \mathbf{0}_{6\times 1} \tag{5.12c}$$

$$\boldsymbol{I}_{\mathrm{L}}(k) \leq \boldsymbol{i}_z(k) \leq \boldsymbol{I}_{\mathrm{U}}(k) \tag{5.12d}$$

As shown in (5.12), by fixing the CMV value, the CMV control effort component of the cost function is constant and can be neglected from the cost. Moreover, initially, the optimization problem is solved obtaining an initial iterative solution $\boldsymbol{i}_z^{(i)}$.

In (5.12d), $\boldsymbol{I}_{\mathrm{L}}(k)$ and $\boldsymbol{I}_{\mathrm{U}}(k)$ are the lower and upper bounds for the circulating current vector. These limits are time-varying since depend on the input and output current references, $\boldsymbol{i}_\Psi^\star$ and $\boldsymbol{i}_\chi^\star$, respectively. Additionally, the lower and upper limits depend on the branch over-current limit, $I_{\max}$. Therefore, the upper and lower limits for the cluster currents can be deduced from (5.3) as:

$$\begin{cases} \boldsymbol{I}_{\mathrm{U}}(k) & = I_{\max}\mathbf{1}_{9\times 1} - \boldsymbol{i}_{\mathrm{B}}^\star(k) \\ \boldsymbol{I}_{\mathrm{L}}(k) & = -I_{\max}\mathbf{1}_{9\times 1} - \boldsymbol{i}_{\mathrm{B}}^\star(k). \end{cases} \tag{5.13}$$

Additionally, the restriction (5.12c) ensures that the optimal solution do not impact in the input or output system. In this work, it is adopted an exterior point active set method based on a Lagrangian function and the Karush-Kuhn-Tucker (KKT) conditions.

Common-Mode Voltage Subproblem

Similarly as the previous control problem, the CMV optimal control problem redefines the energy dynamic-model (5.9b) by taken the previously obtained solution for the circulating currents $\boldsymbol{i}_z^{(i)}$ as follows:

$$\mathbf{E}_C(k{+}1){=}\mathbf{E}_C(k) + \boldsymbol{b}_0(k)v_0(k) + \boldsymbol{d}_0(k) \tag{5.14}$$

where the matrices $\boldsymbol{b}_0(k)$ and $\boldsymbol{d}_0(k)$ are defined as:

$$\boldsymbol{b}_0(k) = T_s\big(\boldsymbol{i}_z^{(i)} + \boldsymbol{i}_{\mathrm{B}}(k)\big), \tag{5.15}$$

$$\boldsymbol{d}_0(k) = T_s\mathbf{V}(k)\big(\boldsymbol{i}_z^{(i)} + \boldsymbol{i}_{\mathrm{B}}(k)\big) \tag{5.16}$$

Consequently, the COCP stated in (5.9) can be rewritten as the following convex optimization subproblem:

$$\min_{v_0(k)} \ \left\|\mathbf{E}_C(k{+}1) - \mathbf{E}_C^{\star}(k)\right\|_{\boldsymbol{Q}}^2 + \lambda_0 v_0^2(k) \tag{5.17a}$$

$$\text{s.t. } \mathbf{E}_C(k{+}1){=}\mathbf{E}_C(k) + \boldsymbol{b}_0(k)v_0(k) + \boldsymbol{d}_0(k) \tag{5.17b}$$

$$V_{\mathrm{L}}(k) \leq v_0(k) \leq V_{\mathrm{U}}(k) \tag{5.17c}$$

Notice that the CMV optimal control problem (5.17) considers the circulating currents $\boldsymbol{i}_z^{(i)}$ as a known disturbance, so the middle term of the cost function (5.8) associated to the circulating currents does not participate in this optimal problem. Finally, since $v_0 \in \mathbb{R}$, it is important to highlight that the optimal solution of this subproblem, $v_0^{(i)}$, can be obtained in each iteration as follows:

$$v_0^{(i)} = \min\big\{V_{\mathrm{U}}(k), \max\left\{V_{\mathrm{L}}(k), v_0^{\mathrm{unc}}\right\}\big\} \tag{5.18}$$

where v_0^{unc} is the unconstrained optimal problem solution:

$$v_0^{\mathrm{unc}} = -\frac{\boldsymbol{b}_0^{\mathrm{T}}(k)\boldsymbol{Q}\big(\mathbf{E}_C(k) + \boldsymbol{d}_0(k){-}\mathbf{E}_C^{\star}(k)\big)}{\boldsymbol{b}_0^{\mathrm{T}}(k)\boldsymbol{Q}\boldsymbol{b}_0(k){+}\lambda_0}. \tag{5.19}$$

5.3.4 Iterative Optimization Process

As mentioned, the original NLP has been decomposed into two simpler linear subproblems to apply the BCD algorithm. As shown in Fig. 5.3, the first one focuses on determining the optimal circulating currents for a given CMV, while the second subproblem aims to find the optimal CMV for a given circulating current. The solution to the original NLP is then approached iteratively by solving both linear subproblems sequentially. This iterative procedure is repeated for a specified number of times, denoted as n_{i}, ultimately yielding the optimal solution for both circulating currents and CMV in the nonlinear control system. Notice that n_{i} is a control parameter to tune for the control performance. On the one hand, a low value of n_{i} might lead to a sub-optimal solution for circulating currents and/or CMV. On the other hand, a high value of n_{i} leads to a high computational burden for the overall optimization problem [63]. Hence, a trade-off between the optimal solution tolerance and computational burden must be achieved when tuning n_{i}.

5.4 Experimental Results

Experimental results have been performed to analyze and verify the proposed MPC strategy performance when governing an M3C connected to a three-phase system and a passive load. The first system is composed by a grid-voltage generated using the grid-simulator NHR9410 and the second system is comprised by a passive load of the second was generated using the regenerative ac load NHR9430. The predictive control scheme was implemented on an OPAL-RT OP4510 system. The data is acquired by the OPAL-RT software every 62.5 μs and is not post-processed. The prototype is presented in Fig. 5.4 and its parameters are summarized in Table 5.1. The proposed MPC strategy was tuned heuristically with q_{κ}=1, λ_z=5×10^{-3}, λ_0=1.25×10^{-5} and $n_{\mathrm{i}} = 3$; and the execution time of the proposal with three iteration is T_e=14.55 μs.

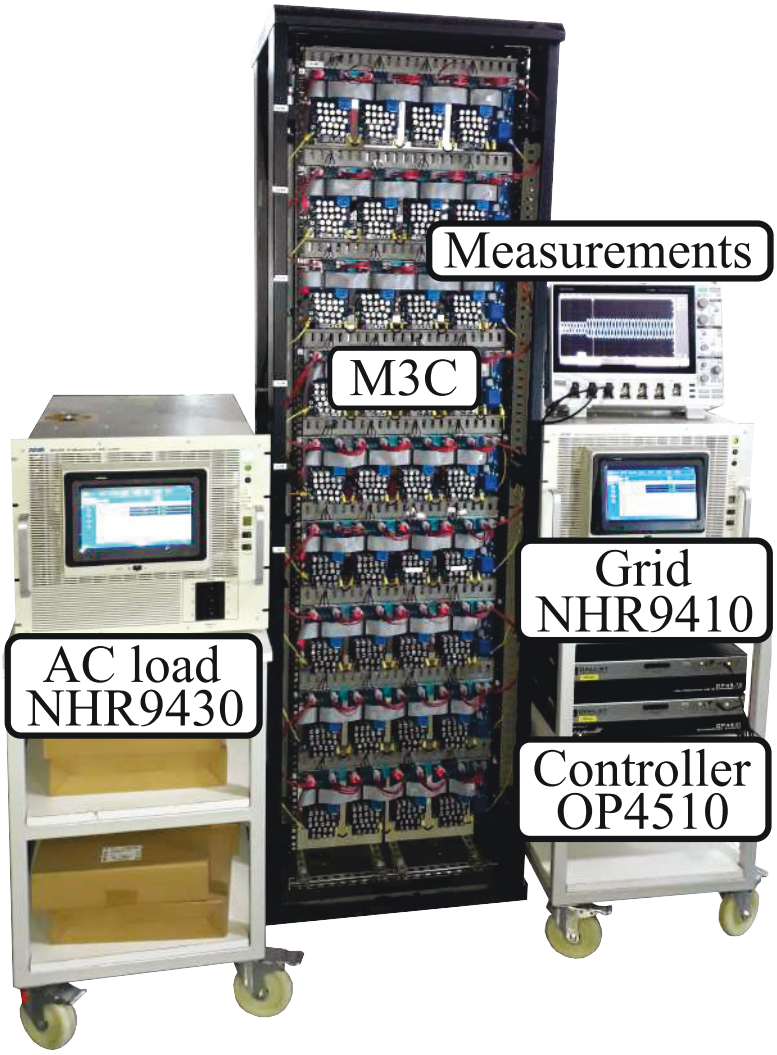

Figure 5.4: Experimental prototype of 3 kVA.

Table 5.1: System Parameters for Experimental Results.

Variable	Description	Experimental
P	Rated power	3 kW
v_Ψ	Input grid voltage (line-to-line rms)	190 V
f_Ψ	Input grid frequency	60 Hz
r_L, L_L	Output load parameters	14 Ω, 1 mH
f_χ	Output frequency	1-70 Hz
N	SMs per clusters	4
C	SM capacitance	987 μF
$v^\star_{C\kappa}$	dc cap. voltage per SM	100 V
L, R	Cluster filter parameters	5 mH, 0.1 Ω
f_{cr}	Carrier frequency	2 kHz
$I_{\max}$	Maximum cluster current	15 A
$V_{\max}$	Maximum common-mode voltage	141 V

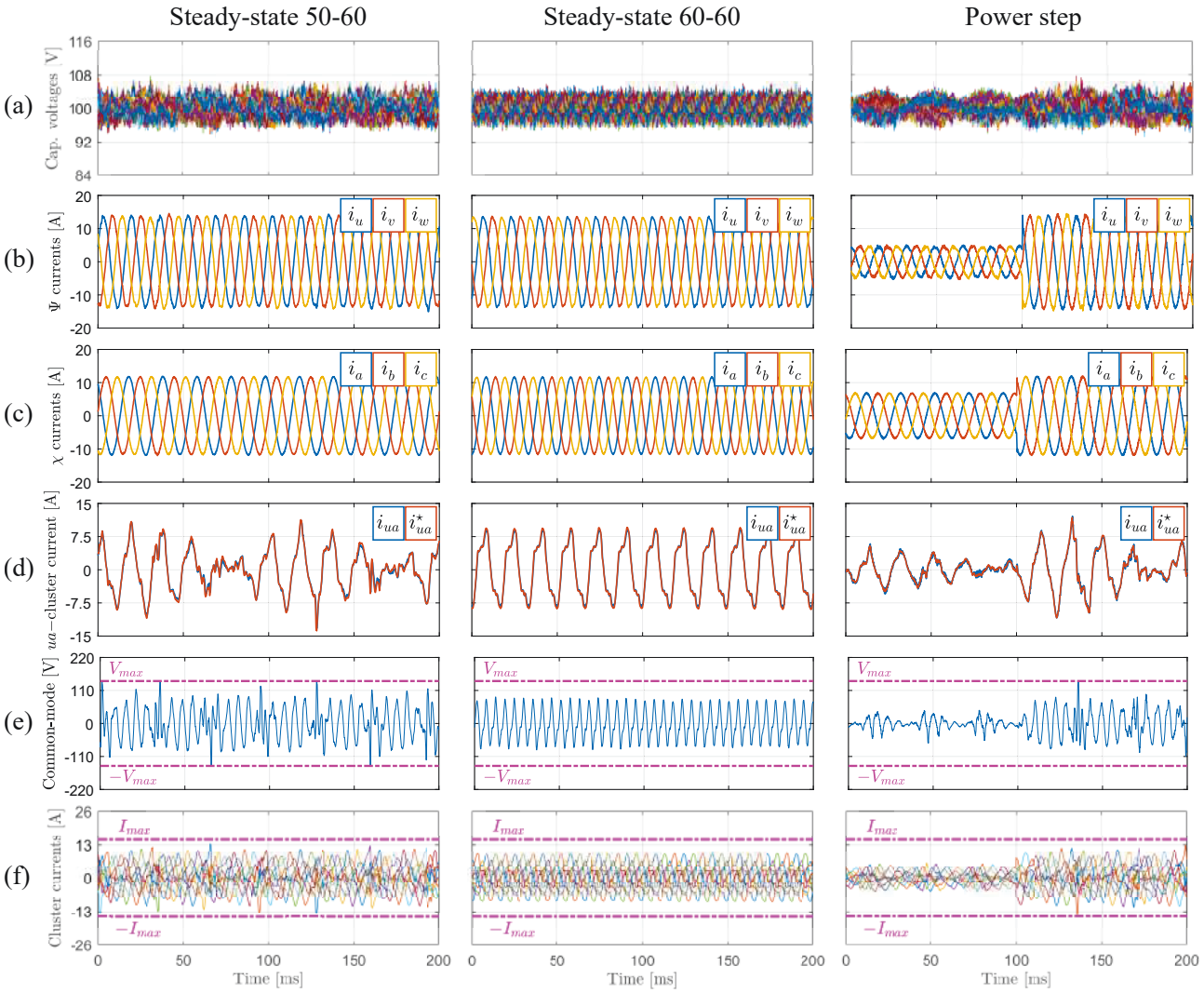

Figure 5.5: Experimental performance in steady-state operating at 50-60 Hz, 60-60 Hz, and a power step at 60-50 Hz. (a) capacitor voltages, (b) input currents, (c) output currents, (d) tracking of $ua-$cluster current, (e) CMV, and (f) cluster currents.

5.4.1 Steady-State Performance

The results of the steady state performance of the proposal are presented in Fig. 5.5, for different frequency mode (50-60) and equal frequency mode (60-60), being the latter a critical operating point. The capacitor voltages are properly regulated to the expected value of 100 V, presenting a ripple of ±6 V as are shown in Fig. 5.5(a) and an average tracking error of 2 V. Hence, the local cluster balancing control is properly addressed by the proposal. The proposed strategy governs the M3C to extract 3kW from the input and inject it to the output-port as is presented in the balanced current waveforms from both ports in Fig. 5.5(b) and 5.5(c).

The cluster tracking is presented in Fig. 5.5(d), where the $ua-$cluster current achieves an average tracking error of 0.57 A. Additionally, the proposal generates a THD of 2.83 and 1.01% of THD for the i_u and i_a currents, respectively. Moreover, the obtained WTHD for both currents are 0.9 and 0.21%, respectively.

Finally, the CMV and circulating current references are presented in Fig. 5.5(e) and 5.5(f), which always are between its upper an lower bounds. Additionally, the proposal generates

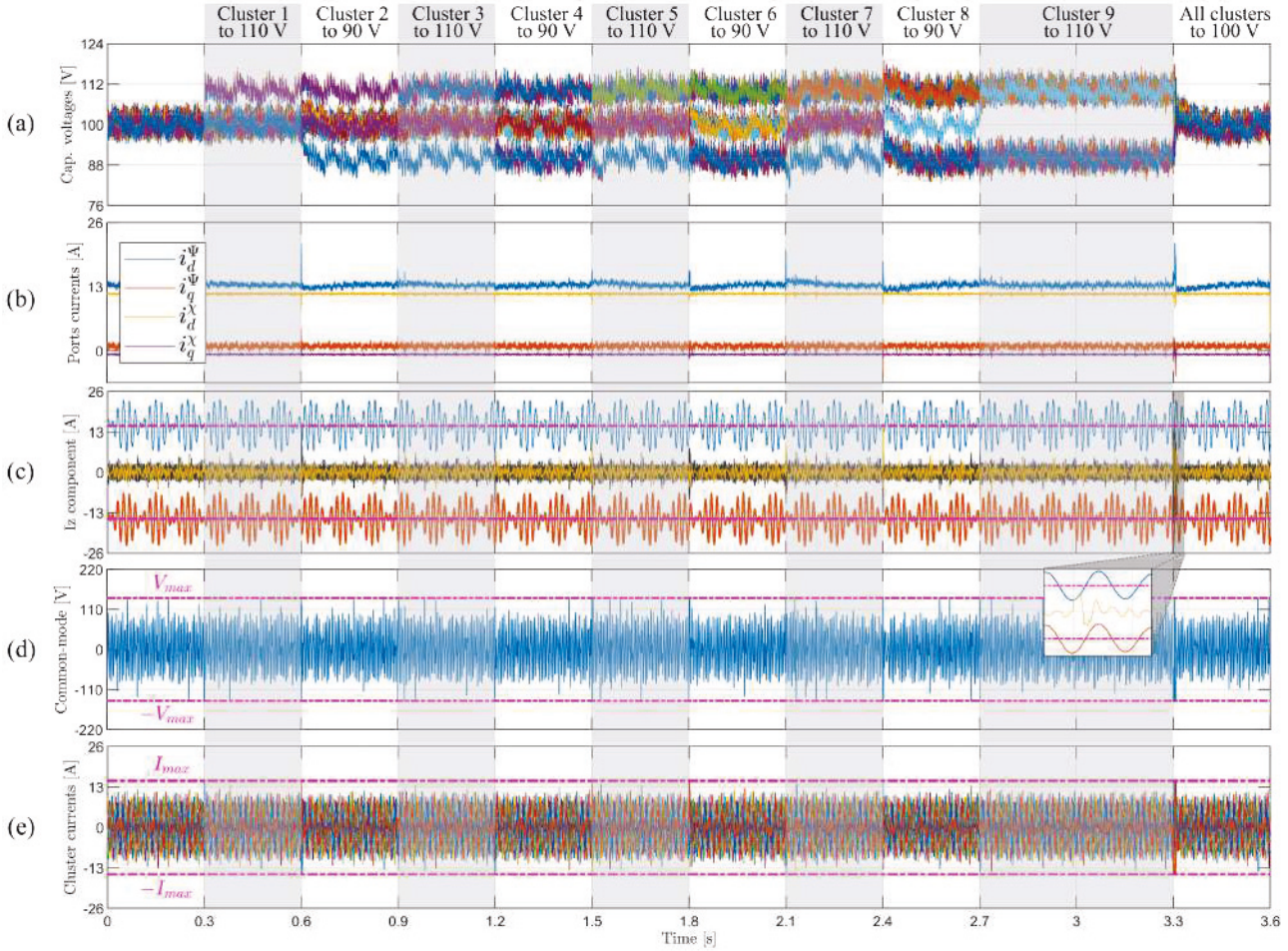

Figure 5.6: Experimental performance under cluster energy imbalance operation. (a) capacitor voltages, (b) input and output currents, (c) circulating current reference with upper and lower bounds of *ua*-cluster, (d) CMV, and (e) cluster currents.

references and governs the M3C in a safe operating region, as can be appreciated in Fig. 5.5(f), where the cluster current references are kept between $\pm I_{\max}$ A.

5.4.2 Dynamic Performance

The proposal has been tested under different step changes to present its dynamic performance under suddenly power, cluster energy, and output frequency step in Fig. 5.5, 5.6 and 5.7, respectively.

Power Step Change

The dynamic response of a suddenly power step is almost instantaneous with no overshoot in output nor input currents as Fig. 5.5(b) and 5.5(c) present. As expected, the current levels increase due to the increment of power, including input, output and cluster currents (see Fig. 5.5(d)). Moreover, the voltages are not an exception, the voltage levels also rise, as can be seen in the capacitor voltages ripple in Fig. 5.5(a). Nonetheless, the capacitor voltages are always maintain around their voltage reference.

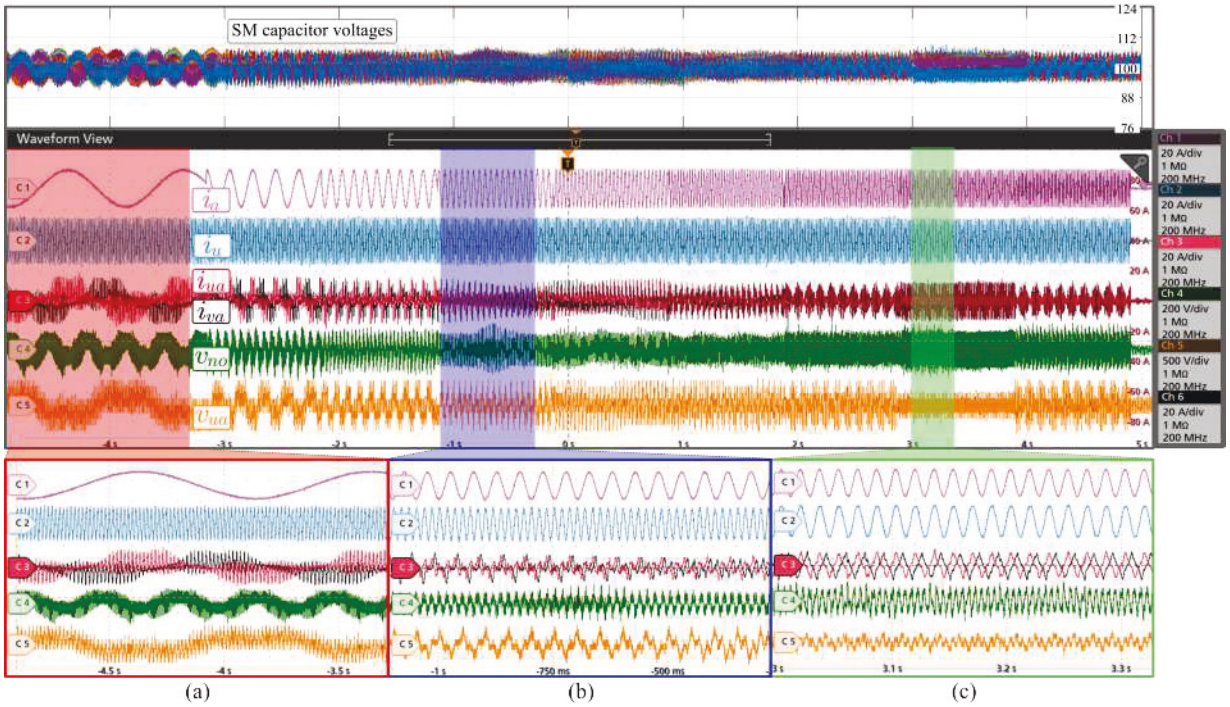

Figure 5.7: Experimental dynamic performance, frequency at 1 to 70 Hz. (a) output frequency at 1 Hz, (b) output frequency at 20 Hz, and (c) output frequency at 60 Hz. Top graph: capacitor voltages. Bottom graphs (oscilloscope waveforms): i_a (Ch 1), i_u (Ch 2), i_{ua} (Ch 3), v_{no} (Ch 4), v_{ua} (Ch 5), and i_{va} (Ch 6).

Cluster Energy Steps and Unbalanced Operation

The proposed two-stage MPC has been tested under cluster energy steps, operating with unbalanced stored energy per cluster. In this test, the energy cluster references are changed every 0.3 s, increasing or decreasing the energy of only one cluster each instant by +4.14 J (equivalent to increase the capacitor voltages by 10 V) or by −3.75 J (equivalent to decrease the capacitor voltages by 10 V). Additionally, at the instant 3.3 s, the proposal governs the M3C to balanced all the clusters to the initial state.

During this test, the capacitor voltages are kept in their energy reference (see Fig. 5.6a), achieving an unbalanced operation with regard the stored cluster energies while the M3C transfers 3 kW from one port to the other as Fig. 5.6b shows. Notice that the circulating current component and the CMV references are always inside their upper and lower bounds, saturating their values when needed as is presented in the zoom of Fig. 5.6c. Moreover, it is important to mention that the circulating current references are always a feasible operation point for the M3C, allowing to the sequential PS-MPC to use all the available current in the cluster to balance the energy among clusters. As a result, the cluster currents are always between $\pm I_{\max}$ A.

Different Output Frequencies Performance

The proposal can operate at any frequency between 1 and 70 Hz with a low capacitor ripple as can be appreciated in Fig. 5.7. In this test, the output frequency is suddenly changed every second starting from instant −3 to 5 s and the frequencies are 1, 5, 10, 20, 30, 40, 50, 60 and 70 Hz. As depicted in Fig. 5.7, the output current is achieved independent of the frequency and the dynamic response under frequency steps is fast with no overshoot. Moreover, the converter

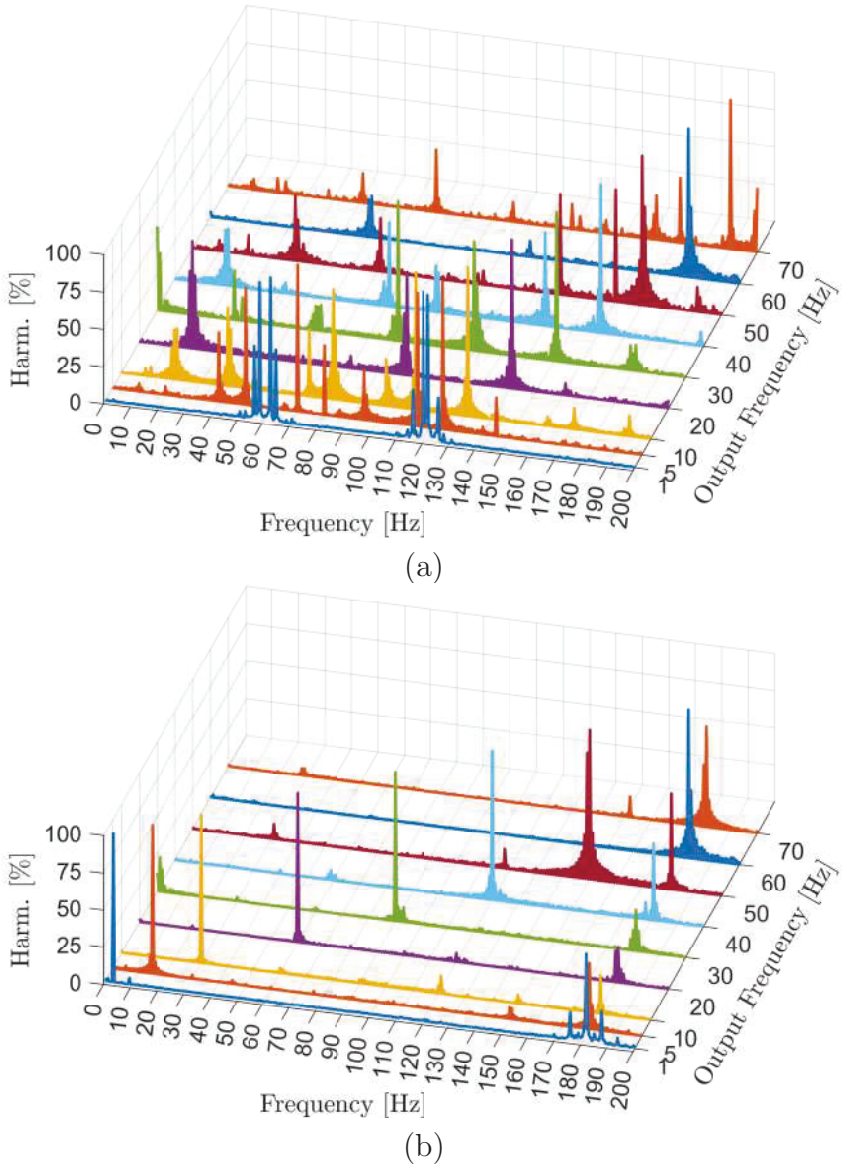

Figure 5.8: Experimental spectrum with output frequency from 1 to 70 Hz. (a) cluster circulating current and (b) CMV.

is able to operate in the critical point (60-60 Hz).

Additionally, Fig. 5.8 illustrates the frequency components generated by the proposed MPC for different output frequencies. As a pattern, the proposal always generates circulating current components at $|2f_\psi \pm f_\chi|$ and $|2f_\chi \pm f_\psi|$. Nevertheless, it might inject additional components. It is important to mention that constraint (5.12c) ensures that any generated harmonic does not affect input or output currents. Regarding CMV, the proposed MPC always generates components at $3f_\psi$ and $3f_\chi$. Nonetheless, similarly as the circulating currents, the proposal might inject additional frequency components for CMV.

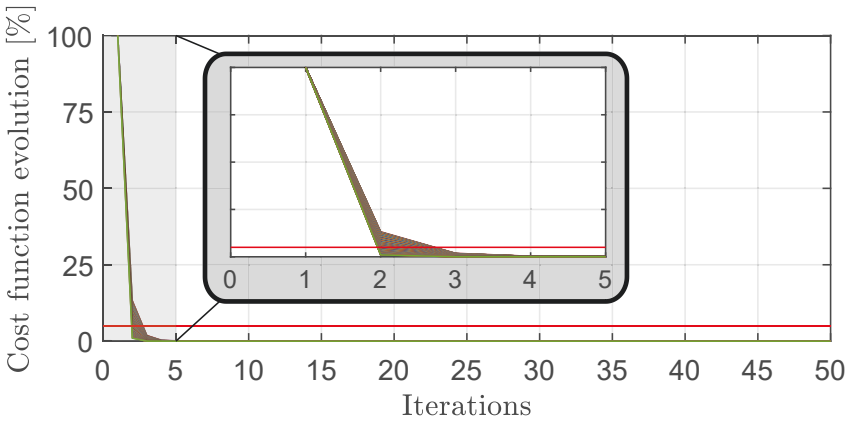

Figure 5.9: Normalized cost function convergence rate $J_{\%}^{(i)}$ during a steady-state scenario.

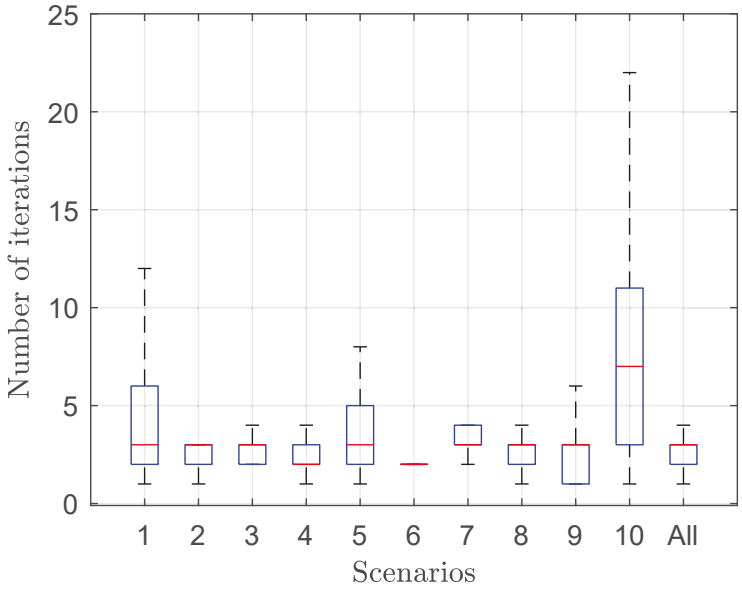

Figure 5.10: Box-and-whisker diagram summarising the number of iterations required for transient scenarios shown in Fig. 5.6.

Table 5.2: CMV design impact in comparison with literature.

Index	MPC		Proposal	
	1 Hz	60 Hz	1 Hz	60 Hz
Compared error $\triangle V_C/\triangle V_{C\text{MPC}}$	1	1	0.26	0.52
RMS circulating current [A]	3.94	1.67	3.94	1.67
RMS CMV [V]	0	60	33.56	41.2
CC frequency components	Multiples		Multiples	
CMV frequency components	1		Multiples	

5.4.3 Cost Function Evolution Over Iterations

To evaluate the convergence of the algorithm, the normalized cost function value as a function of the number of iterations, $J_{\%}^{(i)}$ in (5.20), is used as index performance.

$$J_{\%}^{(i)} = \frac{J^{(i)} - J^{(50)}}{J^{(1)}} \times 100 \tag{5.20}$$

Fig. 5.9 shows that, for steady-state operating conditions, the cost function value decreases with the iterations until converging to the optimal value. Notice that, in steady-state, only three iterations are required to have an error lower than 5 % (red line). Nevertheless, to test more challenging scenarios, we comprehensively analyzed the convergence rate of the 10 transients shown in Fig. 5.6. The results are analyzed in the box and whisker plot of Fig. 5.10, where most transient scenarios require only 3 iterations to converge to the optimal value (error smaller than 5%), although some cases require more iterations. Nonetheless, based on the results of Fig. 5.10, the proposed ICB control achieves the optimal with three iterations for 75% of the analyzed transient scenarios. Therefore, by considering $n_i = 3$, the proposal will properly cover three out of four scenarios during transient and almost every case during steady-state. On one hand, if n_i is too small (≈ 1), the solution obtained by the proposal will present a considerable error regarding the optimal. On the other hand, if n_i is too big, the execution time of the proposal will highly increase, slightly improving the performance of the ICB control. Hence, by selecting n_i, there is a trade-off between the execution time and the solution regarding the optimum.

5.4.4 Comparison with a state-of-the-art strategy

The proposal has been compared with the circulating current generator based on MPC presented in [46]. As is shown in Fig. 5.11, the comparison considers the operation of the M3C in critical points which are low and equal frequencies (1 and 60 Hz, respectively) while the other port remains constant at 60 Hz. When the output frequency is 1 Hz, the proposal achieves a root mean squared error of the capacitor voltages of $\triangle V_C = 3.08$ in comparison with $\triangle V_C = 4.44$ obtained by [46]. On the other hand, when the frequencies are equal, the proposal and [46] present a root mean squared error of the capacitor voltages of $\triangle V_C = 2.17$ and $\triangle V_C = 3.39$, respectively.

The generated CMV presents two main frequency components, the first related with the input frequency and the second with the output frequency, which correspond to the third harmonic of the mentioned frequencies. For instance, when the output frequency is 1 Hz, the generated CMV clearly presents a high and low frequency components, the high frequency component is 180 Hz and the low frequency is 3 Hz as is presented in Fig. 5.11(c). In contrast, [46] does not consider a common-mode voltage for low frequency operation. When the system operates with equal frequencies (60 Hz), the CMV has a main frequency component at 180 Hz as expected which is presented in 5.12(c).

In both cases, the proposal is able to reduce the energy mismatch among clusters, reducing the root mean squared error of the capacitor voltages in 31% at low frequencies and up to 36% at equal frequencies in comparison with [46].

Finally, the proposed strategy was compared by simulation with the one presented in [46], which only optimized the circulating currents. In this test, the weighting factor λ_z, which penalizes the circulating current control action, has been adjusted to obtain the same RMS value for

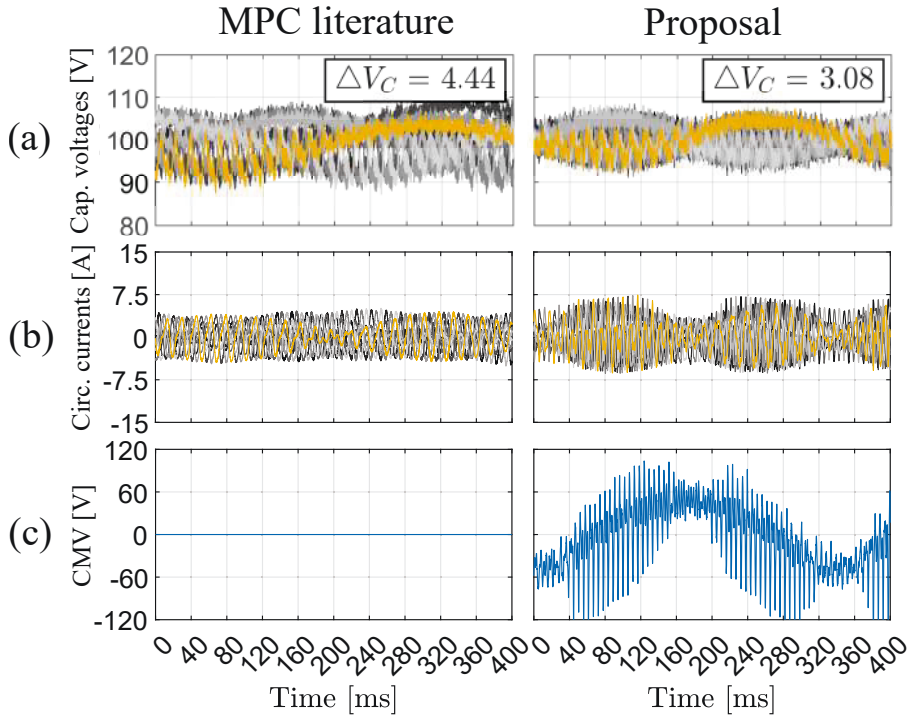

Figure 5.11: Experimental comparison at low frequency 1 Hz.

circulating currents as [46]. Table 5.2 presents the results, showing both strategies generating the same RMS value for circulating currents. Nevertheless, compared with [46], the proposal improves the average capacitor voltage error by 74 and 48 % when operating at 1 Hz and 60 Hz, respectively. To achieve that improvement, the proposal generates a CMV reference that highly reduces the capacitor ripple. Despite that [46] only use one frequency component for the CMV, the proposal might use multiple frequency components to reduce the cost function (5.8).

5.5 Conclusion

This chapter presented an optimal reference generator of circulating currents and common-mode voltage to perform the ICB control and the LFO mitigation of an M3C. This work derived the cluster energies model in the original framework, simplifying the control scheme of an M3C. On one hand, the circulating current subproblem ensures that the generated circulating currents do not distort input nor output ports and maintains the cluster current references within its feasible limits. On the other hand, the CMV subproblem allows one to obtain a constrained CMV reference which is specially useful for mitigation when the converter operates at critical points.

Additionally, the proposed reference generator was tested in an M3C prototype with 36 SMs. The experimental results showed the effectiveness of the energy balance capabilities of the proposal even during low and equal frequencies operation while keeping the cluster currents and common-mode voltage under safe limits. Finally, future work may consider the optimization of the amplitude for the obtained frequency components over a period.

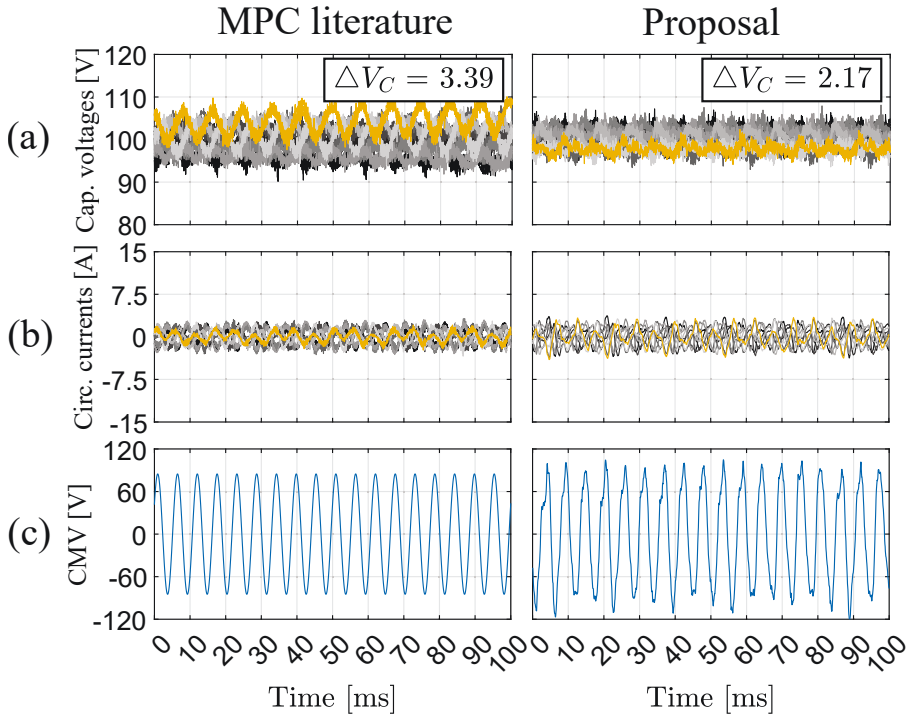

Figure 5.12: Experimental comparison at equal frequency 60 Hz.

Chapter 6

CONCLUSIONS AND FUTURE WORK

6.1 Conclusions

This research proposed predictive control strategies for the modular multilevel matrix converter (M3C). This control strategy was divided in two parts, the current and local cluster balancing controllers (inner controller); and the inter-cluster balancing controller (outer controller).

Chapter 2 proposed an inner control strategy based on long horizon FCS-MPC. Experimental results were performed to validate the proposal up to horizon 4 and to compared with other FCS-MPC strategies. As a result, the proposed sequential FCS-MPC-H4 presented fast dynamic response and steady-state performance when tracking the cluster currents with multiple frequency components. Additionally, in comparison with FCS-MPC from literature, the proposal highly reduced the average switching frequency and computational burden, increasing its scalability.

Chapter 3 presented an inner control strategy based on a PS-MPC, where the cluster currents are derived in the double$-\alpha\beta 0$. Based on the experimental results, the proposal proved its effectiveness to govern an M3C, tracking input, output, circulating currents and regulating the capacitor voltages locally. Additionally, the proposal obtained the optimal duty cycles no only during steady-state but transients as well. Moreover, the resulting voltage waveform presented fixed switching frequency with low distortion and distributed power losses among power switches.

Chapter 4 proposed a constrained optimal circulating current generator as inter-cluster balancing control for the M3C, where the cluster energies were derived in the double$-\alpha\beta 0$. However, the circulating currents were kept in the original framework. The experimental results of the constrained MPC showed an effective balance of the energy among clusters while operating the M3C in safe zone all the time, because the proposal considered upper and lower bound for circulating currents. Therefore, the proposed circulating generator overcame optimal generator from literature by guarantying a safe operation of the M3C and using full range of the available cluster currents, independently of the controller tuning.

The chapter 5 presented an optimal reference generator of circulating currents and common-mode voltage to perform the ICB control and the low-frequency oscillation mitigation of an

M3C. This proposal was designed completely in the original framework. The proposed reference generator was tested in an M3C prototype with 36 SMs. The experimental results showed the effectiveness of the energy balance capabilities of the proposal even during low and equal frequencies operation while keeping the cluster currents and common-mode voltage under safe limits. On one hand, the circulating current subproblem ensures that the generated circulating currents do not distort input nor output ports and maintains the cluster current references within its feasible limits. On the other hand, the CMV subproblem allows one to obtain a constrained CMV reference which is specially useful for mitigation when the converter operates at critical points.

Both hypotheses have been proved during this research.

H1: It is possible to unified the current control and local-cluster balancing (LCB) control with a finite-control-set MPC and phase-shifted MPC over a wide frequency range, obtaining a fixed voltage and current spectrum (for the sequential PS-MPC strategy) and a high scalability (linear increment in the case of the sequential PS-MPC).

H2: The constrained MPC-based reference generator improves the performance of the M3C in steady-state in terms of capacitor voltage ripple and ensures safety operation of the converter for a wide frequency range, including critical frequencies.

6.2 Future Work

As future work or extensions of this work, the following ideas are raised:

- To analyze the frequency domain of the different loops, the robustness of the MPC strategies and how the improvements of the different proposal impact in the sizing of capacitors and inductors of an M3C.

- To obtain an extended state-space for the controllers and incorporate disturbances to achieve zero steady-state error. This idea arises because MPC strategies are very sensitive to the model. Hence, by considering an extended state-space model to include unknown disturbance it is possible to operate with a model which presents inaccuracies.

- To design an inner controller of an M3C to manage faults in one and two clusters. The standard solution when the M3C presents a faulty cluster is to operate it with six cluster, working as an Hexverter. This idea aims to consider an inner controller that allows to operate the M3C with eight or seven cluster instead of shutting down two clusters that can properly work.

- To design an outer controller of an M3C that considers faults in one and two clusters. By taking into account the previous idea, it is important to support it with an outer controller that allows to regulate the energy of the M3C with only eight or seven cluster as well.

- To increase the prediction horizon of the sPS-MPC and evaluate the computational burden. The developed sPS-MPC presents upper and lower bound for duty cycles, evaluating a larger horizon might improve the performance of the controller in steady-state and/or under a power step.

- To analyze the circulating current frequency components and optimize the amplitude over a period as ICB control. In order to improve the performance of the obtained controllers, by considering fixed frequency components and optimizing over the period, it is possible to reduce the sample frequency of the ICB control and obtain a better performance of capacitor voltage oscillations and/or cluster currents over a period.

- To analyze the common-mode voltage and optimize the amplitude over a period as ICB control. It might be possible to reduce the sampling frequency of the ICB control and increase the horizon over a period of some specific frequency components for the CMV to improve the performance of the ICB control over a period of the selected frequency components.

- To consider one optimization for current, LCB and ICB control. In this research, two controllers were implemented at the same sampling frequency to achieve current, LCB and ICB controls. It might be possible to mixed those controllers and obtain only one

controller.

- To evaluate the use of batteries in the M3C for micro grids, in applications such as cruisers and small systems based on WECS. The battery energy storage systems are the main alternative to storage a large amount of energy. By considering batteries in the SMs, the M3C will be able to inject independent active and reactive power to the ports. Hence, the M3C can work as storage system for propulsion systems and grid supply in marine vessels and other micro grid systems.

- To consider a distributed control system strategy for the M3C. This idea aims to reduce the computational burden required by a central controller and divided it in several microcontrollers, allowing to reduce the computational effort even more. The distributed control can be applied per cluster and per SMs.

Bibliography

[1] S. S. Sharma, "The relationship between energy and economic growth: Empirical evidence from 66 countries," *Applied Energy*, vol. 87, no. 11, pp. 3565–3574, 2010, ISSN: 0306-2619. DOI: https://doi.org/10.1016/j.apenergy.2010.06.015. [Online]. Available: http://www.sciencedirect.com/science/article/pii/S0306261910002291.

[2] United Nations Framework Convention on Climate Change, "Chile madrid time for action," United Nations Framework Convention on Climate Change, 2019. [Online]. Available: https://unfccc.int/sites/default/files/resource/cp2019_L10E_adv.pdf.

[3] UK Government, "Cop26 presidency outcomes," UK Government, 2022. [Online]. Available: https://webarchive.nationalarchives.gov.uk/ukgwa/20230311031856mp_/https://ukcop26.org/wp-content/uploads/2022/11/COP26-Presidency-Outcomes.pdf.

[4] United Nations Framework Convention on Climate Change, "Climate action and support trends," United Nations Framework Convention on Climate Change, 2019. [Online]. Available: https://unfccc.int/sites/default/files/resource/Climate_Action_Support_Trends_2019.pdf.

[5] Ministerio de Energía, "Ruta energética 2018-2022," Ministerio de Energía, 2018. [Online]. Available: https://energia.gob.cl/sites/default/files/documentos/ruta_energetica_2018-2022.pdf.

[6] Department of Climate Change, Energy, the Environment and Water, "Australian energy update 2022," Australian Government, 2022. [Online]. Available: https://www.energy.gov.au/sites/default/files/Australian%5C%20Energy%5C%20Statistics%5C%202022%5C%20Energy%5C%20Update%5C%20Report.pdf.

[7] Ministerio de Energía, "Planificación energética de largo plazo," Gobierno de Chile, 2021. [Online]. Available: https://energia.gob.cl/sites/default/files/documentos/pelp2023-2027_informe_preliminar.pdf.

[8] Australian Energy Market Operator, "2022 integrated system plan," Australian Energy Market Operator, 2022. [Online]. Available: https://aemo.com.au/-/media/files/major-publications/isp/2022/2022-documents/2022-integrated-system-plan-isp.pdf?la=en.

[9] AF-Mercados EMI, "Actualización de la interconexión eléctrica chile-perú," AF-Mercados EMI, 2019. [Online]. Available: https://energia.gob.cl/sites/default/files/documentos/af_mercados-2019_conexion_chile-peru_2da_etapa.pdf.

[10] M. Diaz, R. Cárdenas, E. Ibaceta, *et al.*, "An overview of applications of the modular multilevel matrix converter," *Energies*, vol. 13, no. 21, 2020, ISSN: 1996-1073. DOI: 10.3390/en13215546. [Online]. Available: https://www.mdpi.com/1996-1073/13/21/5546.

[11] M. Diaz, R. Cardenas, M. Espinoza, *et al.*, "Control of wind energy conversion systems based on the modular multilevel matrix converter," *IEEE Transactions on Industrial Electronics*, vol. 64, no. 11, pp. 8799–8810, 2017.

[12] W. Kawamura, M. Hagiwara, and H. Akagi, "Control and experiment of a modular multilevel cascade converter based on triple-star bridge cells," *IEEE Transactions on Industry Applications*, vol. 50, no. 5, pp. 3536–3548, 2014. DOI: 10.1109/TIA.2014.2311759.

[13] P. Bravo, J. Pereda, M. M. C. Merlin, S. Neira, T. C. Green, and F. Rojas, "Modular multilevel matrix converter as solid state transformer for medium and high voltage ac substations," *IEEE Transactions on Power Delivery*, vol. 37, no. 6, pp. 5033–5043, 2022. DOI: 10.1109/TPWRD.2022.3166258.

[14] J. Pereda and T. C. Green, "Direct modular multilevel converter with six branches for flexible distribution networks," *IEEE Transactions on Power Delivery*, vol. 31, no. 4, pp. 1728–1737, 2016. DOI: 10.1109/TPWRD.2016.2521262.

[15] A. J. Korn, M. Winkelnkemper, P. Steimer, and J. W. Kolar, "Direct modular multilevel converter for gearless low-speed drives," in *Proceedings of the 2011 14th European Conference on Power Electronics and Applications*, 2011.

[16] M. Diaz, R. Cardenas, M. Espinoza, *et al.*, "Vector control of a modular multilevel matrix converter operating over the full output-frequency range," *IEEE Transactions on Industrial Electronics*, vol. 66, no. 7, pp. 5102–5114, 2019.

[17] W. Kawamura, K. Chen, M. Hagiwara, and H. Akagi, "A low-speed, high-torque motor drive using a modular multilevel cascade converter based on triple-star bridge cells (mmcc-tsbc)," *IEEE Transactions on Industry Applications*, vol. 51, no. 5, pp. 3965–3974, 2015.

[18] J. Ma, M. S. A. Dahidah, V. Pickert, and J. Yu, "A hierarchical energy balance control method for m3c based on injecting output frequency circulating currents," *IEEE Transactions on Power Electronics*, vol. 35, no. 3, pp. 2424–2435, 2020.

[19] C. S. Lim, E. Levi, M. Jones, N. A. Rahim, and W. P. Hew, "Fcs-mpc-based current control of a five-phase induction motor and its comparison with pi-pwm control," *IEEE Transactions on Industrial Electronics*, vol. 61, no. 1, pp. 149–163, 2014. DOI: 10.1109/TIE.2013.2248334.

[20] A. Mora, M. Espinoza, M. Diaz, and R. Cardenas, "Model predictive control of modular multilevel matrix converter," in *2015 IEEE 24th International Symposium on Industrial Electronics (ISIE)*, 2015, pp. 1074–1079.

[21] A. Dekka, B. Wu, V. Yaramasu, R. L. Fuentes, and N. R. Zargari, "Model predictive control of high-power modular multilevel converters-an overview," *IEEE Journal of Emerging and Selected Topics in Power Electronics*, vol. 7, no. 1, pp. 168–183, 2019. DOI: 10.1109/JESTPE.2018.2880137.

[22] R. P. Aguilera, P. Acuna, X. Su, P. Lezana, and B. McGrath, "Sequential phase-shifted model predictive control for multicell power converters," in *2017 IEEE Southern Power Electronics Conference (SPEC)*, 2017, pp. 1–6.

[23] R. Cuzmar, J. Pereda, and R. P. Aguilera, "Phase-shifted model predictive control to achieve power balance of chb converters for large-scale photovoltaic integration," *IEEE Transactions on Industrial Electronics*, pp. 1–1, 2020.

[24] P. Poblete, S. Neira, R. P. Aguilera, J. Pereda, and J. Pou, "Sequential phase-shifted model predictive control for modular multilevel converters," *IEEE Transactions on Energy Conversion*, pp. 1–1, 2021. DOI: 10.1109/TEC.2021.3074863.

[25] M. Diaz, R. Cardenas, E. Ibaceta, *et al.*, "An overview of modelling techniques and control strategies for modular multilevel matrix converters," *Energies*, vol. 13, no. 18, 2020, ISSN: 1996-1073. [Online]. Available: https://www.mdpi.com/1996-1073/13/18/4678.

[26] W. Yao, J. Liu, and Z. Lu, "Distributed control for the modular multilevel matrix converter," *IEEE Transactions on Power Electronics*, vol. 34, no. 4, pp. 3775–3788, 2019.

[27] S. Liu, M. Saeedifard, and X. Wang, "Analysis and control of the modular multilevel matrix converter under unbalanced grid conditions," *IEEE Journal of Emerging and Selected Topics in Power Electronics*, vol. 6, no. 4, pp. 1979–1989, 2018. DOI: 10.1109/JESTPE.2018.2812723.

[28] A. Duran, E. Ibaceta, M. Diaz, F. Rojas, R. Cardenas, and H. Chavez, "Control of a modular multilevel matrix converter for unified power flow controller applications," *Energies*, vol. 13, no. 4, 2020, ISSN: 1996-1073. DOI: 10.3390/en13040953. [Online]. Available: https://www.mdpi.com/1996-1073/13/4/953.

[29] M. Urrutia, R. Cárdenas, J. Clare, and A. Watson, "Circulating current control for the modular multilevel matrix converter based on model predictive control," *IEEE Journal of Emerging and Selected Topics in Power Electronics*, pp. 1–1, 2021. DOI: 10.1109/JESTPE.2021.3071964.

[30] W. Kawamura, Y. Chiba, M. Hagiwara, and H. Akagi, "Experimental verification of an electrical drive fed by a modular multilevel tsbc converter when the motor frequency gets closer or equal to the supply frequency," *IEEE Transactions on Industry Applications*, vol. 53, no. 3, pp. 2297–2306, 2017.

[31] J. Liu, S. Yue, W. Yao, W. Li, and Z. Lu, "Dc voltage ripple optimization of a single-stage solid-state transformer based on the modular multilevel matrix converter," *IEEE Transactions on Power Electronics*, vol. 35, no. 12, pp. 12 801–12 815, 2020.

[32] B. Fan, K. Wang, P. Wheeler, C. Gu, and Y. Li, "A branch current reallocation based energy balancing strategy for the modular multilevel matrix converter operating around equal frequency," *IEEE Transactions on Power Electronics*, vol. 33, no. 2, pp. 1105–1117, 2018. DOI: 10.1109/TPEL.2017.2685431.

[33] Y. Wan, S. Liu, and J. Jiang, "Systematic modeling and control of indirect modular multilevel converter (mmc) with grid unbalance estimation," in *IECON 2013 - 39th Annual Conference of the IEEE Industrial Electronics Society*, 2013, pp. 1349–1354. DOI: 10.1109/IECON.2013.6699328.

[34] S. Vazquez, J. Rodriguez, M. Rivera, L. G. Franquelo, and M. Norambuena, "Model predictive control for power converters and drives: Advances and trends," *IEEE Transactions on Industrial Electronics*, 2017.

[35] M. A. Perez, S. Ceballos, G. Konstantinou, J. Pou, and R. P. Aguilera, "Modular Multilevel Converters: Recent Achievements and Challenges," *IEEE Open Journal of the Industrial Electronics Society*, vol. 2, pp. 224–239, 2021. DOI: 10.1109/OJIES.2021.3060791.

[36] M. A. Perez, S. Bernet, J. Rodriguez, S. Kouro, and R. Lizana, "Circuit topologies, modeling, control schemes, and applications of modular multilevel converters," *IEEE Transactions on Power Electronics*, vol. 30, no. 1, pp. 4–17, 2015.

[37] F. Briz, M. Lopez, A. Rodriguez, and M. Arias, "Modular power electronic transformers: Modular multilevel converter versus cascaded h-bridge solutions," *IEEE Industrial Electronics Magazine*, vol. 10, no. 4, pp. 6–19, 2016.

[38] A. Mora, M. Urrutia, R. Cardenas, *et al.*, "Model-predictive-control-based capacitor voltage balancing strategies for modular multilevel converters," *IEEE Transactions on Industrial Electronics*, vol. 66, no. 3, pp. 2432–2443, 2019. DOI: 10.1109/TIE.2018.2844842.

[39] A. Romero-Becerril and L. Alvarez-Icaza, "Comparison of discretization methods applied to the single-particle model of lithium-ion batteries," *Journal of Power Sources*, 2011.

[40] R. P. Aguilera and D. E. Quevedo, "Predictive control of power converters: Designs with guaranteed performance," *IEEE Transactions on Industrial Informatics*, vol. 11, no. 1, pp. 53–63, 2015. DOI: 10.1109/TII.2014.2363933.

[41] D. E. Quevedo, R. P. Aguilera, and T. Geyer, "Model predictive control for power electronics applications," *Handbook of Model Predictive Control*, 2018.

[42] D. E. Quevedo, R. P. Aguilera, and T. Geyer, "Predictive control in power electronics and drives: Basic concepts, theory, and methods," in *Advanced and Intelligent Control in Power Electronics and Drives*, T. Orłowska-Kowalska, F. Blaabjerg, and J. Rodríguez, Eds. Springer International Publishing, 2014.

[43] R. H. Cuzmar, A. Mora, J. Pereda, P. Poblete, and R. P. Aguilera, "Long-horizon sequential fcs-mpc approaches for modular multilevel matrix converters," *IEEE Transactions on Industrial Electronics*, pp. 1–11, 2023. DOI: 10.1109/TIE.2023.3286013.

[44] B. Fan, K. Wang, P. Wheeler, C. Gu, and Y. Li, "An optimal full frequency control strategy for the modular multilevel matrix converter based on predictive control," *IEEE Transactions on Power Electronics*, vol. 33, no. 8, pp. 6608–6621, 2018. DOI: 10.1109/TPEL.2017.2755767.

[45] M. Urrutia, R. Cárdenas, J. C. Clare, M. Díaz, and A. Watson, "Continuous set model predictive control for energy management of modular multilevel matrix converters," *IEEE Transactions on Power Electronics*, vol. 37, no. 5, pp. 5731–5748, 2022. DOI: 10.1109/TPEL.2021.3133695.

[46] R. Cuzmar, A. Montenegro, A. Mora, J. Pereda, and R. P. Aguilera, "Constrained mpc for intercluster energy control of modular multilevel matrix converters," *IEEE Transactions on Industrial Electronics*, pp. 1–11, 2023. DOI: 10.1109/TIE.2023.3303641.

[47] R. Baidya, R. P. Aguilera, P. Acuña, *et al.*, "Enabling multistep model predictive control for transient operation of power converters," *IEEE Open Journal of the Industrial Electronics Society*, vol. 1, pp. 284–297, 2020. DOI: 10.1109/OJIES.2020.3029358.

[48] M. Al-Tameemi, Y. Miura, J. Liu, H. Bevrani, and T. Ise, "A Novel Control Scheme for Multi-Terminal Low-Frequency AC Electrical Energy Transmission Systems Using Modular Multilevel Matrix Converters and Virtual Synchronous Generator Concept," *Energies*, vol. 13, no. 3, p. 747, Feb. 2020, ISSN: 1996-1073. DOI: 10.3390/en13030747. [Online]. Available: https://www.mdpi.com/1996-1073/13/3/747.

[49] Y. Okazaki, W. Kawamura, M. Hagiwara, *et al.*, "Experimental comparisons between modular multilevel dscc inverters and tsbc converters for medium-voltage motor drives," *IEEE Transactions on Power Electronics*, vol. 32, no. 3, pp. 1805–1817, Mar. 2017, ISSN: 0885-8993. DOI: 10.1109/TPEL.2016.2562103.

[50] M. Lei, Y. Li, Z. Li, *et al.*, "A single-phase five-branch direct ac-ac modular multilevel converter for railway power conditioning," *IEEE Transactions on Industrial Electronics*, vol. 67, no. 6, pp. 4292–4304, Jun. 2020, ISSN: 1557-9948. DOI: 10.1109/TIE.2019.2926045.

[51] H. Akagi, "Classification, terminology, and application of the modular multilevel cascade converter (mmcc)," *IEEE Transactions on Power Electronics*, vol. 26, no. 11, pp. 3119–3130, Nov. 2011, ISSN: 0885-8993. DOI: 10.1109/TPEL.2011.2143431.

[52] Y. Miura, T. Mizutani, M. Ito, and T. Ise, "Modular multilevel matrix converter for low frequency AC transmission," in *Proceedings of the International Conference on Power Electronics and Drive Systems*, IEEE, Apr. 2013, pp. 1079–1084, ISBN: 9781467317900. DOI: 10.1109/PEDS.2013.6527180.

[53] J. Kucka, D. Karwatzki, and A. Mertens, "Optimised operating range of modular multilevel converters for ac/ac conversion with failed modules," in *2015 17th European Conference on Power Electronics and Applications (EPE'15 ECCE-Europe)*, 2015, pp. 1–10.

[54] D. Karwatzki and A. Mertens, "Generalized control approach for a class of modular multilevel converter topologies," *IEEE Transactions on Power Electronics*, vol. 33, no. 4, pp. 2888–2900, Apr. 2018, ISSN: 0885-8993. DOI: 10.1109/TPEL.2017.2703917.

[55] B. Fan, K. Wang, Z. Zheng, L. Xu, and Y. Li, "Optimized branch current control of modular multilevel matrix converters under branch fault conditions," *IEEE Transactions on Power Electronics*, vol. 33, no. 6, pp. 4578–4583, 2018.

[56] H. Akagi, E. H. Watanabe, and M. Aredes, *Instantaneous Power Theory and Applications to Power Conditioning*. Wiley-IEEE Press, 2017, ISBN: 1118362101.

[57] S. Boyd and L. Vandenberghe, *Convex Optimization*. Cambridge University Press, 2004, ISBN: 9780521833783.

[58] D. P. Bertsekas, *Convex Optimization Algorithms*. Athena Scientific; 1st edition, 2015, ISBN: 1886529280.

[59] P. Poblete, J. Gajardo, R. H. Cuzmar, *et al.*, "Predictive optimal variable-angle ps-pwm strategy for cascaded h-bridge converters," *IEEE Transactions on Industrial Electronics*, pp. 1–11, 2024. DOI: 10.1109/TIE.2024.3370998.

[60] Q. Xiao, Y. Jin, H. Jia, *et al.*, "Review of fault diagnosis and fault-tolerant control methods of the modular multilevel converter under submodule failure," *IEEE Transactions on Power Electronics*, vol. 38, no. 10, pp. 12 059–12 077, 2023. DOI: 10.1109/TPEL.2023.3283286.

[61] D. Karwatzki and A. Mertens, "Generalized control approach for a class of modular multilevel converter topologies," *IEEE Transactions on Power Electronics*, vol. 33, no. 4, pp. 2888–2900, Apr. 2018, ISSN: 0885-8993. DOI: 10.1109/TPEL.2017.2703917.

[62] R. H. Cuzmar, A. Mora, J. Pereda, R. P. Aguilera, P. Poblete, and S. Neira, "Computationally efficient mpc for modular multilevel matrix converters operating with fixed switching frequency," *IEEE Open Journal of the Industrial Electronics Society*, vol. 4, pp. 748–761, 2023. DOI: 10.1109/OJIES.2023.3347101.

[63] D. P. Bertsekas, "Nonlinear programming: 3rd edition," in Athena Scientific, 2016.